1-1-2007

Morphological control in nanostructured polymers.

Shujun Chen
University of Massachusetts Amherst

MORPHOLOGICAL CONTROL IN NANOSTRUCTURED POLYMERS

A Dissertation Presented

by

SHUJUN CHEN

Submitted to the Graduate School of the
University of Massachusetts Amherst in partial fulfillment
of the requirements for the degree of

DOCTOR OF PHILOSOPHY

February 2007

Polymer Science and Engineering

INFORMATION TO USERS

The quality of this reproduction is dependent upon the quality of the copy submitted. Broken or indistinct print, colored or poor quality illustrations and photographs, print bleed-through, substandard margins, and improper alignment can adversely affect reproduction.

In the unlikely event that the author did not send a complete manuscript and there are missing pages, these will be noted. Also, if unauthorized copyright material had to be removed, a note will indicate the deletion.

ProQuest Information and Learning Company
300 North Zeeb Road
P.O. Box 1346
Ann Arbor, MI 48106-1346

MORPHOLOGICAL CONTROL IN NANOSTRUCTURED POLYMERS

A Dissertation Presented

by

SHUJUN CHEN

Approved as to style and content by:

Samuel P. Gido, Chair

Thomas P. Russell, Member

H. Henning Winter, Member

Shaw Ling Hsu, Department Head
Polymer Science & Engineering

MORPHOLOGICAL CONTROL IN NANOSTRUCTURED POLYMERS

A Dissertation Presented

by

SHUJUN CHEN

Approved as to style and content by:

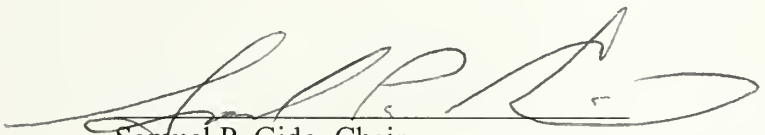

Samuel P. Gido, Chair

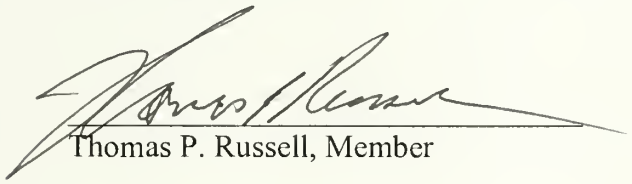

Thomas P. Russell, Member

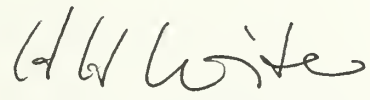

H. Henning Winter, Member

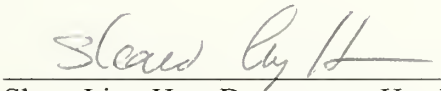

Shaw Ling Hsu, Department Head
Polymer Science & Engineering

DEDICATION

To my loving parents, Bingtao Chen and Wangrong Jiang.

ACKNOWLEDGMENTS

I would like to thank God, for being so faithful and being the source of love, strength and wisdom in my life. Without God, I couldn't have been able to go through this journey and finish this dissertation.

I want to thank my thesis advisor, Professor Sam Gido, who has been so supportive of me throughout my Ph.D. career. He is the type of advisor who gives you a lot of freedom in choosing and experimenting with whatever research ideas that may interest you; yet when you face a roadblock and need his directions, he is always there for you, lending his advice and helping you out. I especially appreciate his wisdom and kindness in persuading me not to quit my Ph.D. program but rather leave my options open when I felt so frustrated in my research and just wanted to give up. Looking back, I was really fortunate to have him as an advisor and to take his advice in applying for a leave of absence instead. Who (besides Professor Gido) could have imagined at the time that I would return to the Polymer Science and Engineering (PSE) program two years later and eventually finish my Ph.D.?

I am also greatly indebted to my thesis committee members, Professors Tom Russell and Henning Winter. Although both of them are very busy with their numerous responsibilities, they always made time for me when I needed help, even if it sometimes meant walking along and riding elevators together. They listened to my concerns and gave me lots of good advice, about my research as well as about my future career. I am especially thankful for their timely response and strong support in my postdoc job search.

I would like to thank my research collaborators for providing the polymers and for their contributions to my Ph.D. thesis work during the past three years: Professor Jimmy Mays at the University of Tennessee; Professor Nikos Hadjikristidis at the University of Athens; Professors Rudolf Faust and Daniel Sandman. Dr. Yonghua Zhou and Mr. Xiaoyu Wang at the University of Massachusetts Lowell; and Professor Henning Winter and Dr. Souvik Nandi at the University of Massachusetts Amherst.

I wish to thank my funding agencies, the National Science Foundation (NSF), the NSF-supported Materials Research Science and Engineering Center (MRSEC) at the University of Massachusetts Amherst, and the Army Research Laboratory (ARL), for their generous funding support for my Ph.D.

I would like to express my appreciation to the PSE department, for the excellent faculty, the wonderful staff, and the world-class facilities. Specifically, I would like to thank Professors Farris, McCarthy and Crosby, for being my mentors and strong supporters. My special thanks also go to Eileen, Sophie, Ann, Anita, Vivien, Anne, Linda, Cathy, Greg, Andre, Lou, Evgenia, and Sekar, for their friendly smiles and timely help with my paperwork, building, computer, or instrument problems. I owe a large debt of gratitude to Greg, who is like a father to me, and to so many international students. He cares deeply about the PSE students and is always there for us, during times of happiness as well as times of frustration.

I want to thank all past and present Gido group members: Darrin, Regina, Chin, Jeanene, Jennifer, Rick, Shi-Juang, Ken, Lizhang, Sheng, Robin, Yuqing, Xiaochuan, Engin, Sungkyun, Ashoutosh, Bode, Tomo, Thieu, Roland Weidisch, Tamako, Xiaodong,

and Roland Horst. I have enjoyed the group outings, the late working nights, as well as the stimulating discussions we had about research, life and Sam.

My thanks also go to all my friends at UMass. To Yoko, who is my classmate and has been through so much with me over the years. I cherish her friendship greatly and am really happy that we will both graduate this year! To Wen, who is like a sister and always cares for me throughout the years. To Ru, Chuntao, Xinqiao, Huiqing, Maohua, Tao, Lei, Zhiqun, Ting, and Yao, for their help and support during my early years at PSE. To Zhixiang, Qingling, Zhaoyang, Jianing, Xiaoming, Jiafang, Liming, Xianbo, Guolin, Lichao, and Yufeng, for the fun badminton games and their friendship. To Jong-Young, Chi-Lun, Kyusoon, and Kaoru, for the lunches at Hatch and for their support. To Jiayu, Ling, and Yunxia, for their hospitality and friendship. Also to Joanna, Jess, and Naomi, for the good times we had in the PSE ASPIRE and Outreach programs.

I owe special thanks to my church friends in Boston: Maggie, Winnie, Terry, Melody, and Julia, who above all brought me to God and have always kept me in their prayers. Also to my church in Amherst, which is like a big family and always keeps me grounded. Particularly, to Zifeng, Baoshan, Bing, Wenying, Xinmei, Yajing, and Yan, for their fellowship, love, support, and prayer during the ups and downs of my Ph.D. career.

Finally, I would like to express my deepest appreciation to my family: My father Bingtao Chen, my mother Wangrong Jiang, my brothers Yunhe and Rengang Chen, my sisters-in-law Lingli Hu and Li Cai, and my niece Kexin Chen. Without their unconditional, unwavering love, support, and sacrifice, I couldn't have come this far and finished my Ph.D. study. To them, I am forever indebted.

ABSTRACT

MORPHOLOGICAL CONTROL IN NANOSTRUCTURED POLYMERS

FEBRUARY 2007

SHUJUN CHEN, B.S., WUHAN UNIVERSITY

M.S., BENTLEY COLLEGE

Ph.D., UNIVERSITY OF MASSACHUSETTS AMHERST

Directed by: Professor Samuel P. Gido

This dissertation investigates several aspects of an important research topic in polymer science, that is, morphological control in polymer nanostructures. A brief introduction is given in Chapter 1. In Chapter 2, the central issue is defect control in novel noncentrosymmetric (NCS) lamellar block copolymer blends, made from poly(styrene-*b*-butadiene-*b*-isoprene-*b*-cyclohexadiene) and poly(styrene-*b*-cyclohexadiene). Coexisting centrosymmetric (CS) and NCS lamellar morphologies were observed, as predicted by mean-field theory. Morphologies of NCS tilt and twist grain boundary defects are studied, and detailed analysis of interfacial energies associated with NCS twist grain boundaries are performed. Defects unique to NCS layered systems, such as versatile NCS kink bands and NCS polarity reversals, are also studied in detail. Based on these results, strategies for reducing certain NCS defects are proposed.

In Chapter 3, the issue becomes morphological characterization of a new ABA triblock copolymer, poly(*tert*-butyl vinyl ether-*b*-isobutylene-*b*-*tert*-butyl vinyl ether) (P*t*BVE-PIB-P*t*BVE), a thermoplastic elastomer (TPE) and precursor for poly(vinyl

alcohol-*b*-isobutylene-*b*-vinyl alcohol) (PVA-PIB-PVA). P*t*BVE-PIB-P*t*BVE samples with 23–39 wt% P*t*BVE content exhibited typical characteristics of TPE with tensile strengths of 9–15 MPa and elongations at break of 760–1300%, and formed lamellar or cylindrical morphologies, depending on molecular compositions.

In Chapter 4, the subject shifts to crystal morphology characterization of a porous crystalline polymer (high density polyethylene, HDPE) prepared through a novel crosslinking-swelling-crystallization (CSX) process. Open pores with oriented lamellar structures in the pore walls were observed, much different from structures found in typical bulk HDPE. Based on the crystal morphology, possible mechanisms for the pore formation in the CSX process are proposed.

In Chapter 5, results from two other polymer systems studied are summarized. For the first system, poly(styrene-*b*-ethylene butylene-*b*-styrene), the effects of solvent selectivity and annealing temperature on resulting morphologies are studied systematically. Spherical or lamellar morphologies were initially obtained from three selective solvents; upon thermal annealing all changed into cylindrical morphology. The second system is polydiacetylene (PDA) single crystals of bulk, micron, and submicron sizes. For both PDAs studied, the crystal lattice parameters do not change markedly with decreasing crystal size, suggesting other factors may contribute to the observed change in optical properties.

TABLE OF CONTENTS

LIST OF TABLES

LIST OF FIGURES

CHAPTER 1

INTRODUCTION

1.1 Noncentrosymmetric Lamellar Block Copolymer Systems

Noncentrosymmetric (NCS) materials, that is, materials that lack a center of symmetry, are rare in nature. Due to their inherent polarization, periodic NCS materials display a variety of interesting properties, such as piezo- or pyroelectricity and second-order nonlinear optical activity.[1] In amorphous materials, noncentrosymmetry can be obtained by depositing particular sequences of layers on top of each other, or by applying external fields to orient the molecules,[2] in order to achieve a macroscopic polarization. An alternative approach is to take advantage of the self-assembling property of block copolymers. Abetz and coworkers[3] first demonstrated the success of such an approach. By blending lamellar ABC triblock terpolymers and lamellar ac diblock copolymers, in which all blocks have similar lengths, they were able to obtain a periodic NCS lamellar structure with the sequence ...ABC ca ABC... Later they also found the formation of NCS lamellar structures in blends of two lamellar ABC triblock copolymers differing only in the length of their middle block, as well as in a blend of lamellar ABC and lamellar BAC triblock copolymers.[4] Recently Takano et al.[5] reported an NCS structure from a tetrablock quarterpolymer of the ABCA type.

There has also been some theoretical work performed on NCS lamellar systems.[6-8] Leibler and coworkers[6] studied the NCS blend of lamellar ABC triblocks and lamellar ac diblocks and gave a theoretical explanation for the existence of such a structure, using

molecular parameters such as monomer-monomer incompatibilities and block molecular weights. By assuming an asymmetric interpenetration profile for the mixed Aa and Cc interfaces, they found that the free energy for the mixed Aa (Cc) interface is lower than the mean value of AA (CC) and aa (cc) interface free energies, and therefore an NCS structure with mixed Aa and Cc interfaces is favored. Wickham and Shi[7] examined the phase behavior of the same lamellar ABC/ac blend system using self-consistent mean-field theory. In the theoretical phase diagram thus obtained, several equilibrium lamellar structures are observed, depending on the volume fraction of the diblocks, ϕ_2, the monomer interactions, and the degrees of polymerization of the copolymers. In particular, the pure NCS phase is found to be stable over a narrow region near $\phi_2 = 0.4$. Shi and coworkers[8] also studied the phase behavior of ABCD tetrablock quarterpolymer melts using self-consistent mean-field theory. Large regions of enthalpically stabilized NCS lamellar phase (...ABCD ABCD...) are found when an attractive interaction is assumed between the A and D blocks. Entropically stabilized NCS phases (...ABCA ABCA...) are also found for ABCA tetrablock melts where the two end A blocks are equal in size.

1.2 Defects in Lamellar Block Copolymers

The study of defects, or disruptions of order, is an important aspect of study for any ordered materials, from metals, liquid crystals, to self-assembled block copolymers. It is essential to understand the types of defects in an ordered system, the energetics of these defects, as well as the physics behind them, so that they can be better controlled in the material of interest for intended applications. In many cases, the number of defects

needs to be minimized in order to achieve better long-range order, such as in high-fidelity electronic devices. In other cases, the proliferation of certain defects is desired, for example, grain boundaries in lamellar block copolymers used as gas permeation membranes.

In the area of self-organizing block copolymers, there has been some experimental[9-11] as well as theoretical[12-14] work on the defects in lamellar diblock copolymers, or centrosymmetric (CS) lamellar systems. On the other hand, there has been no research done on the nature and characterization of defects present in NCS lamellar block copolymer systems. It is therefore worthwhile to explore the types of defects that are inherent in this novel NCS structure. Such an understanding will be fundamental to the ultimate goal of defect control in NCS materials, the success of which depends in large part on the ability to get defect-free structures on a macroscopic scale.

1.3 Morphological Control Using Selective Solvents

It is well-known that the morphologies of block copolymers are dependent on the solvents from which they are cast.[15] The selectivity of the solvent affects the effective volume fractions of different blocks, and therefore the resultant morphology. For example, the morphology of a lamellar AB diblock copolymer may become that of A cylinders when cast from a B-selective solvent, and that of A spheres if the solvent selectivity for B is even higher.

Usually equilibrium morphologies are desirable and neutral or non-preferential solvents are used. In practice, however, it is often hard to find a true neutral solvent for a two-phase system, let alone a system with three or more components. Even if such a neutral solvent does exist, its use may not be preferred due to environmental or economical concerns. Therefore, the use of a selective solvent may be inevitable in certain applications.

In many cases, the initial non-equilibrium morphology obtained from a selective solvent may be converted to the equilibrium morphology via thermal annealing. One can imagine that, depending on the degree of selectivity of the initial casting solvent, and in turn the nature of the initial morphology, the degree of order as well as lattice dimensions in the final morphology may vary. Such a selective-solvent effect may be a positive or negative one, that is, the resultant final morphology may have better or worse order as compared to the one from a neutral (or almost neutral) solvent. If it turns out to be a positive one, it will become a new means to improve long-range order in block copolymer morphologies.

It is therefore meaningful to study systematically the effect of solvent selectivity on the final block copolymer morphology, in terms of both the degree of order and the lattice dimensions, and assess the feasibility of using selective solvents as a possible means of morphological control in block copolymer systems.

1.4 Morphological Control through Chemical Degradation

Another means to achieve morphological control, or more precisely, morphological change, is through the use of chemical degradation. Of particular interest is the ability to induce morphology change (change in domain size, or entire morphology) in a block copolymer when one of the blocks is partially removed through chemical degradation. Two of the main methods of chemical degradation used so far are UV-ozone treatment and hydrolysis. Thin films containing regularly packed nanochannels have been prepared through both means. The former has proved quite successful on the removal of poly(methyl methacrylate) (PMMA),[16] and the latter has mainly been used in the conversion of poly(*tert*-butyl methacrylate) (P*t*BMA) and poly(*tert*-butyl acrylate) (P*t*BA) to poly(methacrylic acid) (PMAA)[17] and poly(acrylic acid) (PAA),[18] respectively.

In terms of hydrolysis, all of the systems studied so far have been anionically polymerized block copolymers containing a methacrylate or acrylate block. Recent advances in living cationic polymerization have made available well-defined block copolymers containing poly(*tert*-butyl vinyl ether) blocks, which are readily converted to poly(vinyl alcohol) blocks through hydrolysis. It would be interesting to study these *tert*-butyl vinyl ether-containing block polymers and investigate the types of hydrolysis-induced morphological change in these polymers.

1.5 References

(1) Landau, L. D.; Lifshitz, E. M. *Electrodynamics of Continuous Media*; Pergamon: Oxford, 1987.

(2) Yariv, A. *Quantum Electronics*; Saunders College Publishing: Philadelphia, 1991.

(3) Goldacker, T.; Abetz, V.; Stadler, R.; Erukhimorich, I.; Leibler, L. *Nature* **1999**, *398*, 137–139.

(4) Abetz, V.; Goldacker, T. *Marcomol. Rapid Commun.* **2000**, *21*, 16–34.

(5) Takano, A; Soga, K.; Suzuki, J; Matsushita, Y. *Macromolecules* **2003**, *36*, 9288–9291.

(6) Leibler, L.; Gay, C.; Erukhimovich, I. *Europhys. Lett.* **1999**, *46*, 549–554.

(7) Wickham, R. A.; Shi, A.-C. *Macromolecules* **2001**, *34*, 6487–6494.

(8) Jaffer, K. M.; Wickham, R. A.; Shi, A.-C. *Macromolecules* **2004**, *37*, 7042–7050.

(9) Gido, S. P.; Thomas, E. L. *Macromolecules* **1994**, *27*, 6137–6144.

(10) Gido, S. P.; Gunther, J.; Thomas, E. L.; Hoffman, D. *Macromolecules* **1993**, *26*, 4506–4520.

(11) Gido, S. P.; Thomas, E. L. *Macromolecules* **1994**, *27*, 849–861.

(12) Tsori, Y.; Andelman, D; Schick, M. *Phys. Rev. E* **2000**, *61*, 2848–2858.

(13) Duque, D.; Schick, M. *J. Chem. Phys.* **2000**, *113*, 5525–5530.

(14) Matsen, M. W. *J. Chem. Phys.*, **1997**, *107*, 8110–8119.

(15) Lodge, T. P.; Pudil, B.; Hanley, K. J. *Macromolecules* **2002**, *35*, 4707–4717.

(16) Thurn-Albrecht, T.; Schotter, J.; Kastle, G. A.; Emley, N.; Shibauchi, T.; Krusin-Elbaum, L.; Guarini, K.; Black, C. T.; Tuominen, M. T.; Russell, T. P. *Science* **2000**, *290*, 2126–2129.

(17) Abetz, V.; Markgraf, K.; Rebizant, V. *Macromol. Symp.* **2002**, *177*, 139–145.

(18) Lu, Z.; Liu, G. J.; Duncan, S. *Macromolecules* **2004**, *37*, 174–180.

CHAPTER 2

DEFECTS IN NONCENTROSYMMETRIC LAMELLAR BLOCK COPOLYMER BLENDS

2.1 Abstract

This chapter summarizes experimental results from a defect study on the noncentrosymmetric (NCS) lamellar blend of an ABCD tetrablock quarterpolymer and an AD diblock copolymer. The block copolymers used were polystyrene-*block*-polybutadiene-*block*-polyisoprene-*block*-polycyclohexadiene (SBIC) and polystyrene-*block*-polycyclohexadiene (sc). Coexisting tetrablock-rich mixed centrosymmetric (CS) and NCS lamellar morphologies were seen in transmission electron microscopy (TEM) and confirmed by small angle x-ray scattering (SAXS), as predicted by the mean-field theory. The morphologies of new NCS twist grain boundary defects were studied, and detailed analysis of interfacial energies associated with these NCS tilt and twist grain boundaries were performed. Defects unique to NCS layered systems, such as versatile NCS kink bands and NCS polarity reversals, were also studied in detail. Based on these results, strategies for reducing certain NCS defects are proposed.

2.2 Introduction

Noncentrosymmetric (NCS) materials, that is, materials which lack a center of symmetry, are rare in nature. Due to their inherent polarization, periodic NCS materials display a variety of interesting properties, such as piezo- or pyroelectricity and second-order nonlinear optical activity.[1] In amorphous materials, noncentrosymmetry can be

obtained by depositing particular sequences of layers on top of each other, or by applying external fields to orient the molecules,[2] in order to achieve a macroscopic polarization. An alternative approach is to take advantage of the self-assembling property of block copolymers. Abetz and coworkers[3] first demonstrated the success of such an approach. By blending lamellar ABC triblock terpolymers and lamellar ac diblock copolymers, in which all blocks have similar lengths, they were able to obtain a periodic NCS lamellar structure with the sequence ...ABC ca ABC.... as shown in Figure 2.1. Later they also found the formation of NCS lamellar structures in blends of two lamellar ABC triblock copolymers differing only in the length of their middle block, as well as in a blend of lamellar ABC and lamellar BAC triblock copolymers.[4] Recently Takano et al.[5] reported an NCS structure from a tetrablock quarterpolymer of the ABCA type.

There has also been some theoretical work performed on NCS lamellar systems.[6-8] Leibler and coworkers[6] studied the NCS blend of lamellar ABC triblocks and lamellar ac diblocks and gave a theoretical explanation for the existence of such a structure, using molecular parameters such as monomer-monomer incompatibilities and block molecular weights. By assuming an asymmetric interpenetration profile for the mixed Aa and Cc interfaces, they found that the free energy for the mixed Aa (Cc) interface is lower than the mean value of AA (CC) and aa (cc) interface free energies, and therefore an NCS structure with mixed Aa and Cc interfaces is favored. Wickham and Shi[7] examined the phase behavior of the same ABC/ac lamellar blend system using self-consistent mean-field theory. In their theoretical phase diagram (Figure 2.2), several equilibrium coexisting lamellar phases are predicted, depending on the monomer interactions, the

degrees of polymerization, and the volume fractions of the copolymers in the blend. In particular, the pure NCS phase is found to be stable over a narrow region near a diblock volume fraction of 0.4. Shi and coworkers[8] also studied the phase behavior of ABCD tetrablock quarterpolymer melts using self-consistent mean-field theory. Large regions of enthalpically stabilized NCS lamellar phase (...ABCD ABCD...) are found when an attractive interaction is assumed between the A and D blocks. Entropically stabilized NCS phases (...ABCA ABCA...) are also found for ABCA tetrablock melts where the two end A blocks are equal in size.

The study of defects, or disruptions of order, is an important aspect of study for any ordered materials, from metals, liquid crystals, to self-assembled block copolymers. It is essential to understand the types of defects in an ordered system, the energetics of these defects, as well as the physics behind them, so that they can be better controlled in the material of interest for intended applications. In many cases, the number of defects needs to be minimized in order to achieve better long-range order, such as in high-fidelity electronic devices. In other cases, the proliferation of certain defects is desired, for example, grain boundaries in lamellar block copolymers used as gas permeation membranes.

In the area of self-organizing block copolymers, there has been some experimental[9-11] as well as theoretical[12-14] work on the defects in lamellar diblock copolymers, or centrosymmetric (CS) lamellar systems. On the other hand, there has been no research done on the nature and characterization of defects present in NCS

lamellar block copolymer systems. It is therefore worthwhile to explore the types of defects that are inherent in this novel NCS structure. Such an understanding will be fundamental to the ultimate goal of defect control in NCS materials, the success of which depends in large part on the ability to get defect-free structures on a macroscopic scale.

In this chapter of the thesis, a defect study on NCS lamellar blend systems is conducted. The NCS lamellar morphology is studied using TEM and SAXS. The types of defects are explored and characterized. Of these, the structures of three new NCS defects are studied in detail and explanations for structure formation are proposed.

2.3 Experimental Section

2.3.1 Synthesis

Block copolymers were synthesized by sequential anionic polymerization of different monomers. A polystyrene-*block*-polybutadiene-*block*-polyisoprene-*block*-polycyclohexadiene tetrablock quarterpolymer (SBIC) and a polystyrene-*block*-polycyclohexadiene diblock copolymer (sc) were synthesized in benzene using *sec*-butyllithium as the initiator and 1,4-diazabicyclo[2.2.2]octane (DABCO) as the polar additive. Details are given in refs 15 and 16. The characteristics of the block copolymers are given in Table 2.1.

2.3.2 Sample Preparation

SBIC tetrablock and sc diblock copolymers were dissolved together in toluene at a 50/50 molar blend ratio (equimolar blend). The toluene solution was evaporated over

several weeks to get a solid sample film, which was then placed in a vacuum oven for 1 week at room temperature to remove any residual solvent. To further promote the approach to an equilibrium structure, the oven temperature was slowly increased to an annealing temperature of 150°C and held there for another week before lowering to room temperature. For comparison, sample films of pure SBIC tetrablock quarterpolymer were prepared under same conditions.

2.3.3 Transmission Electron Microscopy (TEM)

Ultrathin sections (~50 nm in thickness) of the samples were obtained using a Leica ultramicrotome equipped with a Diatome diamond knife at a knife/sample temperature of -110°C. The sections were then stained in OsO_4 vapors for 30 min. TEM was performed on a JEOL 2000FX transmission electron microscope operating at 200 kV.

2.3.4 Small Angle X-ray Scattering (SAXS)

This was performed on annealed films using a Molecular Metrology 2D SAXS instrument powered by a high brilliance Osmic Max-Flux source with Cu Kα X-ray radiation and pinhole collimation. Patterns were collected digitally with a 2D multiwire detector and analyzed with a FAST ComTec MPA-3 multichannel analyzer and custom-written software. Extraneous background scatter was subtracted, and the data was plotted on a logarithmic scale. Circular averaging was performed to produce a plot of intensity vs. scattering angle, q.

2.4 Results and Discussion

2.4.1 Noncentrosymmetric (NCS) Lamellar Morphology

A representative TEM micrograph of the blend morphology is shown in Figure 2.3a. PB and PI phases are more readily stained by OsO_4 and appear dark in the TEM image, while the PCHD phase is slightly stained by OsO_4 and appears gray, and the PS phase does not react with OsO_4 and appears light. For the SBIC tetrablock, it is not possible to distinguish the middle phases PB and PI due to their similar reactivity with OsO_4. In the upper half of Figure 2.3a, repeating stacks of white-black-gray layers are clearly seen, indicating the NCS lamellae of PS, PB/PI, and PCHD. This morphology is drastically different from the centrosymmetric (CS) lamellar morphology formed by pure SBIC tetrablock, as shown in Figure 2.3b.

The bottom half of Figure 2.3a shows coexisting morphologies of centrosymmetric SBIC tetrablock lamellae and sc diblock lamellae in the blend. As mentioned in the introduction, Wickham and Shi's theory[7] predicts that in an ABC/ac lamellar blend pure NCS morphology is stable only in a narrow region near $\phi_2 = 0.4$ in the χN-ϕ_2 phase diagram, where χ is the Flory-Huggins interaction parameter between the different blocks (assuming $\chi_{AB} = \chi_{BC} = \chi_{AC} \equiv \chi$), N is the total degree of polymerization of the diblock, and ϕ_2 is the volume fraction of the diblock in the blend. In the SBIC/sc blend, of the three Flory-Huggins interaction parameters, χ_{SB}, χ_{IC}, and χ_{SC}, only the first is available. According to the relationship[17] $\chi = -0.00096 + 18.78/T$, χ_{SB} was calculated to be 0.0494 at the glass-transition temperature of polystyrene (373 K). Using this χ value and the molecular characteristics listed in Table 2.1 for the

SBIC/sc equimolar blend. χN and ϕ_2 values were calculated to be 15.75 and 0.31, respectively. At $\phi_2 = 0.31$, coexisting triblock-rich mixed CS and NCS morphologies are predicted between χN values of 14 and 28 in the theoretical phase diagram calculated by Wickham and Shi.[7] Our experimental observations of coexisting tetrablock-rich CS and NCS morphologies are consistent with their theory predictions.

The small angle x-ray scattering profiles of the SBIC/sc blend, the SBIC tetrablock, and the sc diblock are shown in Figure 2.4. All three profiles have a series of q_n/q^* ratios of 1: 2: 3.... indicative of lamellar morphologies. The lamellar long periods of SBIC/sc blend, SBIC tetrablock, and sc diblock are 37.1 nm, 51.6 nm, and 23.3 nm respectively. This further confirms the NCS morphology in the blend, because the lamellar long period of the blend, 37.1 nm, is approximately half of the sum of the long periods of the centrosymmetric SBIC tetrablock and sc diblock, or 37.4 nm. The shoulder between the first- and second-order NCS peaks in the SBIC/sc blend profile matches the second-order peak in the SBIC tetrablock profile, reconfirming the coexistence of NCS and tetrablock-rich CS morphologies in the blend. However, the much higher scattering intensity from the first-order peak of the NCS series indicates that the NCS morphology is the predominating morphology in the blend.

One important feature of the NCS morphology is the presence of a particular defect in the boxed region of Figure 2.3a. This defect, which we call a polarity reversal, is formed at the grain boundary of two oppositely oriented NCS stacks of lamellae, and is not possible in CS diblock and tetrablock lamellar systems. A similar defect was briefly

discussed by Goldacker et al.,[3] although no detailed analysis was provided. In this paper, a detailed discussion of the polarity reversal defect will be provided later in a separate section.

In addition to the polarity reversal defect, typical grain boundary defects similar to those present in CS diblock lamellar systems, are also observed for the NCS lamellar blend.[9] Shown in Figure 2.5 are representative TEM micrographs of two types of tilt grain boundaries in the SBIC/sc NCS lamellar system. Figure 2.5a shows a chevron tilt boundary in the NCS lamellae. This occurs when the tilt angle θ between the two sets of lamellar planes is relatively small. Different from that of diblock lamellae, the NCS chevron can be complicated by defects such as polarity reversals. Figure 2.5b shows an omega tilt boundary in the NCS lamellae. This results when the tilt angle θ between the adjoining lamellae is large. Unlike omegas in CS diblock lamellae where only one of the lamellar phases forms protrusion, omegas in the NCS lamellae require two of the phases to form protrusions at the same time.

Of all the new NCS grain boundary defects, NCS twist boundaries represent a new interesting category and therefore were studied in more detail. The characteristic morphologies and interfacial energies associated with these NCS twist boundaries are discussed in the next two sections, followed by a section on one interesting type of NCS tilt boundaries, NCS kink bands.

2.4.2 NCS Twist Boundary Morphologies

In centrosymmetric lamellar diblock systems, high-angle twist boundaries have inter-material dividing surfaces (IMDS) that approximate minimal surfaces mathematically known as Scherk's first surface.[10,18] The nature of the Scherk twist boundary in diblock lamellar systems was studied in detail by Gido and coworkers both experimentally[10] and theoretically[11] using a series of PS-*b*-PB lamellar diblock copolymers.

2.4.2.1 Brief Review of the Scherk Twist Boundary

A model of the Scherk twist boundary as well as computer ray tracing simulation of a TEM tilt series of this boundary is shown in Figure 2.6, as adapted from ref 10. The portion of the surface where the two lamellar phases cross consists of a doubly periodic array of saddle regions. Projecting this Scherk boundary down the z-axis gives rise to a crossing pattern shown in Simulation A. In this TEM simulation, the black and white regions are from matching phases in the AB diblock, while the gray regions are from the saddle regions, in which roughly half of the material that electrons pass through is A and half is B. As the Scherk boundary is tilted along the y-axis, the crossing pattern in Simulation A is gradually disappearing, and eventually the pattern shown in Simulation G is seen, which corresponds to projecting directly down the x-axis, so that one set of the lamellae is viewed from the side (left set) and the other from the top (right set).

2.4.2.2 NCS Twist Boundary Crossing Patterns

Due to the coexistence of NCS and CS morphologies in most NCS lamellar blends,[7] three types of twist grain boundary are possible in an NCS lamellar blend. The corresponding crossing patterns (projections down the z-axis) for these twist grain boundaries are illustrated in Figures 2.7a-c. To facilitate direct comparison with experimental TEM data, in these simulated crossing patterns the thicknesses of white, black, and gray layers are drawn in proportion to the respective experimental layer thickness values (Table 2.2), as determined from SAXS lamellar long period data and sample volume fraction data, for both the NCS SBIC/sc blend and the CS SBIC tetrablock. Because of the unequal volume fractions and the differences in block molecular weights in the two blend components, most features in these patterns are rectangles rather than squares. Nonetheless, the basic characteristics of the three crossing patterns, in terms of the components of the unit cells, are shared by all ABC/ac lamellar blend systems, as are listed in Table 2.3.

To facilitate contrast assignment in these crossing patterns, a grayscale is assigned to each of the three phases in the SBIC/sc blend based on TEM contrast. Two possible grayscale assignments are listed in Table 2.4. The most intuitive grayscale assignment, Case 1, gives the white, gray and black phases grayscales of 0%, 50% and 100%, respectively. However, in TEM images of the SBIC/sc blend such as Figure 2.3a, it is observed that the difference in contrast between the white and gray phases is much less than that between gray and black, due to the dominating staining of the PB/PI phases in the blend. This suggests Case 2, in which the white, gray and black phases are assigned

grayscales of 10%, 40% and 100%, respectively, is a more realistic grayscale assignment. Contrast levels for regions of mismatching phases can be estimated from average grayscales of the crossing phases in these regions, as also listed in Table 2.4. The grayscale assignment in Case 2 has been adopted in the illustration of the simulated crossing patterns (Figures 2.7a-c).

Figure 2.7a shows the pattern formed by NCS lamellae crossing with NCS lamellae. The basic unit cell in this pattern, as highlighted by the white box, is composed of 9 rectangles (3 x 3). Three of them are from matching phases: 1 white-white, 1 black-black and 1 gray-gray; and the rest are from mismatching phases: 2 white-blacks, 2 black-grays, and 2 white-grays. Figure 2.7b shows the pattern formed by NCS lamellae crossing with CS lamellae. Because the NCS and CS lamellar repeats consist of three and four layers respectively, the basic unit cell of this pattern is composed of 12 rectangles (3 x 4), of which four are from matching phases: 1 white-white, 2 black-blacks, and 1 gray-gray; and the other eight are from mismatching phases: 3 white-blacks, 3 black-grays, and 2 white-grays. The pattern formed by crossing two sets of CS lamellae is shown in Figure 2.7c. The basic unit cell of this pattern is composed of 16 rectangles (4 x 4), with six from matching phases: 1 white-white, 4 black-blacks, and 1 gray-gray; and the other ten from mismatching phases: 4 white-blacks, 4 black-grays, and 2 white-grays.

Although all three patterns in Figure 2.7 are examples of 90° twist grain boundaries, non-orthogonal crossing patterns are also possible (and more likely to occur)

in NCS lamellar blends, as will be shown in the TEM images below. In the non-orthogonal crossing patterns, the individual units are parallelograms instead of rectangles, but the same analyses apply in terms of contrast and unit cell structure.

Figure 2.8 shows a TEM micrograph of an NCS-NCS twist grain boundary. In the central area of this micrograph, the twist angle is about 90°. A box is drawn in this area, in which all discernable rectangles match well with the rectangles in the basic unit cell (boxed area) of the simulated crossing pattern in Figure 2.7a, in terms of both location and overall contrast, although the subtle differences in the grayness of the lighter regions (white-white, gray-gray, and white-grays) are simply too small to be caught by naked eyes. The matching of the unit cell in the TEM micrograph with that in the simulated crossing pattern suggests that Figure 2.7a is a reasonable representation of the NCS-NCS twist boundary projection along the z-axis.

In Figure 2.8, there is tilt associated with one set of the NCS lamellae (the vertical one) forming the twist boundary, therefore the crossing pattern changes from an orthogonal one in the center to non-orthogonal ones in the upper and lower parts of the TEM micrograph. Both non-orthogonal crossing patterns have a twist angle of about 60°, due to similar amounts of tilt involved.

Figure 2.9 shows a TEM micrograph of an NCS-CS twist grain boundary, corresponding to the crossing pattern in Figure 2.7b. The NCS lamellae on the left cross

with the CS lamellae in the center and give rise to a non-orthogonal crossing pattern, with a twist angle of about 60°.

An example of a CS-CS twist grain boundary is given in Figure 2.10. In the upper middle region of this TEM micrograph, a near-orthogonal crossing pattern corresponding to that in Figure 2.7c is clearly seen.

2.4.2.3 NCS Twist Boundary Tilt Series

Figure 2.11 shows a TEM tilt series of an NCS-NCS twist grain boundary. The tilt axis and tilt direction are indicated by the straight and curved arrows to the left of the TEM micrographs. The twist boundary is highlighted by the black box, which covers approximately the same sample area in all figures. The tilt axis is nearly along the lamellar normal (y-axis) of the set of lamellae to the left of the axis (Set 1). At 0° tilt, Figure 2.11a corresponds to a projection close to the lamellar normal (x-axis) of the set of NCS lamellae to the right of the tilt axis (Set 2), similar to that in Simulation G of Figure 2.6. As the sample is tilted, contrast from Set 2 starts to appear, so do the phase-mismatch regions in the twist boundary. The gradual appearance of the lamellae and the phase-mismatch regions is quite evident in Figures 2.11b and 2.11c, at 20° and 30° of tilt, respectively. In Figure 2.11d, at 40° tilt, the projection is closer to, although not exactly along the z-axis, and contrasts from both sets of lamellae forming the crossing pattern are clearly visible.

At this point, without further computer simulation or microtomography, it is difficult to understand the exact nature of the IMDS in a three-component twist grain boundary, given the complexity involved in visualizing how three different layers may meet orthogonally while preserving chain connectivity and volume incompressibility. Whether there exists an analogy to Scherk's first surface in a three-component lamellar system is yet to be determined.

2.4.3 NCS Twist Boundary Interfacial Energy Considerations

The crossing of unlike layers requires the creation of extra interfaces between the mismatching phases and therefore results in interfacial energy penalties; whereas when like layers cross, only one phase is present in the crossing region and no interfaces are created. Different crossing patterns therefore indicate different amounts of interfacial area for the respective twist grain boundaries, which should then cause different amounts of interfacial energy penalties. To compare the interfacial energy penalties associated with the three types of twist grain boundaries present in an ABC/ac lamellar blend, detailed analysis of the interfacial area in each twist boundary must first be performed. Then the interfacial energy penalties can be determined with known or estimated interfacial energies between the three different phases. The knowledge of interfacial energy penalties associated with the three different types of NCS twist grain boundaries should then help us understand the relative stability of these twist grain boundaries.

To facilitate the analysis of interfacial energy penalties, three types of ratios are defined, which are:

Interfacial Area Ratio. Although the exact nature of the interface in an NCS twist grain boundary is not known, the interfacial area of each phase-mismatch region can be estimated as the projected interfacial area in the crossing pattern times a prefactor, provided that all interfaces are of similar shapes, as do Scherk twist boundaries in diblock lamellar systems. The interfacial area ratio, $R_{area}(n)$, is thus defined as the ratio of total projected interfacial area for the nth type interface in the unit cell of a crossing pattern, $A_I(n)$, to total unit cell area of that crossing pattern, or the sum of total projected single phase area, $\Sigma A_S(m)$, and total projected interfacial area, $\Sigma A_I(n)$, in the unit cell.

$$R_{area}(n) = A_I(n) / [\Sigma A_S(m) + \Sigma A_I(n)] \qquad (1)$$

where $\Sigma A_S(m) = A_S(A) + A_S(B) + A_S(C)$, and $\Sigma A_I(n) = A_I(AB) + A_I(BC) + A_I(AC)$.

Interfacial Energy Ratio. In an ABC/ac lamellar blend system, there are three interfacial energies: γ_{AB}, γ_{BC}, and γ_{AC}. For demonstration purposes, normalized interfacial energies will be used for all calculations. The interfacial energy ratio, or normalized interfacial energy, $R_{energy}(n)$, is defined as the interfacial energy of the nth type interface divided by the highest interfacial energy among the three.

$$R_{energy}(n) = \gamma(n) / \gamma_{max} \qquad (2)$$

where $\gamma(1) = \gamma_{AB}$, $\gamma(2) = \gamma_{BC}$, $\gamma(3) = \gamma_{AC}$.

Energy Penalty Ratio. The energy penalty ratio, $R_{penalty}$, is simply the sum of the product of the interfacial area ratio, $R_{area}(n)$, and the interfacial energy ratio, $R_{energy}(n)$. The energy penalty ratios thus measure the relative interfacial energy costs associated with these NCS twist grain boundaries.

$$R_{penalty} = \Sigma[R_{area}(n) \cdot R_{energy}(n)] \qquad (3)$$

In the following section, the energy penalty ratios associated with the three different NCS twist grain boundaries are determined for (1) an ideal ABC/ac NCS lamellar blend, and (2) the SBIC/sc NCS lamellar blend.

2.4.3.1 Ideal ABC/ac NCS Lamellar Blend

In an ideal ABC/ac NCS lamellar blend, if equal block lengths are assumed for all blocks ($N_A = N_B = N_C = N_a = N_c$), the layer thicknesses of A, B, and C layers should obey the following relationship for both the NCS lamellae and the CS triblock lamellae:

$$h_A = h_C = 2h_B \equiv 2h \qquad (4)$$

Using this relationship, the interfacial area ratios for all three twist boundary crossing patterns in an ideal ABC/ac NCS lamellar blend are calculated and listed in Table 2.5.

In terms of interfacial energy ratios, if equal interfacial energies between the three phases are assumed, that is, $\gamma_{AB} = \gamma_{BC} = \gamma_{AC}$, all three interfacial energy ratios will have the value of 1, as in Scenario 1 in Table 2.6. The energy penalty ratios for the three NCS twist boundaries are therefore 0.640, 0.667, and 0.667, for NCS-NCS, NCS-CS, and CS-CS twist boundaries, respectively, which indicates that NCS-NCS twist boundary has the lowest interfacial energy cost under this assumption.

More realistically, the three phases in the NCS lamellar blend would have different surface energies, resulting in unequal interfacial energies, and in turn unequal interfacial energy ratios. Three representative scenarios of unequal interfacial energy ratios are selected and the corresponding energy penalty ratios for the three NCS twist boundaries are calculated and also listed in Table 2.6 (Scenarios 2-4). It is clear from Table 2.6 that in two of the three scenarios (Scenarios 2 and 3), where the middle phase B has either the lowest or highest surface energy among the three phases, the NCS-NCS twist boundary has the lowest interfacial energy cost, while in the other scenario (Scenario 4), where the middle phase B has the medium surface energy, the CS-CS twist boundary costs the least amount of interfacial energy.

2.4.3.2 SBIC/sc NCS Lamellar Blend

In reality, however, the layer thicknesses may not obey the relationship of eq 4, due to the differences in block lengths, as in the case of the SBIC/sc NCS lamellar blend. Using the experimental layer thickness values listed in Table 2.2, the interfacial area ratios for the three types of NCS twist boundaries in the SBIC/sc blend are calculated and listed in Table 2.7.

Because the SBIC/sc NCS lamellar blend is a real blend system, real interfacial energy values should be used to calculate the interfacial energy ratios, and in turn the energy penalty ratios. However, recall that in the SBIC/sc blend system, only one of the three χ's is currently available, which is χ_{SB}. The other two χ's involving PCHD are not available. The situation is the same for interfacial energies. In addition, for PCHD, no

measured solubility parameter or surface tension has been reported either. The only available interfacial-energy-related PCHD data are two calculated solubility parameters, one for 1,4-PCHD,[19] and one for 1,2-PCHD.[20] On the other hand, for PS, PB, and PI, both calculated and measured solubility parameters are available.[21-23]

It is known that there exists a relationship between interfacial energy between two polymer phases γ_{12} and the corresponding Flory-Huggins interaction parameter χ_{12}.[24]

$$\gamma_{12} = a\,(\chi_{12})^{1/2}\,RT / v \qquad (5)$$

where a is Kuhn length, R is the gas constant, T is the absolute temperature, and v is the molar monomer volume.

According to Hildebrand,[25] the Flory-Huggins interaction parameter χ_{12} can be estimated from solubility parameter differences between the two polymer phases through the following equation,

$$\chi_{12} = (\delta_1 - \delta_2)^2\, v / RT \qquad (6)$$

where δ_1 and δ_2 are solubility parameters of phases 1 and 2.

Assuming equal monomer volume for all block phases, eq 5 and eq 6 can be combined to get the following relationship:

$$\gamma_{12} = a\,(RT/v)^{1/2}\,(\delta_1 - \delta_2) \sim (\delta_1 - \delta_2) \qquad (7)$$

Therefore, the solubility parameter difference $\Delta\delta_{12} = \delta_1 - \delta_2$ can be used as an estimate for interfacial energies. Because measured solubility parameter of PCHD is not

available. $\Delta\delta_{SC}$ is determined from calculated δ_{PS} and $\delta_{1,4\text{-}PCHD}$ values in ref 19. to be 1.1 $MPa^{1/2}$, given that the PCHD blocks in both SBIC tetrablock and SC diblock used for this study consist of mainly 1,4-units. It is likely that the middle PB and PI phases are partially mixed due to their similar chemical structures and solubility parameters[22] (16.7 $MPa^{1/2}$ for PI and 17.4 $MPa^{1/2}$ for PB). To simplify the analysis, the two middle phases are treated as one mixed PB/PI phase and the average solubility parameter $\delta_{P(B/I)}$ for the two phases, 17.1 $MPa^{1/2}$, is used. Based on this $\delta_{P(B/I)}$ and the measured δ_{PS}[22], 18.6 $MPa^{1/2}$, the $\Delta\delta$'s are calculated as 1.5 $MPa^{1/2}$ and 0.4 $MPa^{1/2}$ for $\Delta\delta_{S(B/I)}$ and $\Delta\delta_{(B/I)C}$, respectively. The solubility parameters for the three block phases and corresponding $\Delta\delta$'s are listed in Table 2.8. The interfacial energy ratios are calculated from these $\Delta\delta$ values and also listed in Table 2.8.

Under the assumption of equal interfacial energies (Scenario 1 in Table 2.9), the energy penalty ratios for the three NCS twist boundaries are 0.657, 0.655, and 0.624, for NCS-NCS, NCS-CS, and CS-CS twist boundaries, respectively, which indicates that in the SBIC/sc blend CS-CS twist boundary has the lowest interfacial energy cost. This result is quite different from that for the ideal ABC/ac NCS lamellar blend under the same interfacial energy assumption (Scenario 1 in Table 2.6), which favors the NCS-NCS twist boundary.

Multiplying the interfacial energy ratios in Table 2.8 with the respective interfacial area ratios for the crossing patterns, the interfacial energy penalties for the three types of NCS twist boundaries in SBIC/sc blend are calculated and the results are

listed in Table 2.9 as Scenario 2. In this scenario with real calculated interfacial energy ratios, CS/CS twist boundary again gives the lowest energy penalty ratio, 0.342, indicating that it is the most stable twist boundary in the SBIC/sc blend. This result in also quite different from that for ideal ABC/ac NCS lamellar blend in a similar interfacial energy scenario (Scenario 2 in Table 2.6), which favors the NCS-NCS twist boundary. The different conclusions for SBIC/sc blend and ideal ABC/ac NCS lamellar blend in similar interfacial energy scenarios suggest that both interfacial area and interfacial energy can affect the resulting interfacial energy penalties and need to be taken into account when estimating stabilities of NCS twist boundaries, as has been done in this section.

If the above argument about interfacial energy penalty is valid, then one should expect that the most frequently observed twist boundary in the SBIC/sc blend is CS-CS twist boundary. This was indeed observed in the TEM. In addition to the large number of CS-CS twist boundaries observed, another evidence of the stability of CS-CS twist boundary is the frequent observation of a transition from NCS to CS lamellae as the layers approach a twist grain boundary. An example of such a transition is shown in Figure 2.12.

2.4.4 NCS Kink Bands

One particular defect related to tilt grain boundaries is that of kink bands. Unlike regular tilt grain boundaries which are formed when two initially nonparallel lamellar grains grow into each other, kink bands are generally believed to form through a

mechanical buckling process.[9] During the solvent casting process, as the solvent evaporates and the solution becomes concentrated, the copolymer molecules start to order and form lamellar grains, which are oriented randomly throughout the sample. For those lamellae that are oriented perpendicular to the substrate, upon further solvent evaporation, they will experience local compressive forces along the lamellae, which will then cause the layers to buckle and form kink bands.

Typically a kink band is composed of three sets of lamellae, as illustrated in Figure 2.13. The middle part of the kink band is called the kink zone. The two sets of layers outside the kink zone have the same lamellar orientation. The layers inside the kink zone are oriented at an angle θ to the layers outside. If two lines are drawn along the borders of the kink zone, the angle θ can be decomposed into two angles, θ_1 and θ_2, which correspond to the angle between the lamellar parallel of the layers outside the kink zone and the border line, and that between the border line and the lamellar parallel of the layers inside the kink zone, respectively.

During the buckling process, some parts of the original lamellae may be dilated, that is, the chains may be stretched and brush heights increased; while other parts may be compressed. Depending on the location of the kink zone in the original lamellae, the lamellae in a kink zone can be either dilated or compressed, having larger or smaller lamellar thickness than the equilibrium lamellar long period. To quantify the degree of lamellar expansion or compression inside the kink zone, a new term called expansion ratio is introduced, which is defined as the ratio of the layer thickness (d_2) inside the kink

zone to that outside the kink zone (d_1), as also shown in Figure 2.13. The expansion ratio R can also be expressed in terms of θ_1 and θ_2.

$$R = d_2 / d_1 = \text{Sin } \theta_2 / \text{Sin } \theta_1 \qquad (8)$$

In centrosymmetric lamellar diblock systems, only one lamellar long period is available for a certain diblock copolymer in a kink band. The only way to accommodate the expansion or compression requirement of the lamellae inside the kink zone is for the chains to be stretched or compressed. In NCS lamellar blends, however, due to the coexistence of NCS and CS morphologies, both NCS layers and CS layers can be incorporated into kink bands. Because the two lamellar morphologies have inherently different lamellar long periods, the layer expansion or compression requirement in a kink zone can be satisfied simply by choosing between the CS and NCS morphologies. The CS morphology has a larger lamellar long period because of one extra layer in the lamellar repeat. Therefore one way to accommodate a dilatational kink zone in the NCS lamellar blend is to change the morphology from NCS to CS in the kink zone. Conversely changing from CS to NCS morphology should accommodate a compressive kink zone. TEM micrographs of two such cases are shown in Figure 2.14. In Figure 2.14a, stacks of NCS layers transform into CS layers within the kink zone and transform back to NCS layers across the kink zone (NCS→CS→NCS). This accommodates expansion of the lamellae within the kink zone. In Figure 2.14b, stacks of CS layers transform into NCS layers within the kink zone and transform back to CS layers across the kink zone (CS→NCS→CS). This accommodates compression of the layers within the kink zone. In reality this switching between the NCS and CS morphologies is

possible because there is still considerable amount of solvent remained in the system when the kink bands are formed so that the polymer chains have enough mobility to diffuse into and out of the kink zone.

The formation of a particular type of NCS kink band depends on the degree of expansion or contraction required during a certain kinking process. If the expansion or contraction is only minimal, kink bands of the NCS→NCS→NCS type are observed, as seen in Figure 2.14c. In other cases, if the expansion is not great enough for a pure NCS→CS→NCS kink band, kink bands with mixed CS and NCS layers in the kink zone are observed, as seen in Figure 2.14d, in order to accommodate a particular expansion ratio. Compared with traditional CS kink bands in lamellar diblock systems, these NCS kinks bands are more versatile, taking full advantage of the available CS and NCS lamellae.

2.4.5 Polarity Reversals

The polarity reversal defect is one of the most commonly observed defects in the NCS lamellar system. In NCS lamellar systems, there are two ways one set of NCS lamellae can reverse its polarity. (1) The polarity is reversed in the direction normal to NCS layers. This is typically caused by the insertion of certain number of diblock chains, which interrupts the assembling of the NCS lamellae and flips their polarity as a result. In other words, it is a "misassembling" product. Examples of this type of polarity reversal defect are seen in Figure 2.15a. (2) The polarity is reversed in the direction parallel to NCS layers. This is the most commonly observed polarity reversal type and

the most detrimental in terms of material properties. In addition to the one shown in Figure 2.3a, Figures 2.12 and 2.14b also have regions where this defect is present. It is caused by the joining of two NCS lamellar grains of opposite polarity during the self-assembling process. Understanding the structure of and energy associated with these polarity reversal defects will help us find possible ways to minimize their presence and obtain defect-free NCS materials suitable for nonlinear optical and electronic applications.

2.4.5.1 Polarity Reversals Normal to NCS Layers

A representative TEM micrograph of this type of polarity reversal defect in the SBIC/sc NCS lamellar blend is shown in Figure 2.15a. In this figure, the polarities of certain NCS layers are marked by short white arrows, the direction of which follow the white-black-gray orientation of the noncentrosymmetric sSBICc lamellae. Careful examination of these arrows reveals that the polarity of the NCS layers sometimes reverse with the insertion of the diblock chains, sometimes not. For example, in the boxed area in Figure 2.15a, the two sets of NCS lamellae on the left have the same polarities, while the two on the right have opposite polarities, in other words, a polarity reversal forms on the right.

In order to find out what dictates the formation of polarity reversals normal to NCS layers and facilitate the structural analysis of such defects, a cartoon is drawn in Figure 2.15b to reproduce the layered structure in the boxed region in Figure 2.15a. In this cartoon, the SBIC and sc polymer chains composing the layers are drawn as light-

dark-gray and light-gray segments, the NCS lamellae are drawn as white-dark-gray layers, the ends of the broken layers are approximated as semi-cylindrical caps, and the polarities of the NCS layers are highlighted by black arrows following the S-BI-C orientation. By counting the number of diblock chains inserted between the NCS layers, it is found that in the case of no polarity reversals (left), 5 diblock chains are inserted; while in the case of polarity reversals (right), 4 diblock chains are inserted. Applying such analysis to more TEM images with polarity reversals normal to NCS layers, the following relationships can be obtained:

$n = 2m + 1$ No polarity reversal

$n = 2m$ Polarity reversal

where n is the number of diblock chains inserted, m is any positive integer.

In other words, when an odd number of diblock chains are inserted in between the NCS layers, no polarity reversal forms; when an even number of diblock chains are inserted, the polarity is reversed. This result is not unexpected, as the NCS lamellar repeat unit consists of exactly one diblock chain, therefore adding an even number of diblock chains doesn't alter the orientation of the diblock chain forming the next NCS lamellar repeat, whereas adding an odd number of diblock chains reverses the diblock orientation and in turn the polarity of the next NCS lamellae. The insertion of the diblock chains and formation of polarity reversals normal to NCS layers appears to be random. A possible explanation is the random distribution of higher concentration of diblock chains during the NCS lamellar self-assembling process.

2.4.5.2 Polarity Reversals Parallel to NCS Layers

A typical TEM micrograph of the polarity reversal defect parallel to NCS layers in the SBIC/sc blend system is shown in Figure 2.16a. For comparison, a polarity reversal defect in the polystyrene-*block*-polybutadiene-*block*-poly(*tert*-butyl methacrylate)/polystyrene-*block*-poly(*tert*-butyl methacrylate) (SBT/st) NCS lamellar blend taken from ref 3 is shown in parallel in Figure 2.16b. An obvious similarity between the two NCS lamellar systems is that in both systems one and only one of the three NCS layers is broken when a polarity reversal defect is formed. This is not surprising because the reversal of the NCS lamellar polarity across the grain boundary disrupts layer continuity and results in layer breaking and interface creation. By breaking just one NCS layer and keeping the continuity of the other two, the lamellar polarity can be successfully reversed with minimal amount of layer disruption and extra interface creation. However, in each NCS lamellar system, there are three different layers that may be broken in a polarity reversal. What then determines which one of the three NCS layers is broken? Careful examination of Figures 2.16a and 2.16b reveals that in the SBIC/sc blend system, the white layers (PS phase) are broken, while in the SBT/st blend system, the black layers (PB phase) are broken.

This difference in the polarity reversal broken phase cannot be explained by chain connectivity, because in one case the broken phase is the end block (PS in SBIC/sc), while in the other case the broken phase is a middle block (PB in SBT/st). A plausible explanation is that the thinnest lamella gets broken, because the breaking of the thinnest lamella, or the one with the lowest volume fraction, should lead to the creation of the

least additional interfacial area at the grain boundary, thus the minimization of the total interfacial energy, given the similar interfacial energies for lamellar block copolymers.

To test this hypothesis, the volume fractions of the respective phases for both SBIC/sc and SBT/st equimolar blend systems are calculated and listed in Table 2.10. In both systems, the broken phase, PS in SBIC/sc, or PB in SBT/st, is indeed the phase with the smallest volume fraction in the blend. Breaking the phase with the smallest volume fraction, and thus the thinnest lamella, is therefore a preferred solution for the formation of the polarity reversal.

As mentioned above, polarity reversals, especially those parallel to NCS layers, are one of the most commonly observed type of defects in NCS lamellar systems and the most harmful to the usefulness of the NCS lamellar materials. Based on the analysis on the broken phase and the proposed volume fraction theory, two strategies are proposed to reduce the impact of the polarity reversal defect. (1) Use strong-segregating blocks for the ABC and ac components of the NCS lamellar blends. Stronger segregating blocks should result in higher interfacial energies between the phases, thereby raising the interfacial energy barrier for polarity reversals. (2) Use high molecular weight polymers when making NCS lamellar blends. Higher molecular weight polymers should form thicker NCS layers, therefore increasing the additional interfacial area and also the interfacial energy cost for polarity reversals. These strategies should help reduce the number of polarity reversals formed during the self-assembling process. Thermal annealing will further reduce the number of polarity reversals. However, these strategies

alone won't be enough to eliminate the polarity reversals and make defect-free materials. A more promising way of making defect-free NCS materials should involve a combination of self-assembly and directed assembly techniques, such as the use of electrical or magnetic fields.

2.5 Conclusions

Noncentrosymmetric lamellar morphology was obtained in equimolar blend of SBIC tetrablock and sc diblock copolymers. Coexisting tetrablock-rich mixed CS and NCS lamellar morphologies were seen in TEM and confirmed by SAXS, as predicted by the mean-field theory. The morphologies of new NCS twist grain boundary defects were studied, and detailed analysis of interfacial energies associated with these NCS twist grain boundaries were performed. Defects unique to NCS layered systems, such as versatile NCS kink bands and NCS polarity reversals, were also studied in detail. Based on these results, strategies for reducing certain NCS defects are proposed.

2.6 References

(1) Landau. L. D.: Lifshitz. E. M. *Electrodynamics of Continuous Media*: Pergamon: Oxford. 1987.

(2) Yariv. A. *Quantum Electronics*: Saunders College Publishing: Philadelphia. 1991.

(3) Goldacker. T.: Abetz. V.: Stadler. R.: Erukhimorich. I.: Leibler. L. *Nature* **1999**. *398*. 137–139.

(4) Abetz. V.: Goldacker. T. *Marcomol. Rapid Commun.* **2000**. *21*. 16–34.

(5) Takano. A: Soga. K.: Suzuki. J: Matsushita. Y. *Macromolecules* **2003**. *36*. 9288–9291.

(6) Leibler. L.: Gay. C.: Erukhimovich. I. *Europhys. Lett.* **1999**. *46*. 549–554.

(7) Wickham. R. A.: Shi. A.-C. *Macromolecules* **2001**. *34*. 6487–6494.

(8) Jaffer. K. M.: Wickham. R. A.: Shi. A.-C. *Macromolecules* **2004**. *37*. 7042–7050.

(9) Gido. S. P.: Thomas. E. L. *Macromolecules* **1994**. *27*. 6137–6144.

(10) Gido. S. P.: Gunther. J.: Thomas. E. L.: Hoffman. D. *Macromolecules* **1993**. *26*. 4506–4520.

(11) Gido. S. P.: Thomas. E. L. *Macromolecules* **1994**. *27*. 849–861.

(12) Tsori. Y.: Andelman. D: Schick. M. *Phys. Rev. E* **2000**. *61*. 2848–2858.

(13) Duque. D.: Schick. M. *J. Chem. Phys.* **2000**. *113*. 5525–5530.

(14) Matsen. M. W. *J. Chem. Phys.*. **1997**. *107*. 8110–8119.

(15) Tsoukatos. T.: Avgeropoulos. A.: Hadjichristidis. N.: Hong. K.: Mays. J. W. *Macromolecules* **2002**. *35*. 7928-7935.

(16) Hong. K.: Mays. J. W. *Macromolecules* **2001**. *34*. 3540–3547.

(17) Wolff. T.: Burger. C.: Ruland. W. *Macromolecules* **1993**. *26*. 1707–1711.

(18) Chen. S.: Gido. S. P.: Tsoukatos. T.: Avgeropoulos. A.: Hadjichristidis. N.: Hong. K.: Mays. J. W. *Polymer Preprints* **2005**. *46(2)*. 542.

(19) David. J. L.: Gido. S. P.: Hong. K.: Zhou. J.: Mays. J. W.: Tan. N. B. *Macromolecules* **1999**. *32*. 3216–3226.

(20) Imaizumi, K.; Ono, T.; Natori, I; Sakurai, S.; Takeda, K. *J. Polym. Sci. Pol. Phys.* **2001**, *39*, 13–22.

(21) Small, P. A. *J. Appl. Chem.* **1953**, *3*, 71–80.

(22) Grulke, E. A. In *Polymer Handbook*, 4th ed.; Brandrup, J., Immergut, E. H., Grulke, E. A., Eds.; Wiley-Interscience: New York, 1999; p VII702.

(23) Barton, A. F. M. *CRC Handbook of Solubility Parameters and Other Cohesion Parameters*; CRC Press: Boca Raton, 1991; p 588.

(24) Helfand, E.; Tagami, Y. *J. Chem. Phys.* **1972**, *56*, 3592.

(25) Hildebrand, J. H.; Scott, R. L. *The Solubility of Non-Electrolytes*; Reinhold: New York, 1949.

Table 2.1 Molecular Characteristics of SBIC Tetrablock and sc Diblock Copolymers

Polymer	M_n (kg mol^{-1})	M_w/M_n	ϕ_{PS} (%)	ϕ_{PB} (%)	ϕ_{PI} (%)	ϕ_{PCHD} (%)
SBIC	52.6	1.14	18	22	24	36
sc	25.6	1.07	48	-	-	52

ϕ_x: the volume fraction of x.
PS: polystyrene.
PB: polybutadiene.
PI: polyisoprene.
PCHD: polycyclohexadiene.

Table 2.2 Layer Thicknesses in SBIC/sc NCS Lamellar Blend and SBIC CS Tetrablock Lamellar System

Polymer System	Layer Thicknesses (nm)		
	White (PS)	Black (PB/PI)	Gray (PCHD)
SBIC/sc	10	12	15
SBIC	9	12	19

Table 2.3 Basic Unit Cell Components of the Crossing Patterns for Three Types of Twist Grain Boundaries in ABC/ac NCS Lamellar Blend

NCS x NCS				NCS x CS				CS x CS			
Phase Match	No. of Subunits	Phase Mismatch	No. of Subunits	Phase Match	No. of Subunits	Phase Mismatch	No. of Subunits	Phase Match	No. of Subunits	Phase Mismatch	No. of Subunits
A x A	1	A x B	2	A x A	1	A x B	3	A x A	1	A x B	4
B x B	1	B x C	2	B x B	2	B x C	3	B x B	4	B x C	4
C x C	1	A x C	2	C x C	1	A x C	2	C x C	1	A x C	2
Total Subunits		9		Total Subunits		12		Total Subunits		16	

Table 2.4 TEM Grayscales for Crossing Phases in SBIC/sc NCS Lamellar Blend and SBIC CS Tetrablock Lamellar System

Crossing Phase(s)	PS (W x W)	PCHD (G x G)	PB/PI (B x B)	PS x PCHD (W x G)	PS x PB/PI (W x B)	PCHD x PB/PI (B x G)
Case 1: Grayscale (%)	0	50	100	25	50	75
Case 2: Grayscale (%)	10	40	100	25	55	70

Table 2.5 Interfacial Area Ratios for Twist Grain Boundaries in Ideal ABC/ac NCS Lamellar Blend

NCS x NCS					NCS x CS					CS x CS				
Phase Match	A_s	Phase Mismatch	A_t	R_{area}	Phase Match	A_s	Phase Mismatch	A_t	R_{area}	Phase Match	A_s	Phase Mismatch	A_t	R_{area}
A x A	$4h^2$	2(A x B)	$4h^2$	0.160	A x A	$4h^2$	3(A x B)	$6h^2$	0.200	A x A	$4h^2$	4(A x B)	$8h^2$	0.222
B x B	h^2	2(B x C)	$4h^2$	0.160	2(B x B)	$2h^2$	3(B x C)	$6h^2$	0.200	4(B x B)	$4h^2$	4(B x C)	$8h^2$	0.222
C x C	$4h^2$	2(A x C)	$8h^2$	0.320	C x C	$4h^2$	2(A x C)	$8h^2$	0.267	C x C	$4h^2$	2(A x C)	$8h^2$	0.222

* Area is calculated using ideal layer thicknesses $h_A = h_C = 2h_B \equiv 2h$.

Table 2.6 Energy Penalty Ratios for Twist Grain Boundaries in Ideal ABC/ac NCS Lamellar Blend

Scenario 1				Scenario 2				Scenario 3				Scenario 4			
R_{energy}		$R_{penalty}$		R_{energy}		$R_{penalty}$		R_{energy}		$R_{penalty}$		R_{energy}		$R_{penalty}$	
A x B	1	NCS x NCS	0.640	A x B	1	NCS x NCS	0.400	A x B	0.5	NCS x NCS	0.400	A x B	0.5	NCS x NCS	0.480
B x C	1	NCS x CS	0.667	B x C	0.5	NCS x CS	0.433	B x C	1	NCS x CS	0.433	B x C	0.5	NCS x CS	0.467
A x C	1	CS x CS	0.667	A x C	0.5	CS x CS	0.444	A x C	0.5	CS x CS	0.444	A x C	1	CS x CS	0.444

Table 2.7 Interfacial Area Ratios for Twist Grain Boundaries in SBIC/sc NCS Lamellar Blend

NCS x NCS					NCS x CS					CS x CS				
Phase Match	A_s	Phase Mismatch	A_i	R_{area}	Phase Match	A_s	Phase Mismatch	A_i	R_{area}	Phase Match	A_s	Phase Mismatch	A_i	R_{area}
W x W	100	2(W x B)	240	0.175	W x W	90	3(W x B)	348	0.181	W x W	81	4(W x B)	432	0.160
B x B	144	2(B x G)	360	0.263	2(B x B)	288	3(B x G)	588	0.305	4(B x B)	576	4(B x G)	912	0.337
G x G	225	2(W x G)	300	0.219	G x G	285	2(W x G)	325	0.169	G x G	361	2(W x G)	342	0.127

* Area is in units of nm^2.

Table 2.8 Solubility Parameters and Interfacial Energy Ratios for Twist Grain Boundaries in SBIC/sc NCS Lamellar Blend

Polymer Phase	δ	Phase Mismatch	Δδ	R_{energy}
PS (W)	18.6	W x B	1.5	1
PB/PI (B)	17.1	B x G	0.4	0.267
PCHD (G)	17.5	W x G	1.1	0.733

* Solubility parameter δ is in units of $MPa^{1/2}$.
δ_{PS} and $\delta_{P(B/I)}$ are measured values from ref 22.
δ_{PCHD} is determined from measured δ_{PS} from ref 22 and calculated $\Delta\delta_{SC}$ from ref 19.

Table 2.9 Energy Penalty Ratios for Twist Grain Boundaries in SBIC/sc NCS Lamellar Blend

Scenario 1				Scenario 2			
R_{energy}		$R_{penalty}$		R_{energy}		$R_{penalty}$	
W x B	1	NCS x NCS	0.657	W x B	1	NCS x NCS	0.406
B x G	1	NCS x CS	0.655	B x G	0.267	NCS x CS	0.386
W x G	1	CS x CS	0.624	W x G	0.733	CS x CS	0.342

Table 2.10 Volume Fractions for Respective Phases in SBIC/sc NCS Lamellar Blend and SBT/st NCS Lamellar Blend

Blend	ϕ_{PS} (%)	$\phi_{PB\ PI}$ or ϕ_{PB} (%)	ϕ_{PCHD} or ϕ_{PtBMA} (%)
SBIC/sc	27	32	41
SBT/st	38	23	39

ϕ_x: the volume fraction of x in the respective blend.
PS: polystyrene.
PB: polybutadiene.
PI: polyisoprene.
PCHD: polycyclohexadiene.
PtBMA: poly(*tert*-butyl methacrylate).

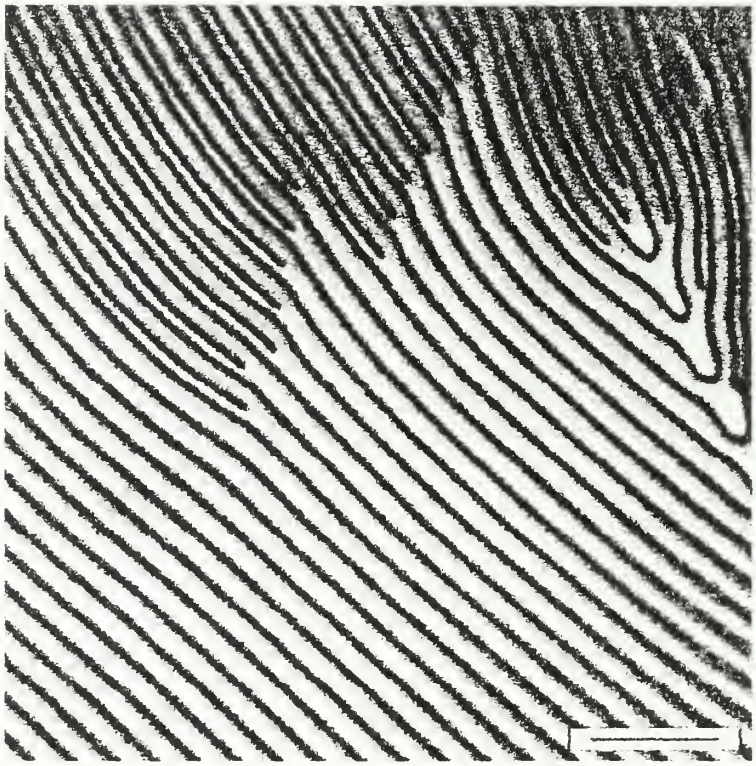

Figure 2.1 TEM morphology of a self-assembled lamellar blend of a triblock terpolymer (PS-*b*-PB-*b*-P*t*BMA, SBT) and a diblock copolymer (PS-*b*-P*t*BMA, st). Top: CS lamellae: Bottom: NCS lamellae. Scale bar: 250 nm.

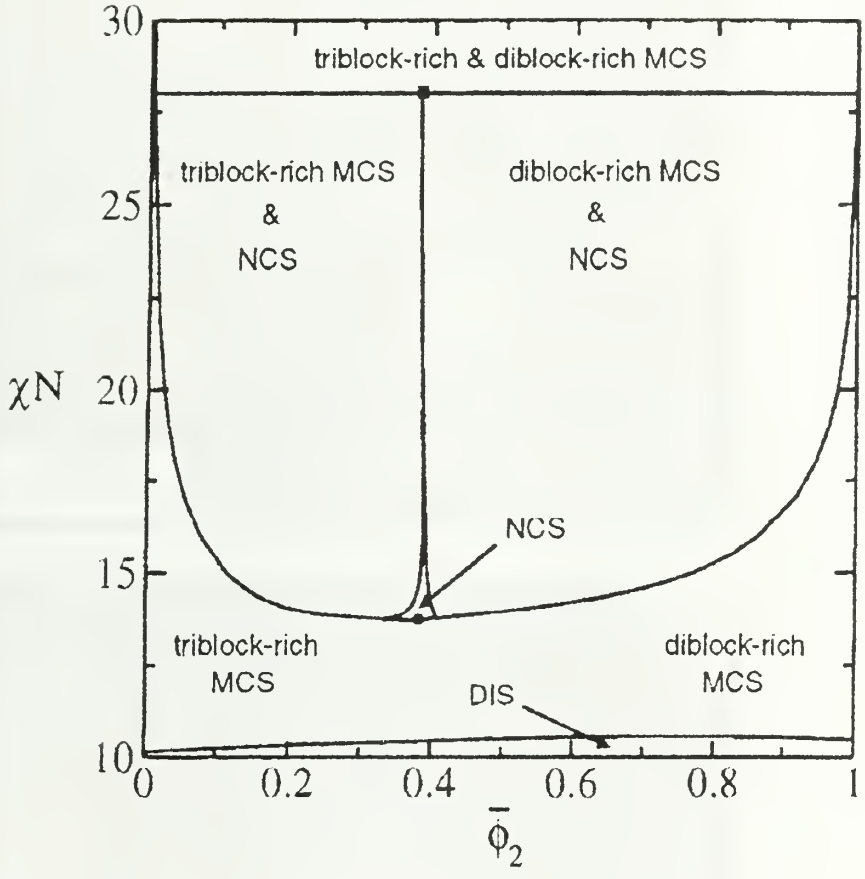

Figure 2.2 Phase diagram of ABC/ac lamellar blend. ϕ_2: Average diblock volume fraction. Ω: Ratio of triblock to diblock lengths. MCS: Mixed centrosymmetric. NCS: Noncentrosymmetric. DIS: Disordered.

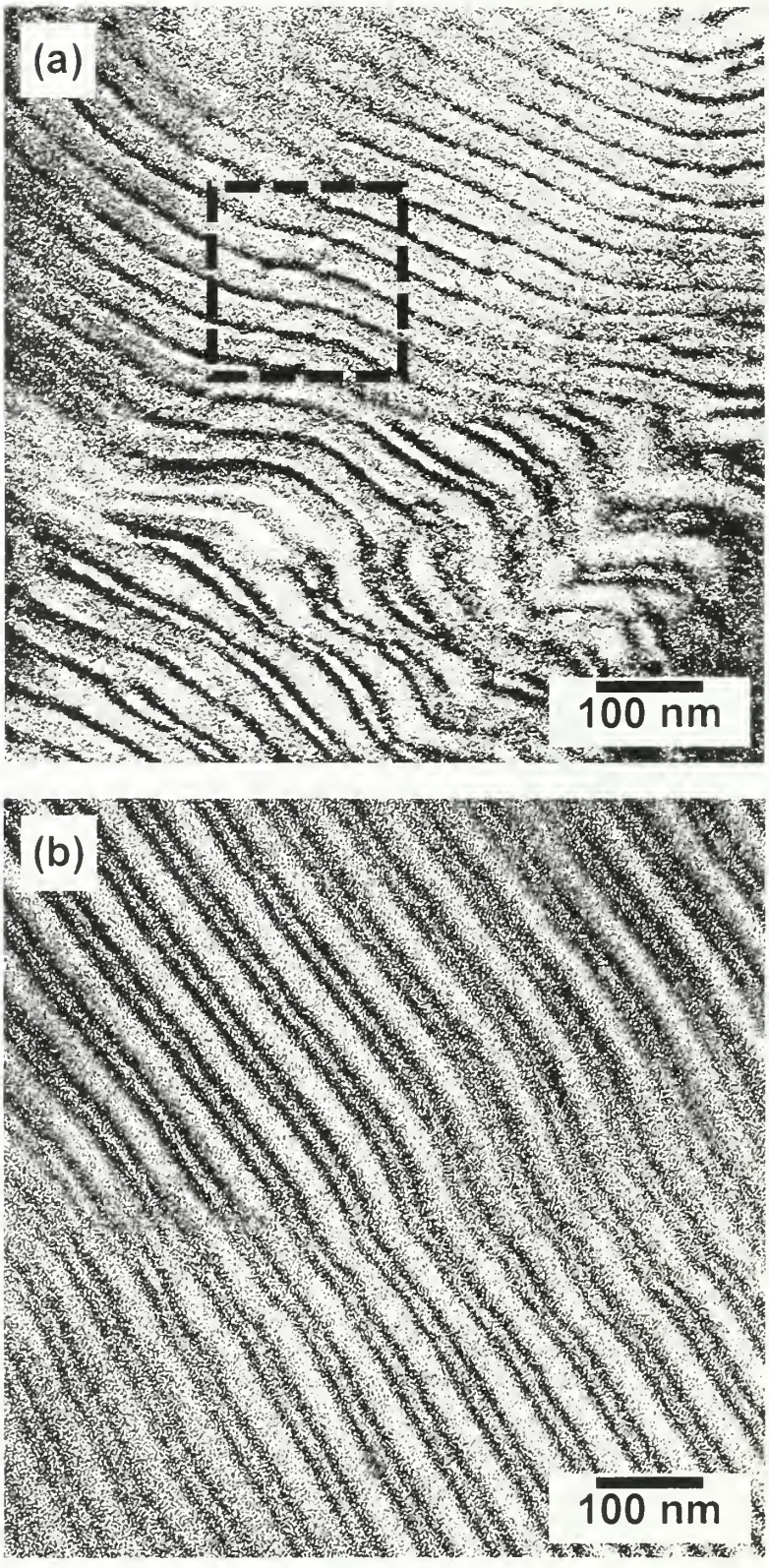

Figure 2.3 TEM morphologies of (a) SBIC/sc equimolar lamellar blend and (b) SBIC lamellar tetrablock copolymer.

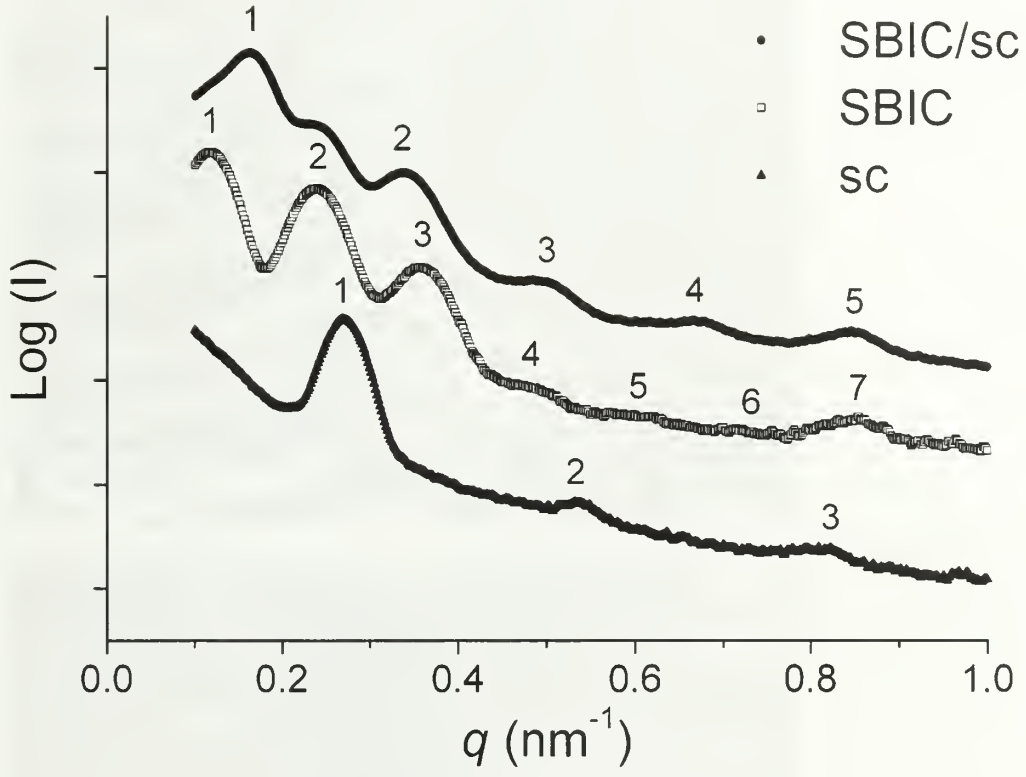

Figure 2.4 Small-angle X-ray scattering profiles of SBIC/sc NCS lamellar blend, SBIC CS lamellar tetrablock, and sc CS lamellar diblock copolymers.

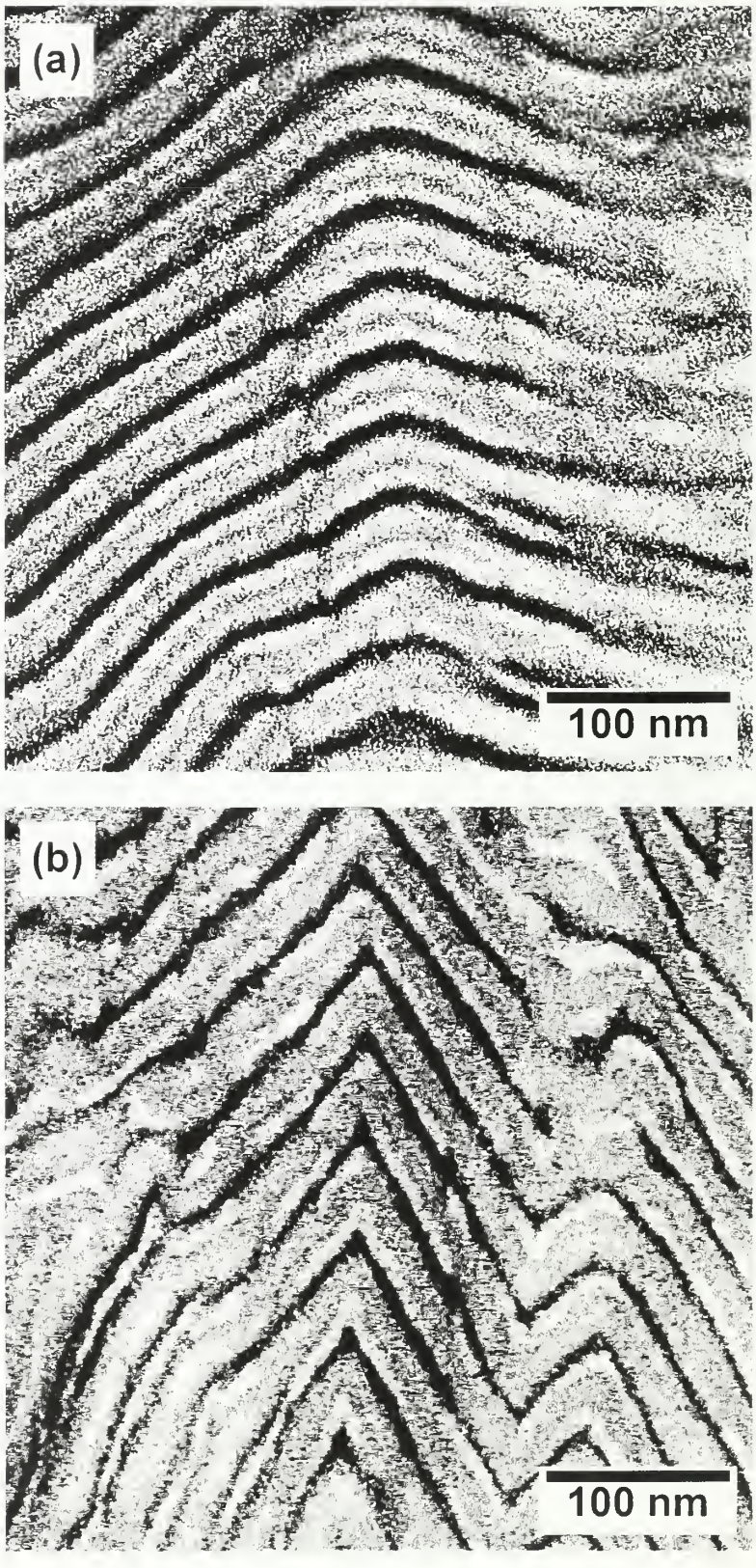

Figure 2.5 TEM morphologies of tilt grain boundaries in SBIC/sc NCS lamellar blend. (a) Chevron tilt boundary: (b) Omega tilt boundary.

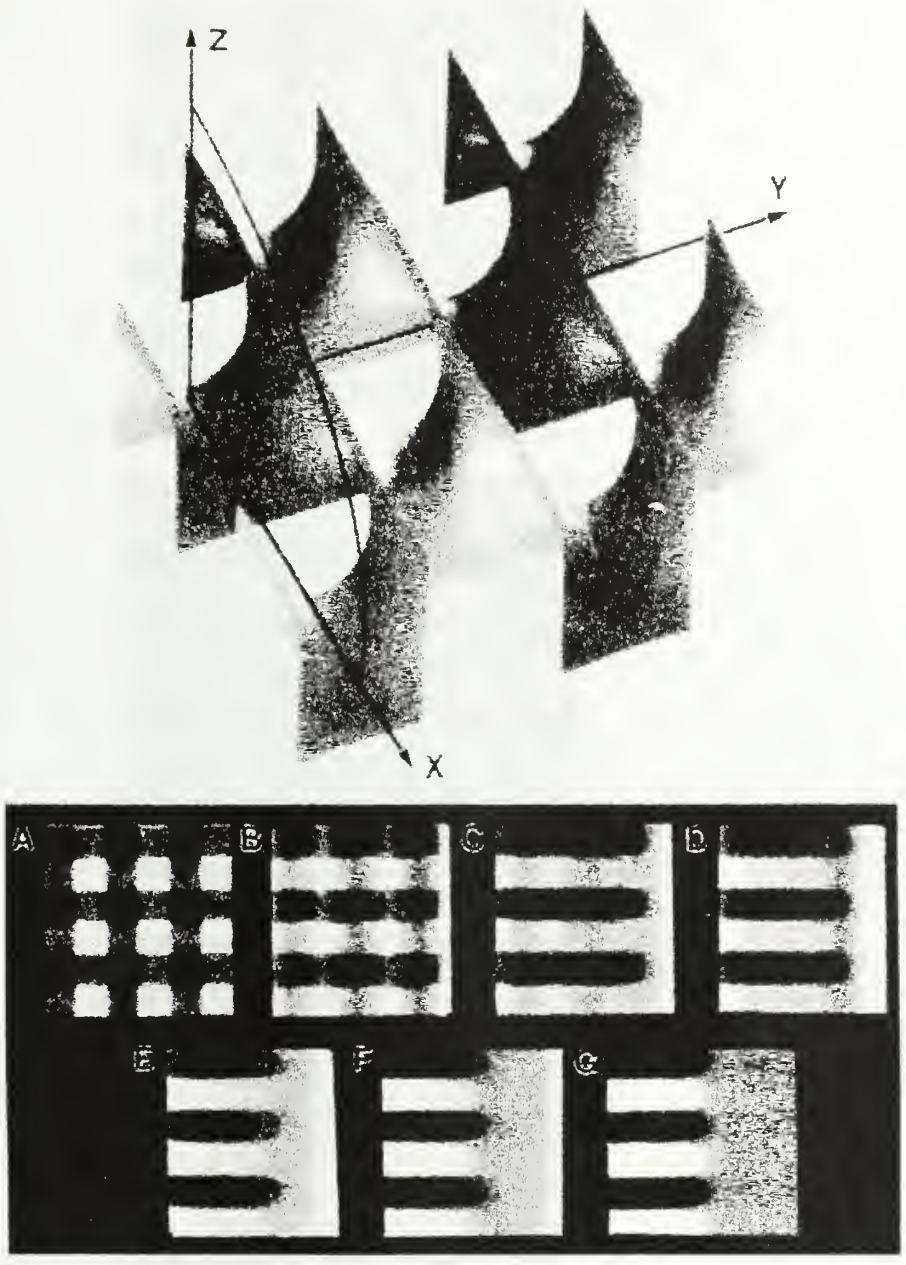

Figure 2.6 The Scherk twist grain boundary in CS lamellar diblock systems. (a) Model showing its characteristic doubly periodic saddle surfaces: (b) Computer ray tracing simulation of a TEM tilt series of this boundary.

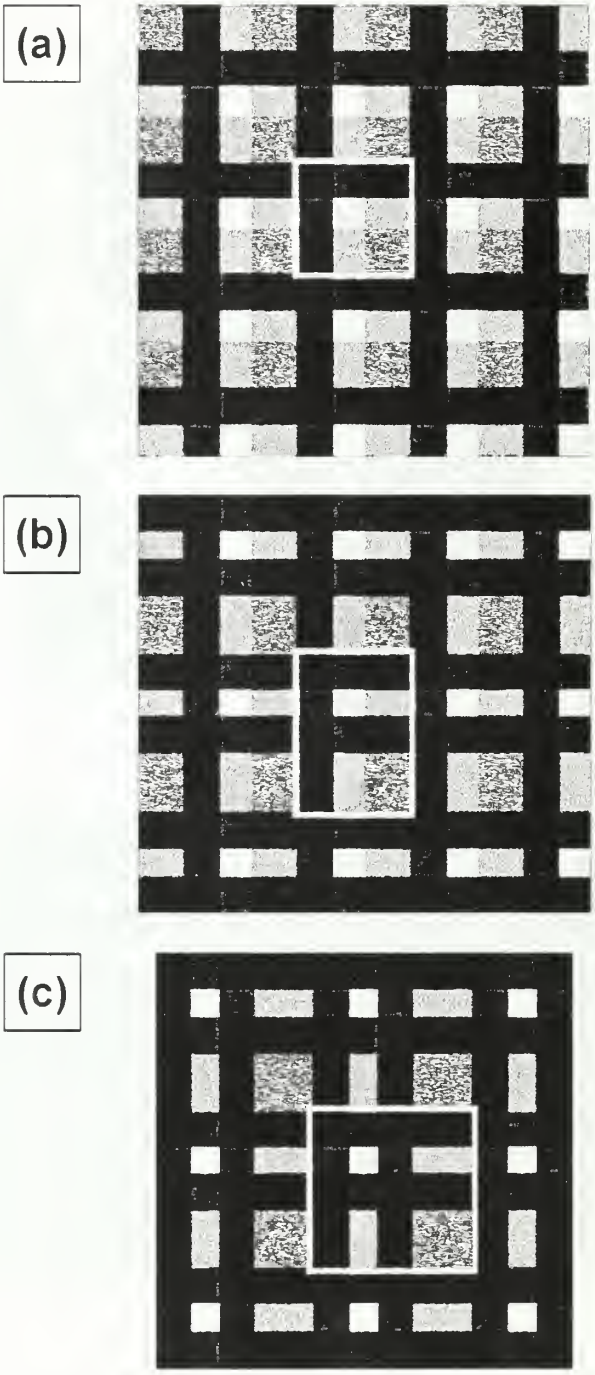

Figure 2.7 Simulated twist grain boundary crossing patterns in ABC/ac NCS lamellar blend. (a) NCS-NCS crossing pattern: (b) NCS-CS crossing pattern: (c) CS-CS crossing pattern. Unit cells are marked by white boxes.

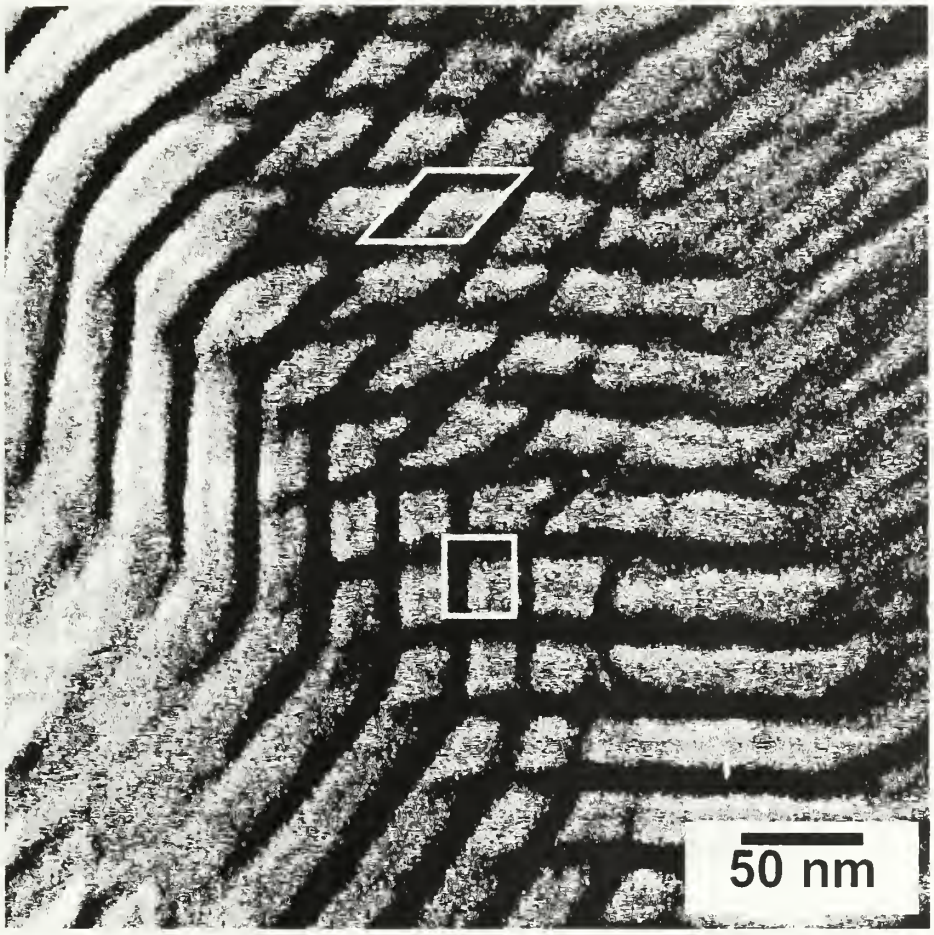

Figure 2.8 TEM morphology of NCS-NCS twist grain boundary in SBIC/sc NCS lamellar blend. Two unit cells are highlighted by white boxes. Upper: non-orthogonal: Lower: orthogonal.

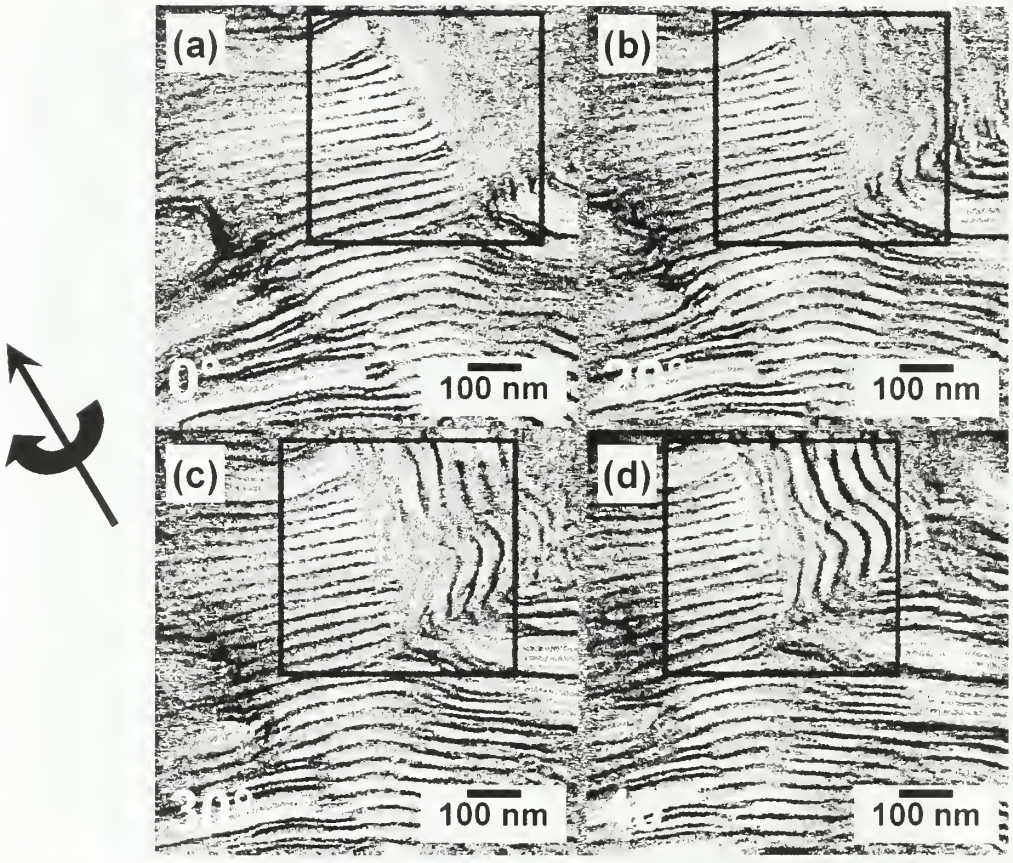

Figure 2.9 TEM tilt series of an NCS-NCS twist grain boundary in SBIC/sc NCS lamellar blend. Tilt boundary and tilting direction are marked by the straight and curved arrows on the left. (a) No tilt: (b) 20° tilt: (c) 30° tilt: (d) 40° tilt.

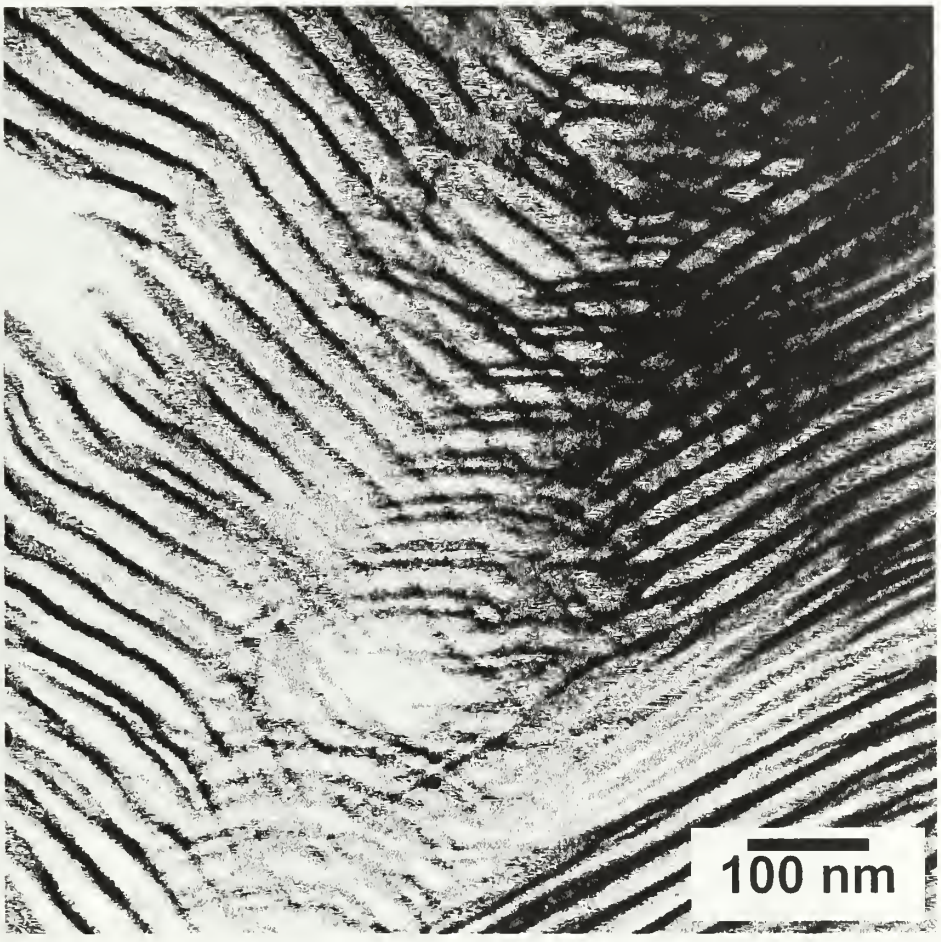

Figure 2.10 TEM morphology of NCS-CS twist grain boundary in SBIC/sc NCS lamellar blend.

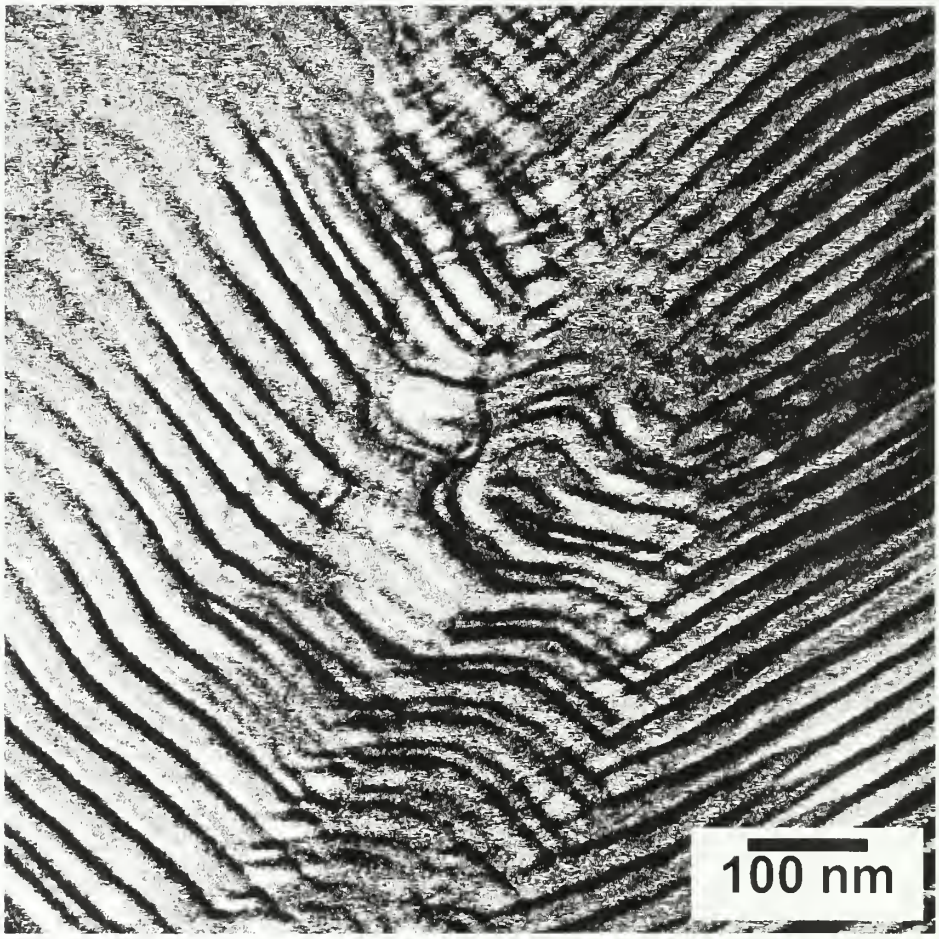

Figure 2.11 TEM morphology of CS-CS twist grain boundary in SBIC/sc NCS lamellar blend.

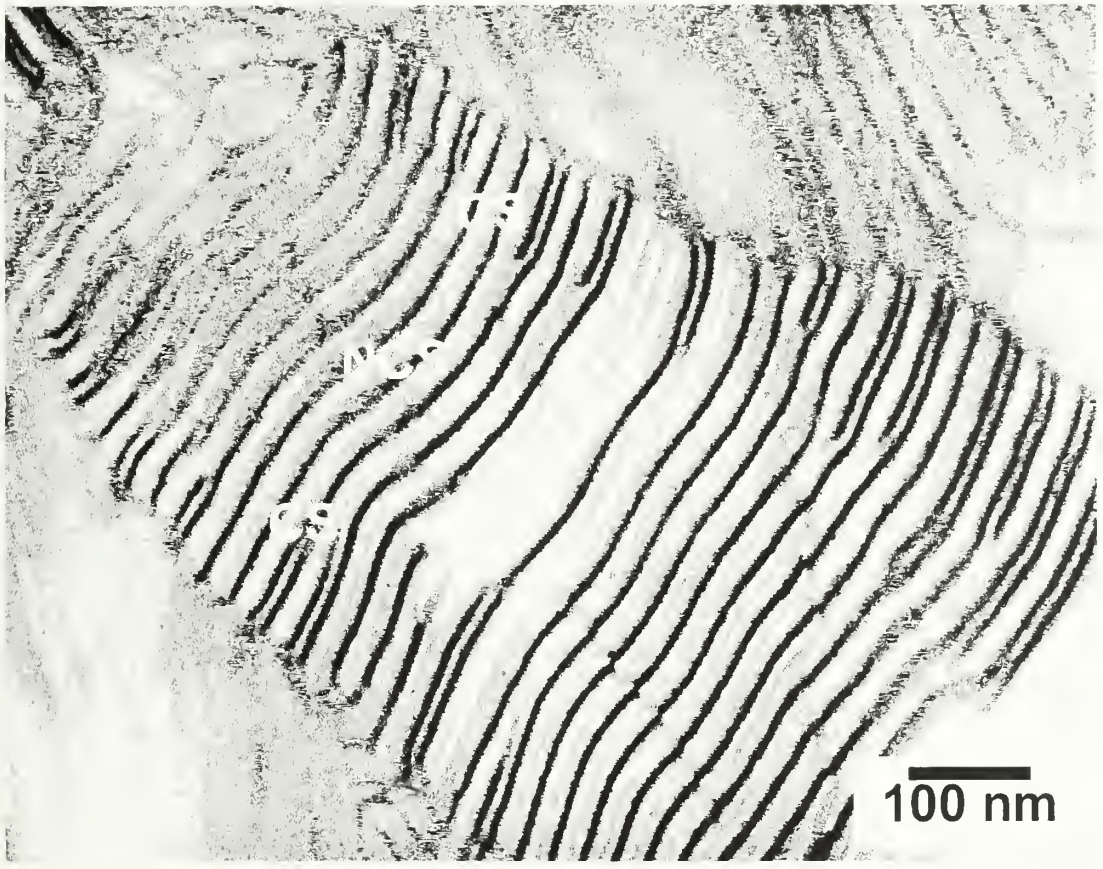

Figure 2.12 TEM micrograph showing transition from NCS to CS lamellae as the layers approach twist grain boundaries (upper and lower) in the SBIC/sc NCS lamellar blend.

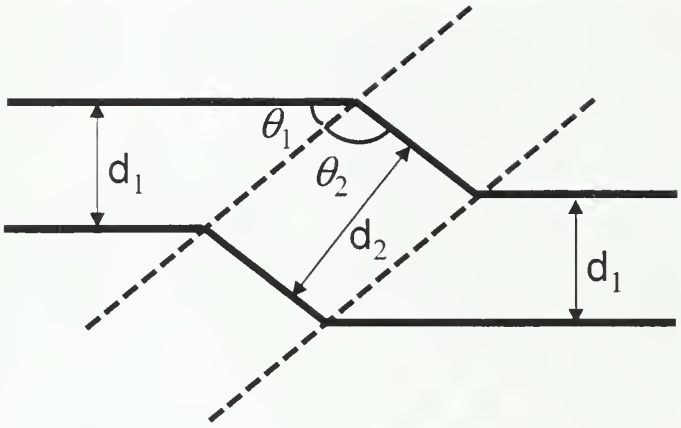

Figure 2.13 Structure of a kink band.

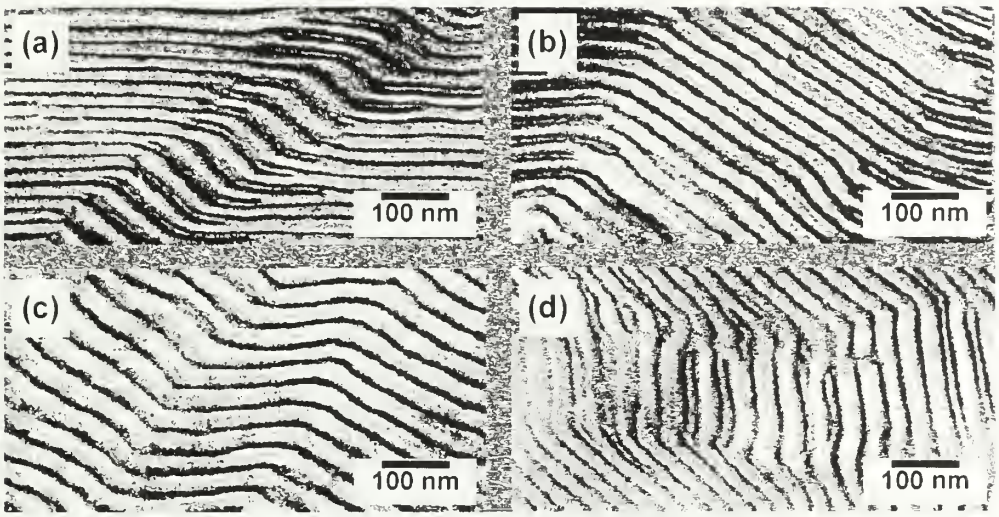

Figure 2.14 TEM micrographs showing different types of NCS kink bands. (a) NCS→CS→NCS: (b) CS→NCS→CS: (c) NCS→NCS→NCS: (d) NCS→Mixed→NCS.

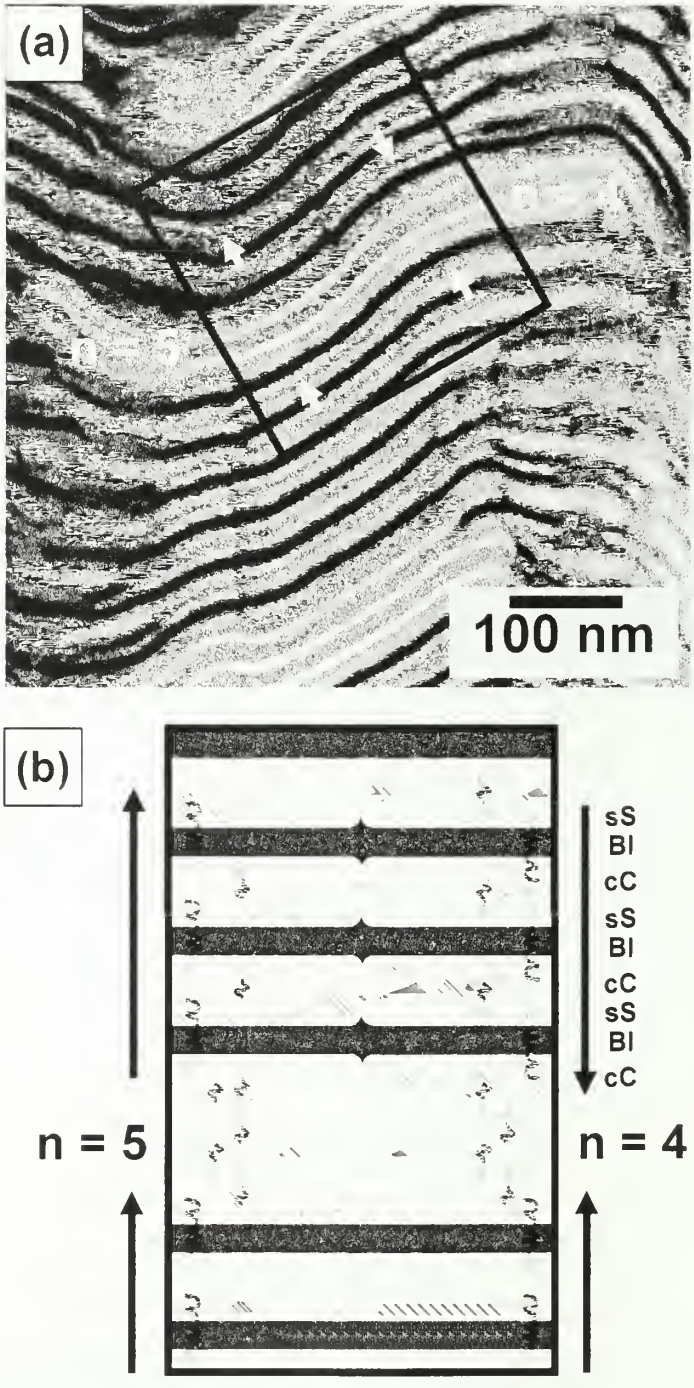

Figure 2.15 Polarity reversals normal to NCS layers. (a) Representative TEM morphology in SBIC/sc NCS lamellar blend. (b) Cartoon depicting the defect structure inside the boxed area in (a).

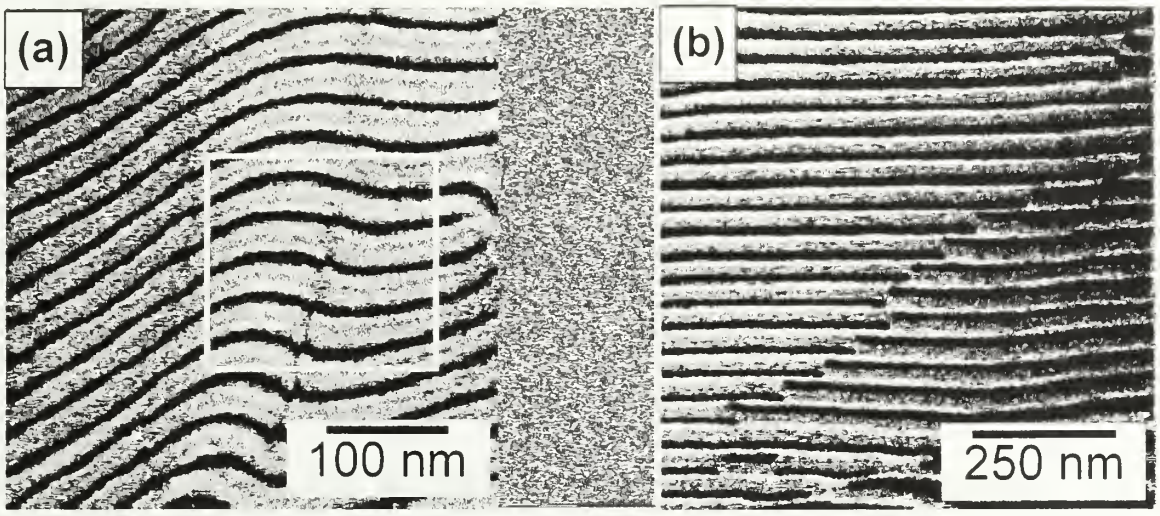

Figure 2.16 Polarity reversals parallel to NCS layers. (a) Representative TEM morphology in SBIC/sc NCS lamellar blend: (b) Representative TEM morphology in SBT/st NCS lamellar blend.

CHAPTER 3

MORPHOLOGY OF POLY(TERT-BUTYL VINYL ETHER-BLOCK-ISOBUTYLENE-BLOCK-TERT-BUTYL VINYL ETHER) TRIBLOCK COPOLYMERS

3.1 Abstract

A series of poly(*tert*-butyl vinyl ether-*b*-isobutylene-*b*-*tert*-butyl vinyl ether) triblock copolymers with narrow MWDs (<1.1) were prepared through living cationic polymerization using a difunctional initiator. It was carried out by the so-called capping-tuning technique, involving the capping of living PIB chain ends with 1,1-ditolylethylene (DTE) followed by addition of titanium(IV) isopropoxide ($Ti(OIp)_4$) to lower the Lewis acidity before the introduction of *t*BVE. Differential scanning calorimetry (DSC) of the block copolymers showed two glass transitions demonstrating microphase separation. The triblock copolymers with 23–39 wt % P*t*BVE content exhibited typical characteristics of a thermoplastic elastomer (TPE) with tensile strengths of 9–15 MPa and elongations at break of 760–1300%. Morphological studies by transmission electron microscopy (TEM), small-angle X-ray scattering (SAXS), and atomic force microscopy (AFM) revealed lamellar or cylindrical morphologies of the triblock copolymers, depending on their molecular compositions.

3.2 Introduction

Since the discovery of living cationic polymerization in the mid-1980s,[1,2] virtually all cationically polymerizable monomers have been polymerized in living cationic

polymerization including isobutylene, vinyl ethers, styrene and its derivatives, and N-vinyl carbazole.[3-5] Based on these monomers, new families of pendant or terminal functional polymers, macromonomers, linear block copolymers (AB, ABA, ABC, etc.), nonlinear block copolymers (graft, star, star block, miktoarm star etc.), and other polymers with well-defined architectures were created.

ABA triblock copolymers with polyisobutylene (PIB) as the rubbery center segment and glassy polymers as end segments, made available by living cationic polymerization, constitute a novel type of thermoplastic elastomers (TPEs), which offer improved thermal and oxidative stability over diene based TPEs. Following the successful synthesis of poly(styrene-*b*-isobutylene-*b*-styrene),[6] various styrenic monomers such as indene,[7] p-methylstyrene (pMeSt),[8] and α-methylstyrene (αMeSt)[9] were used instead of styrene to incorporate polymers with higher T_g as end segments to improve the mechanical properties and upper service temperature of PIB based TPEs.

Poly(alkyl vinyl ether)s are attractive as end segments as vinyl ethers can be polymerized by living cationic polymerizations, thus poly(alkyl vinyl ether-*b*-isobutylene-*b*-alkyl vinyl ether) triblock copolymers could be prepared in a one-pot process without the complication of mechanistic transformation. These ABA triblock copolymers with high T_g end segments should be useful TPEs. Even more intriguing, however, is the opportunity that selected poly(alkyl vinyl ether)s, e.g., benzyl-, trimethylsilyl- and *tert*-butyl vinyl ethers could be hydrolyzed to poly(vinyl alcohol) (PVA), a polar semicrystalline polymer. However, due to the vast difference in reactivity

between vinyl ethers and isobutylene.[4] direct sequential monomer addition is not feasible for the preparation of well defined block copolymers.[15]

In a series of publications from Faust and coworkers[8,18-21] a new strategy was reported for the synthesis of block copolymers by living cationic sequential block copolymerization when the second monomer is more reactive than the first one. It involves capping of PIB chain ends with 1,1-diphenyl ethylene (DPE) or 1,1-ditolyl ethylene (DTE) followed by lowering the Lewis acidity to match the reactivity of the second monomer.

Poly(*tert*-butyl vinyl ether), which has a T_g of 88 °C.[22] has long been prepared by cationic polymerization as a precursor to poly(vinyl alcohol).[23] To the best of our knowledge, there has been no report on the synthesis or morphology of PIB based TPEs with poly(vinyl ether)s as the end segments. In this chapter, morphology of a series of poly(*tert*-butyl vinyl ether-*b*-isobutylene-*b*-*tert*-butyl vinyl ether) (P*t*BVE-PIB-P*t*BVE) triblock copolymers was studied. The triblock copolymers are expected to be thermoplastic elastomers and precursors to poly(vinyl alcohol-*b*-isobutylene-*b*-vinyl alcohol).

3.3 Experimental Section

3.3.1 Materials

A series of well-defined poly(*tert*-butyl vinyl ether-*b*-isobutylene-*b*-*tert*-butyl vinyl ether) (P*t*BVE-PIB-P*t*BVE) triblock copolymers with approximately constant PIB

molecular weight and different compositions were synthesized through living cationic polymerization in hexane/CH_3Cl solvent system at –80 °C. It was carried out by the so-called capping-tuning technique, involving the capping of living PIB chain ends with 1,1-ditolylethylene (DTE) followed by addition of titanium(IV) isopropoxide ($Ti(OIp)_4$) to lower the Lewis acidity before the introduction of *t*BVE. The chemical structure of the triblock copolymers is shown in Figure 3.1.

3.3.2 Sample Preparation

Solid films approximately 1 mm thick of the triblock copolymers were slowly cast from 5 wt % polymer solutions in toluene, a nonpreferential solvent. Casting was performed at room temperature, and the evaporation of solvent was controlled to form a solid film after 7–10 days. The films were given another week under high vacuum at room temperature in order to remove residual solvent. The samples were then annealed for 1 week under high vacuum at 100 °C in order to further promote the approach to an equilibrium structure.

3.3.3 Transmission Electron Microscopy (TEM)

After annealing, samples for electron microscopy were cryo-microtomed in a Leica ultramicrotome. Sections approximately 40–60 nm thick were cut with a Diatome diamond knife at a sample temperature of –85 °C and a knife temperature of –85 °C. The sections were stained in RuO_4 vapors for about 4 hours. TEM was performed on a JEOL 2000FX transmission electron microscope operated at 200 kV accelerating voltage.

3.3.4 Small Angle X-ray Scattering (SAXS)

SAXS experiments were performed on annealed films using a Molecular Metrology 2D SAXS instrument powered by a high brilliance Osmic Max-Flux source with Cu Kα sealed-tube X-ray radiation and pinhole collimation. Patterns were collected digitally with a 2D multiwire detector and analyzed with a FAST ComTec MPA-3 multichannel analyzer and custom-written software. Extraneous background scatter was subtracted, and the data was plotted on a logarithmic scale. Circular averaging was performed to produce a plot of intensity vs. scattering angle, q.

3.3.5 Atomic Force Microscopy (AFM)

AFM experiments were done on unannealed films of the triblock copolymers spin coated on Si wafers, with a Digital Instruments D3100 scanning force microscope in the tapping mode. To be consistent with TEM and SAXS experiments, 5 wt % toluene solutions were used for the spin coating of the triblock copolymers, resulting in a polymer film thickness of about 200 nm.

3.4 Results and Discussion

3.4.1 Molecular Characterization

The GPC traces of a representative triblock copolymer (sample A) and the PIB precursor are shown in Figure 3.2. The M_ns, molecular weight distributions (MWDs), and compositions are summarized in Table 3.1. The experimental and theoretical M_ns were very close, and the narrow MWDs of the products suggest that well-defined triblock copolymer were obtained. The composition of the triblock copolymers, as calculated by

^{1}H NMR spectroscopy, agreed well with the feed composition, indicating the complete conversions of both IB and *t*BVE. The volume fractions of the P*t*BVE blocks were calculated on the basis of the measured density of P*t*BVE, 0.957 g/cm^3, and known density of PIB.[37] The density of P*t*BVE was measured using the displacement method by submerging a compression-molded sample of P*t*BVE homopolymer into *n*-butanol, a nonsolvent, according to ASTM D792.

3.4.2 Thermal Transitions

A DSC scan of a representative triblock copolymer (sample A) is shown in Figure 3.3. The two glass transitions at ~ −64 °C (T_g of PIB) and ~ 74 °C (T_g of P*t*BVE) clearly indicate microphase separation.

3.4.3 Mechanical Properties

The tensile properties of the triblock copolymers have been determined, and the results are summarized in Table 3.2. The TPE characteristics are shown by the tensile strengths of 9–15 MPa and elongations at break of 760–1300%. At low strains (<500%), the modulus increased with increasing P*t*BVE content. Compared to PSt-PIB-PSt of similar compositions, the tensile strength of P*t*BVE-PIB-P*t*BVE is somewhat lower and the ultimate elongation higher.

3.4.4 Morphology

The results from the morphological characterization confirm the microphase separation behavior of the triblock copolymers. More specifically, samples A and B,

with 0.38 and 0.32 combined volume fractions for the two P*t*BVE blocks, respectively, yield lamellar morphologies. Sample C, with a combined volume fraction of 0.22 for the two P*t*BVE blocks, yields a cylindrical morphology.

Shown in Figure 3.4 are three representative TEM micrographs of the triblock copolymers, in all of which the dark phase is P*t*BVE and the light phase is PIB, due to the selective staining of P*t*BVE blocks by RuO_4. RuO_4 has been known to be a good staining agent for poly(methyl vinyl ether) (PMVE),[38] but its staining effect on P*t*BVE has not yet been reported. Our experimental results showed that RuO_4 could selectively stain the P*t*BVE blocks in the triblock copolymers, but the staining time was much longer, about 4 hours, than that needed to stain PMVE, about 15 minutes.[38]

Figure 3.4a shows a well-ordered area of lamellae in sample A, with an apparent lamellar long period (L) of 17 nm. The area shown comes from a lamellar grain of larger than 1 μ x 1 μ in size, demonstrating the good long-range order in this sample. Figure 3.4b shows several grains of lamellae in sample B, including an omega tilt grain boundary defect[38] in the upper left corner of the TEM micrograph. The volume fraction of sample B, 0.32, falls in the volume fraction range where cylindrical morphology would normally be expected. The presence of the omega tilt grain boundary, which is a common defect among lamellar grains, supports the assignment of a lamellar morphology to sample B. The apparent lamellar long period (L) of sample B is 16 nm. In both Figures 3.4a and 3.4b, the light PIB layers look narrower than the volume fractions of PIB (0.62 and 0.68, respectively) would suggest. This is probably due to the shrinkage of

the PIB layers in the electron beam during TEM observation, since PIB is a known beam-sensitive material. Figure 3.4c shows a poorly ordered cylindrical morphology in sample C. In the top-center of the image, the projection is approximately down the cylinder axis, while on both sides of the image the projection is approximately perpendicular to the cylinder axis. This TEM image indicates a d_{10} spacing of about 21 nm. Here, again the dark P*t*BVE cylinders look larger than the 0.22 volume fraction of P*t*BVE would suggest, most likely due to the shrinkage of PIB matrix in the electron beam.

SAXS patterns of the triblock copolymers are shown in Figure 3.5. Figure 3.5a shows the SAXS pattern of sample A, having three observable reflections with ratios q_n/q^*, of the nth reflection scattering vector to the first reflection scattering vector, of 2, 3 and 4. In this figure, the 1st order reflection is very weak, but the ratios of the other, stronger peaks and the comparison to TEM data supports our lamellar morphological assignment and the peak assignment given in the figure. Figure 3.5b shows the SAXS pattern of sample B, with two strong reflections, corresponding to its 3rd and 4th order X-ray reflections, as well as a shoulder, corresponding to the 1st order reflection. The presence of reflection ratios of 1, 3 and 4 further confirms the lamellar morphology of sample B. The lamellar long periods (L) of sample A and sample B, based on the q^* values in SAXS, are 39 nm and 38 nm, respectively. These values are much larger than those obtained from TEM. This may also be attributed to the beam shrinkage of PIB layers during TEM observation. This conclusion is supported by AFM images on thin films, not shown, which give domain spacings for samples A and B which are in agreement with the SAXS data rather than with the smaller spacings observed via TEM.

Figure 3.5c shows the SAXS pattern of sample C, where there are four strong reflections with q_n/q^* ratios of 1, $\sqrt{3}$, 2, and $\sqrt{7}$, which are indicative of a cylindrical morphology. The d_{10} value calculated from SAXS is 28 nm, again larger than the TEM value, but in agreement with AFM results.

Results from AFM experiments on unannealed thin films of the triblock copolymers showed poorly ordered lamellar morphologies for sample A and sample B, and a poorly ordered cylindrical morphology for sample C, consistent with our morphological assignments based on TEM and SAXS data. The poor ordering of the spin cast samples is due to the short spinning process during which the polymer chains did not have enough time to orient themselves to achieve good order. Nevertheless, the domain spacings measured from the AFM data on these unannealed films are good indicators of the domain spacings in the equilibrium state. The AFM values of the lamellar long periods for sample A and sample B, are 44 nm and 41 nm, respectively, in agreement with SAXS data. The AFM value of d_{10} for sample C, is 30 nm, also in agreement with SAXS data.

3.5 Conclusions

Efficient block copolymerization of IB with *t*BVE can be accomplished by living cationic polymerization in a one-pot capping-tuning process, which involves capping the living PIB chain ends with DTE followed by tuning the Lewis acidity by the addition of $Ti(OIp)_4$. Using an optimum $[Ti(OIp)_4]/[TiCl_4]$ ratio well-defined PIB-P*t*BVE diblock and P*t*BVE-PIB-P*t*BVE triblock copolymers with designed molecular weight and narrow

MWDs could be prepared, virtually without homopolymer contaminants. The triblock copolymers exhibited typical TPE properties with tensile strengths of 9–15 MPa and ultimate elongations of 760–1300 %. TEM, SAXS and AFM results suggested that samples with P*t*BVE volume fractions of 0.38 and 0.32 yield lamellar morphologies, and the sample with 0.22 P*t*BVE volume fraction exhibits cylindrical morphology.

3.6 References

(1) Miyamoto, M.; Sawamoto, M.; Higashimura, T. *Macromolecules* **1984**, *17*, 265–268.

(2) Faust, R.; Kennedy, J. P. *Polym. Bull.* **1986**, *15*, 317–323.

(3) Kennedy, J. P.; Iván, B. *Designed Polymers by Carbocationic Macromolecular Engineering: Theory and Practice*; Hanser Publishers: Munich, 1992.

(4) Matyjaszewski, K., Ed. *Cationic Polymerizations, Mechanisms, Synthesis and Application*; Marcel Dekker: New York, 1996.

(5) Puskas, J. E.; Kaszas, G. *Prog. Polym. Sci.* **2000**, *25*, 403–452.

(6) (a) Kaszas, G.; Puskas J. E.; Kennedy, J. P.; Hager, W. G. *J. Polym. Sci. Part A: Polym. Chem.* **1991**, *29*, 427–435. (b) Storey, R. F.; Chisholm, B. J. *Macromolecules* **1993**, *26*, 6727–6733. (c) Gyor, M.; Fodor, Z.; Wang, H.-C.; Faust, R. *J. Macromol. Sci.* **1994**, *A31* (12), 2055–2065.

(7) Kennedy, J. P.; Midha, S.; Tsunogal, Y. *Macromolecules* **1993**, *26*, 429–435.

(8) Fodor, Z.; Faust, R. *J. Macromol. Sci., Pure Appl. Chem.* **1995**, *A32* (3), 575–591.

(9) Li, D.; Faust, R. *Macromolecules* **1995**, *28*, 4893–4898.

(10) Sipos, L.; Zsuga, M.; Deák, G. *Macromolecular Rapid Communication* **1995**, *16*, 935–940.

(11) Kwon, Y.; Faust, R. *Macromolecules* **2002**, *35*, 3348–3357.

(12) Kim, M. S.; Faust, R. *Polym. Bull.* **2002**, *48*, 127–134.

(13) Coca, S.; Matyjaszewski, K. *J. Polymer. Sci. Part A: Polym. Chem.* **1997**, *35*, 3595–3601.

(14) Feldthusen, J.; Iván, B.; Müller, A. H. E. *Macromolecules* **1998**, *31*, 578–585.

(15) Bae, Y. C.; Hadjikyriacou, S.; Schlaad, H.; Faust, R. In *Ionic Polymerization and Related Processes*; Puskas J. E., Ed.; Kluwer Academic Publishers: Dordrecht, Germany, 1999.

(16) Lubnin, A. V.; Kennedy, J. P. *J. Polym. Sci. Part A: Polym. Chem.* **1993**, *31*, 2825–2834.

(17) Kurian, J. Ph.D. Thesis, The University of Akron, **1991**.

(18) Fodor, Z.; Faust, R. *J. Macromol. Sci., Pure Appl. Chem.* **1994**, *A31* (12), 1985–2000.

(19) Hadjikyriacou, S.; Faust, R. *Macromolecules* **1996**, *29*, 5261–5267.

(20) Hadjikyriacou, S.; Faust, R. *Macromolecules* **1995**, *28*, 7893–7900.

(21) Li, D.; Faust, R. *Macromolecules* **1995**, *28*, 1383–1389.

(22) Fishbein, L.; Crowe, B. F. *Makromol. Chem.* **1961**, *48*, 221–228.

(23) Okamura, S.; Kodama, T.; Higashimura, T. *Makromol. Chem.* **1962**, *53*, 180–191.

(24) Ohgi, H.; Sato, T. *Macromolecules* **1999**, *32*, 2403–2409.

(25) Aoshima, S.; Iwasa, S.; Kobayashi, E. *Polym. J.* **1994**, *26* (8), 912–919.

(26) Roth, M.; Mayr, H. *Macromolecules* **1996**, *29*, 6104–6109.

(27) Gyor, M.; Wang, H.-C.; Faust, R. *J. Macromol. Sci., Pure Appl. Chem.* **1992**, *A29*, 639–653.

(28) Bae, Y. C.; Faust, R. *Macromolecules* **1998**, *31*, 2480–2487.

(29) Ledwith, A.; Lockett, E.; Sherrington, D. C. *Polymer* **1975**, *16*, 31–37.

(30) Pernecker, T.; Kennedy, J. P.; Ivan, B. *Macromolecules* **1992**, *25*, 1642–1647.

(31) Schlaad, H.; Kwon, Y.; Faust, R.; Mayr, H. *Macromolecules* **2000**, *33*, 743–747.

(32) Schlaad, H.; Kwon, Y.; Faust, R.; Charleux, B. *Macromolecules* **2000**, *33*, 8225–8232.

(33) Zhou, Y.; Faust, R. *Polymer Preprints* **2003**, *44* (2), 661–662.

(34) Hatada, K.; Kitayama, T.; Matsuo, N.; Yuki, H. *Polym. J.* **1983**, *15* (10), 719–725.

(35) Kawaguchi T.; Sanda, F.; Masuda, T. *J. Polymer. Sci. Part A: Polym. Chem.* **2002**, *40* (16), 3938–3943.

(36) Ouchi, M.; Kamigaito, M.; Sawamoto, M. *Macromolecules* ***1999***, *32*, 6407–6411.

(37) Brandrup, J.; Immergut, E. H.; Grulke, E. A.; Bloch, D., Eds. *Polymer Handbook*, 4th ed.; John Wiley & Sons: New York, 1999.

(38) Trent, J. S.; Scheinbeim, J. I.; Couchman P. R. *Macromolecules* **1983**, *16*, 589–598.

(39) Gido, S. P.; Thomas, E. L. *Macromolecules* **1994**, *27*, 6137–6144.

Table 3.1 Molecular Characteristics of the Triblock Copolymers

no.	PIB		triblock		size of P*t*BVE segments	P*t*BVE content (NMR)			P*t*BVE content (calcd from feed)		
	$10^{-3}M_n$	M_w/M_n	$10^{-3}M_n$	M_w/M_n		mol %	wt %	vol* %	mol %	wt %	vol* %
A	69.4	1.08	110.5	1.08	2 × 20,600	27	39	38	25	37	36
B	66.6	1.07	96.4	1.07	2 ×14,900	21	33	32	20	31	30
C	67.3	1.06	85.9	1.08	2 × 9,300	15	23	22	13	22	21

* Volume fractions were calculated using $d_{PtBVE} = 0.957$ g/cm^3 and $d_{PIB} = 0.915$ g/cm^3.

Table 3.2 Tensile Properties of the Triblock Copolymers

no.	100 % modulus (MPa)	200 % modulus (MPa)	300 % modulus (MPa)	400 % modulus (MPa)	500 % modulus (MPa)	tensile strength (MPa)	elongation at break (%)
A	2.34	2.93	4.31	5.65	7.24	12.52	760
B	1.59	1.97	2.94	4.32	6.08	15.11	800
C	0.90	1.18	1.38	1.46	1.93	9.16	1300

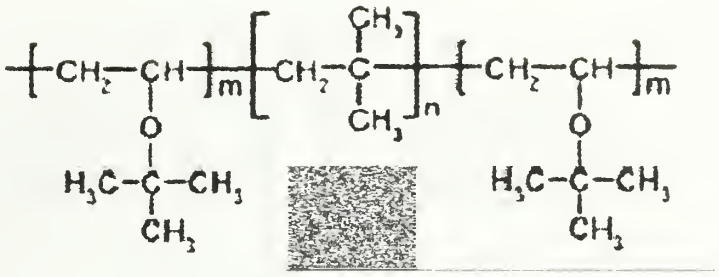

Figure 3.1 Chemical structure of P*t*BVE-*b*-PIB-*b*-P*t*BVE triblock copolymers.

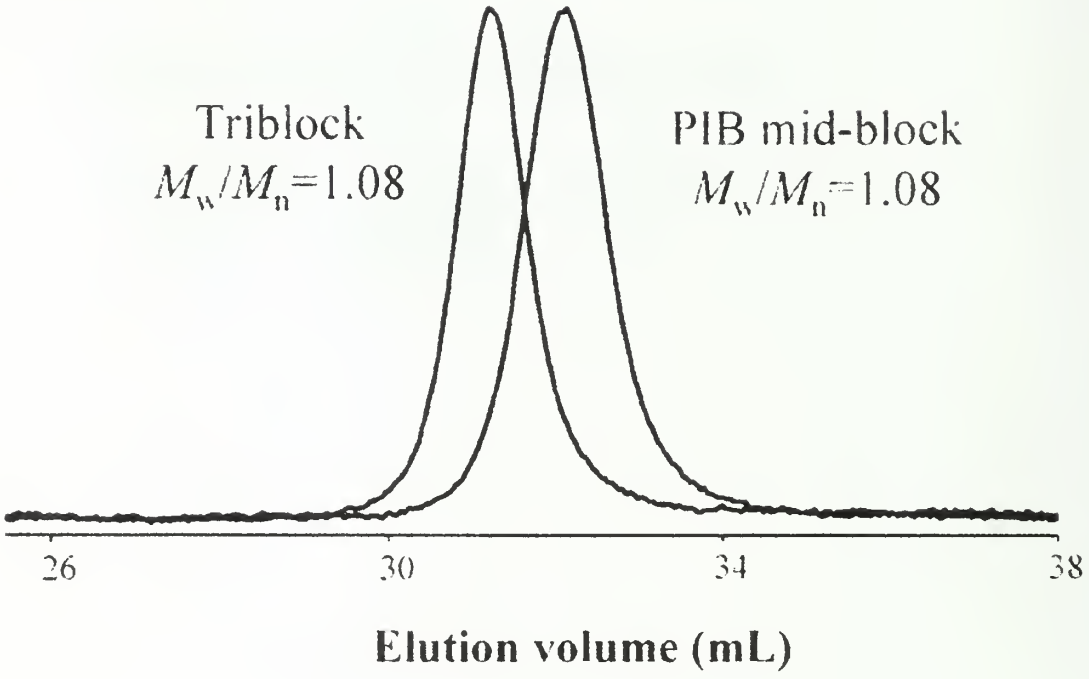

Figure 3.2 GPC RI traces of a representative P*t*BVE-*b*-PIB-*b*-P*t*BVE triblock copolymer (molecular weight 20 600–69 400–20 600) and starting PIB mid-block.

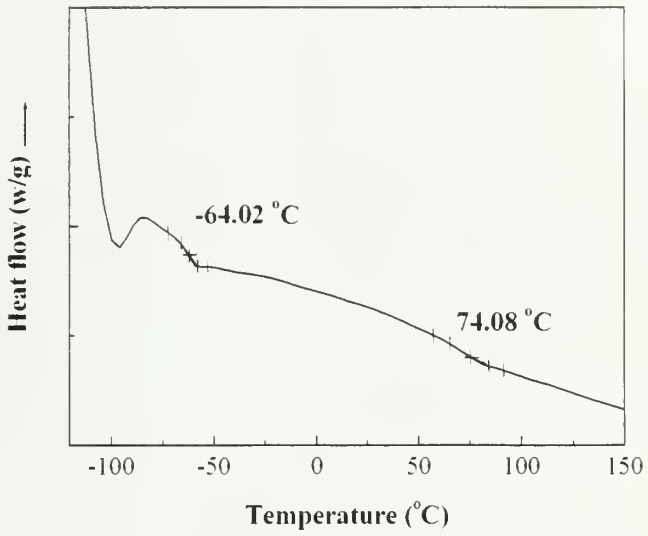

Figure 3.3 DSC scan of a representative P*t*BVE-*b*-PIB-*b*-P*t*BVE triblock copolymer (molecular weight 20 600–69 400–20 600).

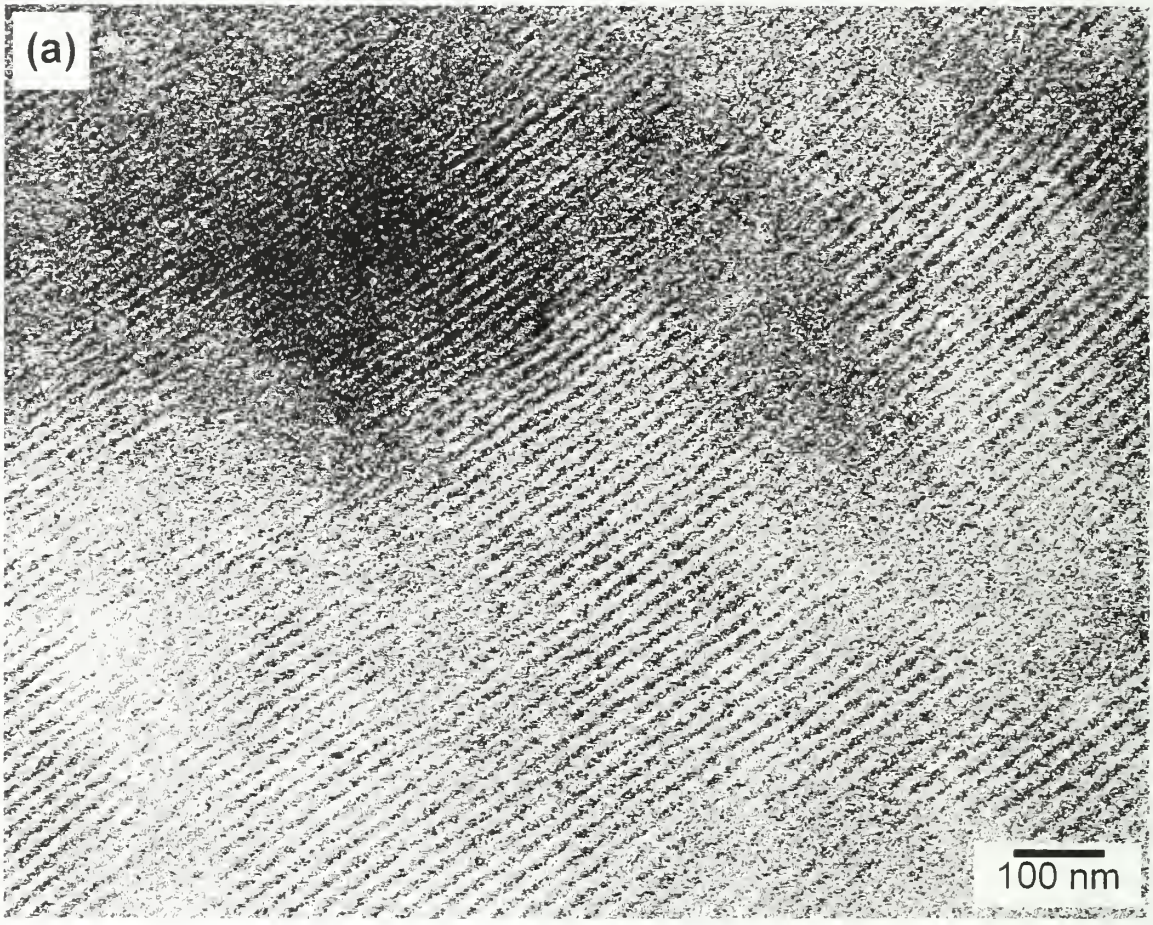

Figure 3.4 TEM micrographs showing (a) the lamellar morphology of sample A with 0.38 P*t*BVE volume fraction: (b) the lamellar morphology of sample B with 0.32 P*t*BVE volume fraction: (c) the cylindrical morphology of sample C with 0.22 P*t*BVE volume fraction. (Continued)

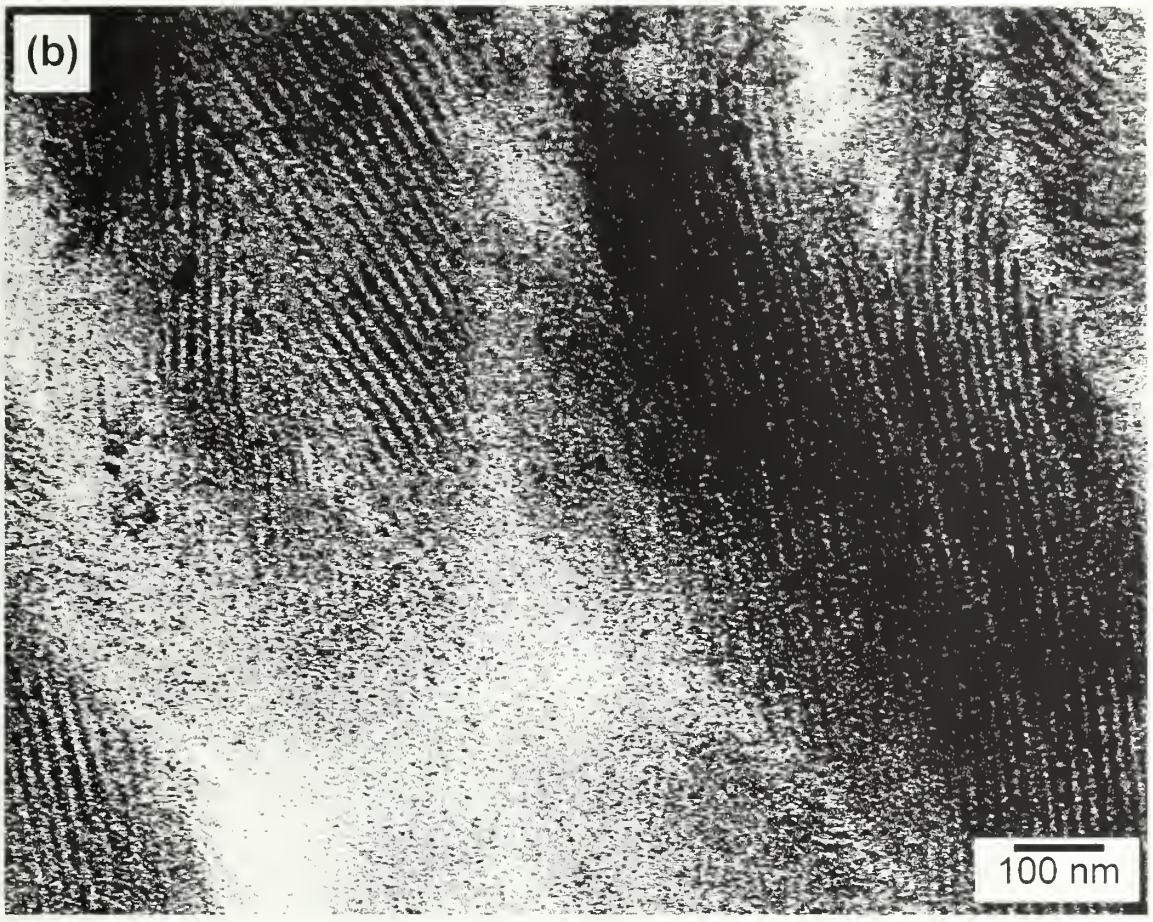

Figure 3.4 Continued.

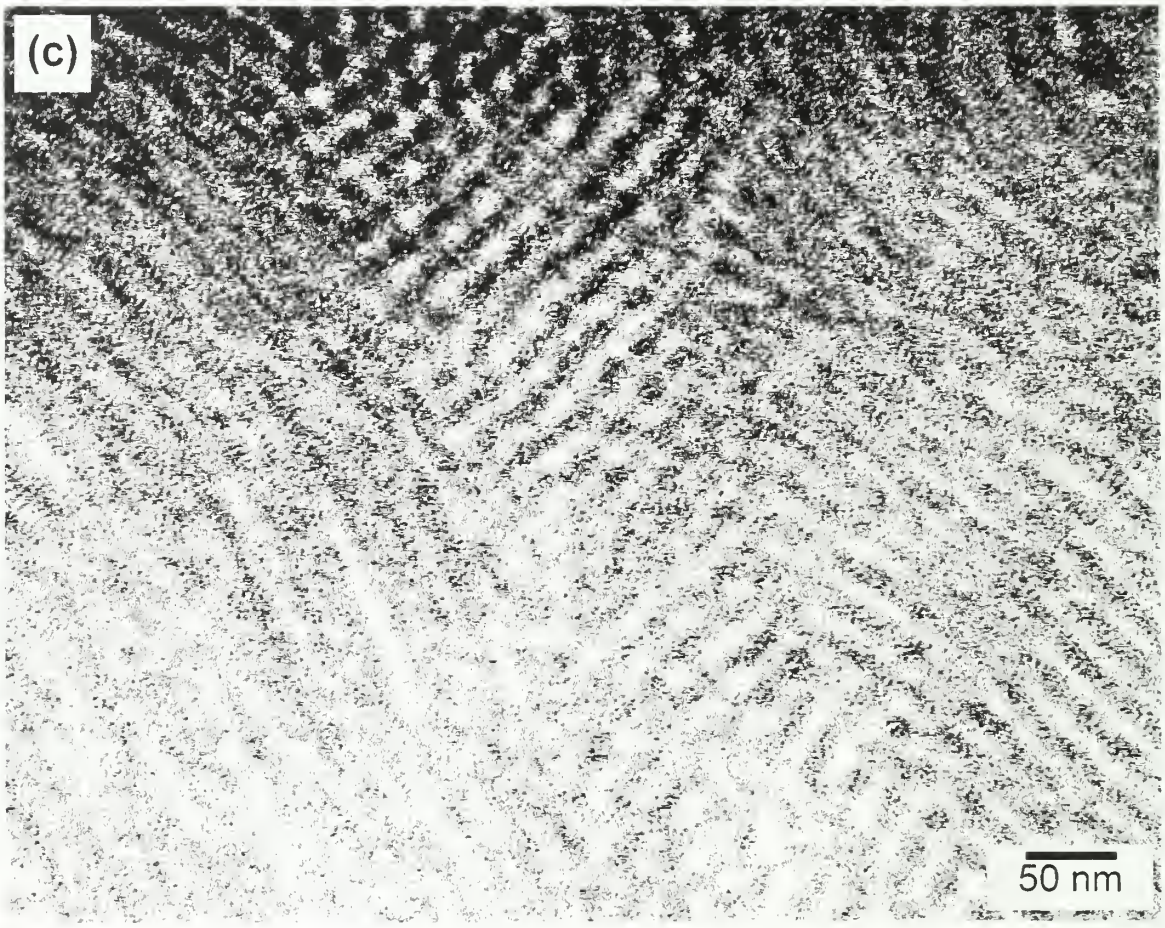

Figure 3.4 Continued.

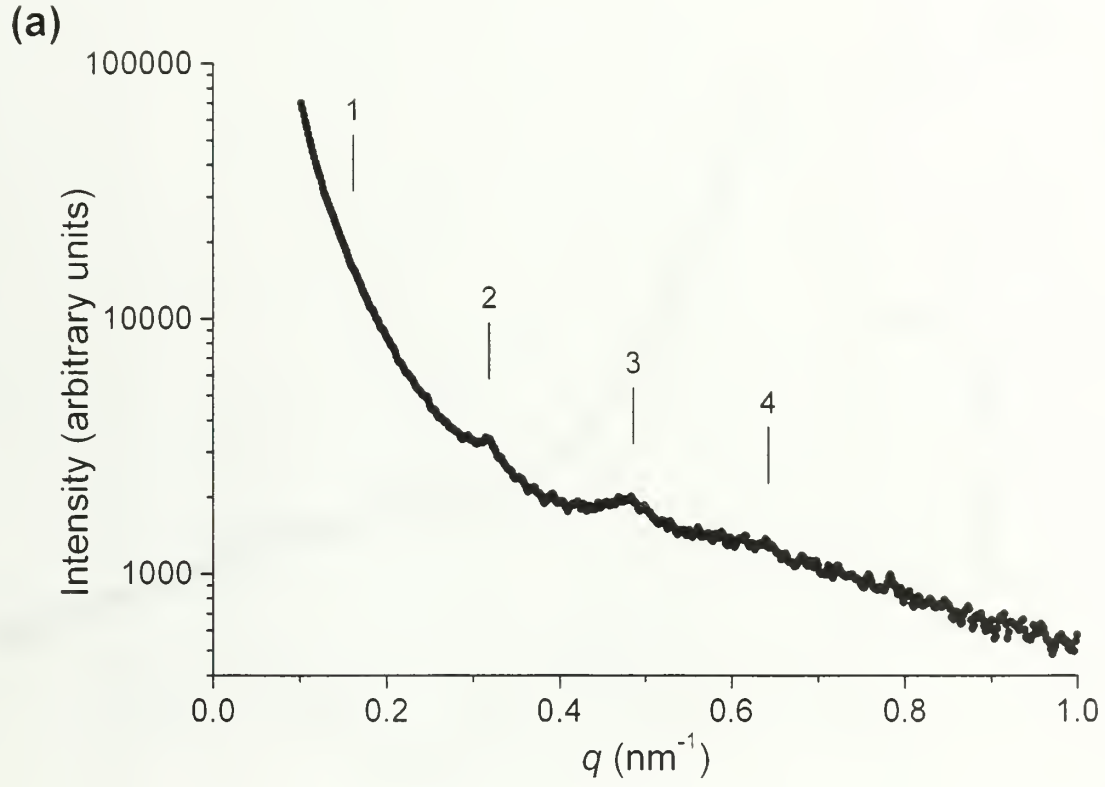

Figure 3.5 SAXS patterns of (a) sample A with 0.38 P*t*BVE volume fraction: (b) sample B with 0.32 P*t*BVE volume fraction: (c) sample C with 0.22 P*t*BVE volume fraction. (Continued)

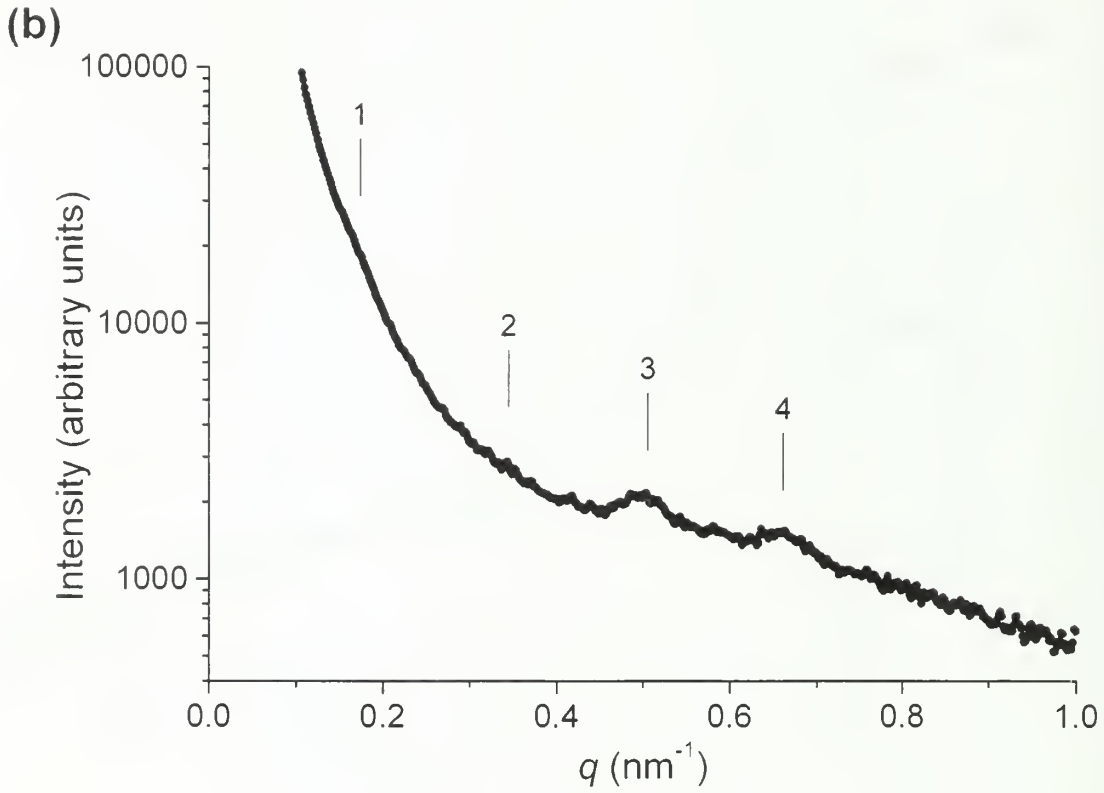

Figure 3.5 Continued.

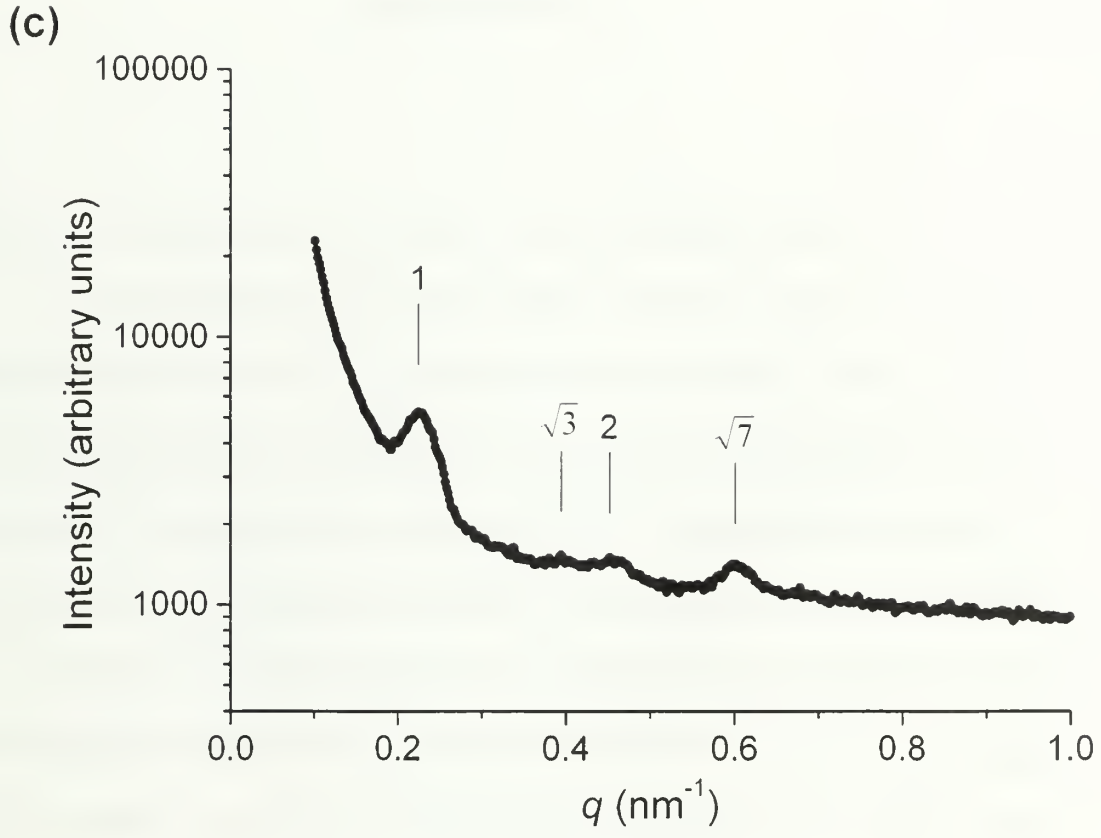

Figure 3.5 Continued.

CHAPTER 4

ORIENTED LAMELLAR STRUCTURE AND PORE FORMATION MECHANISM IN CSX-PROCESSED POROUS HIGH-DENSITY POLYETHYLENE

4.1 Abstract

Characterization of pore structure and pore wall crystal structure was performed on porous high-density polyethylene (HDPE) material using scanning electron microscopy (SEM), transmission electron microscopy (TEM), and electron diffraction (ED). The porous HDPE material was obtained through crystallization from swollen crosslinked polyethylene gels (CSX process[1]) in supercritical propane. SEM showed an open pore structure of micron-sized pores, large void fraction and surface area, as well as thin yet rigid pore walls, making this material a good candidate for a variety of applications. TEM revealed oriented lamellar structure in the pore walls which was much different from structures found in typical bulk HDPE as well as that of the crosslinked HDPE before CSX processing. Electron diffraction results confirmed the presence of oriented lamellar stacking. Based on this oriented lamellar structure, possible mechanisms for crystallization and pore formation are suggested.

4.2 Introduction

Porous polymeric materials are used in a large variety of applications, such as catalysis, separations, sound absorption, thermal and electrical insulation,[2–5] as well as biomedical applications.[6–10] Typical techniques to produce porous materials include

foaming, leaching, sintering, extrusion, injection molding, polymer precipitation, and thermally induced phase separation.[11,12] However, these processes in general do not offer optimal control over pore structure (pore size, geometry, and interconnectivity) and bulk characteristics (density, void fraction, mechanical and electrical properties). To address this issue, several new processes[1,13–15] have been developed in recent years. Shastri, Martin, and Langer[13] developed a hydrocarbon templating process for the production of macroporous polymer foams, in which a hydrocarbon particulate phase is used as a template for the precipitation of the polymer phase and subsequent pore formation. Polymer foams obtained through this method have large pores (> 100 μm) nearly identical to the particulate hydrocarbon phase employed, in terms of both geometry and size. Ko and coworkers[14] utilized electrospinning to create an interconnecting pore structure formed by electrospun poly(D,L-lactide-*co*-glycolide) (PLGA) nanofibers with diameters ranging from 500 to 800 nm. The porous PLGA material thus created has a broad pore diameter distribution, high porosity, and mechanical properties that are well suited for tissue-engineering scaffold applications. More recently, Sakai and coworkers[15] reported the fabrication of a poly(L-lactic acid) (PLLA) scaffold possessing a 3D flow channel network through repeated layering/micromachining of macroporous sheets of PLLA/NH_4HCO_3 salt particle composite followed by salt leaching and gas forming.

Among these new processes, crystallization of polymers from swollen crosslinked gels (CSX)[1] is one that offers a good combination of controllability, material properties, and environmentally-friendliness. The CSX process uses a supercritical fluid (SCF) to swell a crosslinked network of a crystallizable polymer above its melting temperature.

This is followed by cooling and crystallization of the polymer in the SCF. Venting of the SCF above the critical temperature of the fluid but below the melting temperature of the polymer leaves behind a rigid open-pore structure. The SCF can be cleaned and recycled into the CSX process, which makes it an environmentally-friendly zero-emission process. Porous materials made through CSX have open-pore structures with sterile surfaces, large specific surface areas, and controllable pore sizes and overall shapes, making them ideal candidates for biomedical applications. The fact that such low-cost thermoplastics as polyethylene and polypropylene can be easily made into well-controlled porous materials through CSX makes this process even more attractive.

Since the discovery of this novel process, attempts have been made in trying to understand the mechanism of pore formation during CSX. It was previously suggested by Nandi, Winter, and Fritz[16] that the pore structure forms in the following way: Pre-shaped and crosslinked polymers are swollen in a supercritical fluid above the crystal melting temperature of the polymer. The polymer in the swollen gel state is amorphous. Upon cooling below the crystallization temperature while maintaining pressure, fractions of the polymer crystallize in a nucleation and growth process and phase-separate from the fluid. Large composition fluctuations develop due to the crystallization process. Alternatively, some of the polymer may first separate from the fluid and then crystallize. In either case, the result is a bicontinuous morphology in which one phase is polymer rich (crystalline polymer and polymer rich amorphous phase) and the other is mostly fluid. The swelling fluid creates a continuous phase, which after its release leaves behind an open pore structure. In addition, the crosslinking was assumed to play an important role

in the phase separation process by suppressing large-scale polymer diffusion during crystallization.

Such a hypothesis paints a general picture of the pore formation process, but the detailed mechanism remains unexplained. For example, it is unknown whether the gel fraction (crosslinked segments) or the sol fraction (loose chains) nucleates first in the crystallization process. It is also unclear whether there is liquid-liquid phase separation before the onset of crystallization. We feel that a clear understanding of the polymer crystal morphology within the pore walls will help us better understand the pore formation process in CSX.

Direct observation of the pore wall morphology through transmission electron microscopy (TEM) is thus desired, since TEM together with electron diffraction should allow determination of the crystal orientation inside the pore wall if such orientation exists. However, the porous nature of the material makes it difficult to obtain suitable TEM samples. In fact, to our knowledge, no previous work has been done on the internal structural characterization of pore walls in porous crystalline polymers using direct observation techniques such as TEM, mainly due to the difficulty in obtaining suitable samples without disrupting the structure. To overcome this challenge, special care was taken in cryo-microtoming to obtain thick sections of the porous sample. It is conceivable that this technique may also be applied to TEM sample preparation of porous materials made through other processes.

The aim of this chapter is to study the pore wall crystal morphology and in turn the pore formation mechanism in the CSX process. High-density polyethylene (HDPE), the simplest and most studied crystalline polymer, is chosen as our model system. The overall pore structure of CSX-processed HDPE is characterized by scanning electron microscopy (SEM). The crystal morphology of HDPE before CSX and the pore wall morphology of HDPE after CSX are studied using TEM and electron diffraction. Based on the pore structure and the pore wall morphology, crystallization and pore formation mechanisms in the CSX process are proposed.

4.3 Experimental Section

4.3.1 Materials

The crosslinked high-density polyethylene (HDPE-10) used in this study was industrial grade HDPE in the form of solid sheets. The method of crosslinking employed was e-beam at an irradiation dose of 100 kGy.

4.3.2 Gel Fraction Measurement

The gel fraction ϕ_{gel} of the crosslinked HDPE (weight fraction of connected network with respect to the whole sample) was determined using an ASTM method.[16] A preweighed sample of mass m_0 was exposed to *p*-xylene for 72 h at 110 °C, the solvent being replenished every 24 h. This extracted most of the loose chains (sol fraction ϕ_{sol}). The gel content remained undissolved in the vessel. It was recovered and dried for 24 h

under vacuum at 80 °C before it was weighed (mass m_{sox}) to calculate the gel fraction and the sol fraction.

$$\phi_{gel} = m_{sox} / m_0; \qquad \phi_{sol} = 1 - \phi_{gel} \tag{1}$$

4.3.3 Sample Preparation

In this CSX process, the crosslinked HDPE sample of mass 1-2 g was put in a high-pressure vessel and heated to 175 °C. Propane was introduced into the system and then pressurized to 62 MPa. After a swelling time of 1.5 h, the temperature was reduced to 85 °C while maintaining the pressure, and held there for 1 h to crystallize the polymer. The temperature was raised above the critical temperature of the swelling fluid (the critical point of propane is at 96 °C and 4.2 MPa[17]), to 110 °C, before the pressure was released. After propane was completely vented, the system was cooled to room temperature and the porous sample was recovered.

4.3.4 Compressive Modulus Measurement

The compressive moduli of the crosslinked HDPE samples before and after CSX were measured in a Rheometrics RDS-LA linear rheometer. The samples were compressed at a constant strain rate of $0.005 s^{-1}$ and the resulting compressive force was measured. Strain rate $\dot{\varepsilon}$ and strain ε are defined with the sample height $H(t)$:

$$\dot{\varepsilon} = \frac{d(\ln H(t))}{dt}; \qquad \varepsilon = \ln \frac{H(t)}{H_0} \tag{2}$$

Stress was calculated by dividing the measured normal force by the cross-sectional area of the sample. The compressive modulus E is defined as the slope of the best linear fit of the stress-strain curve. The molecular weight of strands between crosslinks M_C was estimated from E:

$$M_c = \frac{3RT\rho\phi_{gel}}{E} \tag{3}$$

where R is the universal gas constant, T is the experimental temperature in absolute scale, and ρ is the density of the polymer.

4.3.5 Differential Scanning Calorimetry (DSC)

The melting behavior of HDPE-10 before and after CSX was studied by differential scanning calorimetry (DSC) using a TA Instruments Q1000 DSC. The instrument was calibrated using indium as standard. Melting endotherms were obtained at a heating rate of 10 °C/min using 5 mg of sample. The degrees of crystallinity were calculated from the heat of fusion using 293 J/g as the heat of fusion of 100% crystalline polyethylene.[18]

4.3.6 Scanning Electron Microscopy (SEM)

The pore structure of the porous HDPE-10 sample after CSX was viewed under a JEOL 6320F field emission gun scanning electron microscope (FEGSEM). To expose the internal pore morphology, the porous sample was freeze fractured in liquid nitrogen. The cracked sample was then placed on a support disc, and the fracture surface was coated with a thin layer of platinum using a Gatan 681 high resolution ion beam coater, at a deposition rate of 1 nm/min for 4 min. The platinum coating thus obtained was about 4

nm thick, which not only effectively covered the massive surface area in the porous sample to prevent charging in the SEM, but also made high-resolution imaging possible due to its fine granular structure.

4.3.7 Transmission Electron Microscopy (TEM) and Electron Diffraction (ED)

The microstructure of HDPE-10 before and after CSX was analyzed by transmission electron microscopy (TEM) using a JEOL 2000 FX TEM at 200 kV accelerating voltage. For the crosslinked HDPE sample before CSX, ultrathin sections of about 50 nm in thickness were cut using a Leica Ultracut cryomicrotome and a Diatome diamond knife at a knife/sample temperature of -150 °C. The sections were collected on copper grids and stained in the vapors of ruthenium tetraoxide (RuO_4) for 1 h before being examined in TEM. For the porous CSX processed HDPE, it would be too difficult to obtain ultrathin TEM sections using microtomy. The high sample porosity would cause thin sections to fall apart. Instead, the porous sample was microtomed at a thickness of 500 nm, using the same temperature setting as that for the sample before CSX (-150 °C). The sections were then stained in RuO_4 vapors for 1 h before TEM examination. An illustration of this technique is shown in Figure 4.1. Although the majority of the sectioned material should be overlapped randomly-oriented interconnected pore walls (depicted as thick blocks in Figure 4.1) that would be too thick for TEM observation, it was expected that within the thick sections occasionally there should be see-through areas (the middle region in Figure 4.1) where single layer of the pore wall lies approximately parallel to the section surface, thus providing a direct view of the pore wall crystal morphology in the TEM. Because only the upper and lower

surfaces of the thick section were ever touched by the diamond knife during the microtoming process, the single pore wall layer observed in the TEM was effectively embedded inside the thick section due to the interconnectivity of the pore walls and therefore protected from any possible external deformation. Thus the TEM morphology obtained for the single pore wall layer should reflect the true morphology of the pore walls in the porous CSX-processed HDPE material.

In performing electron diffraction (ED) and TEM care was taken to limit unnecessary electron beam exposure thus minimizing electron beam damage and producing the best possible electron diffraction patterns. This included such standard procedures as focusing on an adjacent area to the area where data was recorded, using the smallest possible spot size, limiting the spread of the beam, and turning the beam off when it was not needed. Also the ED data was recorded on fast X-ray film (Kodak DEF5) rather than standard EM film. In order to calibrate the diffraction camera length, some sample grids were sputter coated with gold and the Au (111) ring was used as an internal standard.

4.4 Results and Discussion

4.4.1 Mechanical and Thermal Properties

Table 1 lists the gel fraction ϕ_{gel}, the compressive modulus E, and the molecular weight between crosslinks M_c, of HDPE-10, as well as the crystallinity and the melting temperature T_m of the polymer before and after CSX. Both the gel fraction and the molecular weight between crosslinks are indicators of the degree of crosslinking in a

polymer sample. A higher degree of crosslinking is expressed by higher gel fraction and lower molecular weight between crosslinks. A previous study on CSX-processed low-density polypropylene[16] has found that the degree of crosslinking has a strong effect on pore size, with higher gel fraction and lower molecular weight between crosslinks resulting in smaller pore size, although a quantitative relationship between the degree of crosslinking and pore size is not yet established. As shown in Table 4.1, the HDPE-10 sample used in this study has a moderate gel fraction of 41% and a molecular weight between crosslinks of 7300 g/mol, indicating a moderate degree of crosslinking. The measured value of the average pore size in CSX-processed HDPE-10 will be presented in the next section. The compressive modulus of HDPE-10 after CSX, 5.1 MPa, is almost an order of magnitude smaller than that of HDPE-10 before CSX, 46 MPa. This decrease in compressive modulus is not unexpected given the porous nature of the sample after CSX, however 5.1 MPa is a relatively high compressive modulus for a porous polymeric material.

DSC melting endotherms of HDPE-10 before and after CSX are shown in Figure 4.2. The crystallinity of HDPE-10 increased from 62% to 69% after CSX, possibly due to the presence of the supercritical fluid which increases the mobility of the polymer chains and results in the crystallization of less perfect chains. On the other hand, the melting temperature decreased slightly from 132°C to 127°C and the melting peak became narrower after CSX, indicating thinner lamellae and better defined lamellar thickness in the porous HDPE-10. The inclusion of less perfect chains in the crystal

lattice may also contribute to the decease of the melting temperature in the CSX-processed HDPE.

4.4.2 Pore Structure and Pore Size

Two typical SEM micrographs of HDPE-10 after CSX are shown in Figure 4.3, in which Figure 4.3a shows an overall pore structure at lower magnification and Figure 4.3b shows a more localized view at higher magnification. An open pore structure with large surface area can be seen in both micrographs. A rough measurement[16] of the pore sizes from more than 20 SEM images gave an average pore size of 1-2 μm, for the porous HDPE-10 after CSX. High-resolution SEM images such as Figure 4.3b reveal that smaller pores on the order of tens of nanometers are sometimes present on the pore walls. The pore walls themselves are quite thin and are on the order of 100 nm or thinner, as measured from the SEM images. Despite the thin walls, the pore structure is quite rigid, as demonstrated by the relatively high compressive modulus. The fact that the pore structure has survived both the fluid venting process and the cryo-fracturing process reaffirms the rigidity of the pore structure in the porous HDPE-10. The rigidity may come from (1) the presence of a continuous polymer phase and (2) the polyethylene crystallites within the pore walls.

4.4.3 Morphology of HDPE before CSX

In order to assess the degree to which the CSX process has changed the morphology of the crosslinked HDPE, TEM was performed on the HDPE-10 sample before CSX. Shown in Figure 4.4a is a typical TEM micrograph of the HDPE-10

morphology before CSX. The amorphous phase appears dark and the crystalline phase appears light in the TEM micrograph due to RuO_4 staining. Since the HDPE-10 sample was melt-extruded first and then e-beam crosslinked in the form of extruded sheets, its morphology is that of typical melt-crystallized polyethylene. Lamellae parallel to the plane of view, perpendicular to the plane of view, as well as those of intermediate orientations, are all clearly seen. A wide-angle x-ray diffraction pattern and an electron diffraction pattern of this sample are shown in Figures 4.4b and 4.4c, respectively. The two characteristic rings in both figures correspond to the *110* and *200* diffraction signals of the orthorhombic polyethylene crystal lattice. The polycrystalline rings obtained in both diffraction patterns further confirm the lack of orientational order in the crosslinked HDPE before CSX.

4.4.4 Morphology of HDPE after CSX

As mentioned in the experimental section, the porous HDPE sample after CSX were cryo-microtomed into 500-nm thick sections inside of which thin areas of single pore wall were targeted for TEM examination. Figure 4.5a shows a representative TEM micrograph of such a see-through area in the porous HDPE-10 after CSX. In this figure, the overall morphology is that of a piece of pore wall (the middle region of the micrograph) lying almost parallel to the section surface and spanning across two thicker regions of overlapped pore walls (the upper-left and lower-right corners), which appear dark in the TEM. The geometry of this sampled area matches very well with the illustration in Figure 4.1. As characterized by SEM, individual pore wall thickness is on the order of 100 nm or less. This allows the electron beam to readily pass through the

pore wall and reveal its internal structure in the TEM. Conversely, the fact that TEM imaging was successful on isolated pore walls also supports our claim about the thinness of the pore wall.

In Figure 4.5a, the lower part of the viewable area is mostly composed of one single layer of pore wall, while the upper part is composed of two or more pore wall layers, all of which lie more or less parallel to the section surface. Despite the number of layers, two features of the pore wall are clearly visible: 1) The pore walls are indeed interconnected; 2) In addition to the large micron-sized pores, nanopores on the order of 100 nm or smaller are sometimes formed on the pore walls. Both features are also seen in the SEM micrographs (Figure 4.3).

By focusing on the boxed area (single pore wall layer) in Figure 4.5a at higher magnification, the TEM micrograph in Figure 4.5b was obtained, which reveals more detail of the crystal morphology of the pore wall. Clearly the crystal morphology in Figure 4.5b is very different from that of Figure 4.4a. There are several important features about this morphology. First, the lamellar crystals (light phase in the TEM micrograph) are oriented perpendicular, not parallel to the plane of the pore wall surface. Second, the crystalline lamellae and the amorphous layers (dark phase in the TEM micrograph) stack on top of each other to form oriented lamellar stacks. Third, the lamellar crystals appear to be preferentially aligned perpendicular to the edges of the pore wall.

To explain this morphology, we propose a lamellar stacking model as shown in Figure 4.6. In this model, the crystalline lamellae are indicated by the light phase composed of folded chain stems and the amorphous layers are drawn as dark regions in between the lamellae. The crystalline lamellae and amorphous layers alternate and stack along the chain axis (c-axis) of polyethylene, which is proposed to be parallel to the lamellar normal. As a starting point, it is assumed that the stacked lamellar crystals have random orientation around the chain axis, as in polyethylene fibers.

Selected area electron diffraction was performed on the microtomed pore wall sections, using a 20 μm selected area aperture. This technique allows the isolation of diffraction signal from a single pore wall and thus allows evaluation of crystallite orientation within the pore wall. A representative electron diffraction pattern is shown in Figure 4.7, in which two pairs of arcs corresponding to *110* and *200* diffraction signals of polyethylene are seen. The observation of arcs instead of rings further indicates the oriented lamellar morphology in the pore wall. The diffraction arcs are oriented parallel to the crystalline lamellar surface, which indicates that the polyethylene chain axis (c-axis) is perpendicular to the lamellar surface, or parallel to the lamellar normal, as our model suggests. The observation of *110* and *200* arcs at the same time also indicates that there is a uniaxial or fiber-like orientation of the lamellae about the c-axis.

4.4.5 Origin of Lamellar Stacking and Pore Formation Mechanism in the CSX Process

The electron diffraction pattern seen in Figure 4.7 is quite similar to diffraction patterns of drawn polyethylene fibers. Such diffraction patterns are also observed for

polyethylene crystallized in a highly stressed state. Shish-kebabs from elongational flow-induced solution crystallization[19] and row-nucleated structures from stress-induced melt crystallization[20] both give similar diffraction patterns. In both cases, the chain axis (c-axis) is oriented in the flow (or stress) direction and the chain-folded lamellae (kebabs in shish-kebabs and rows in row structures) are preferentially oriented perpendicular to the flow (or stress) direction, or in the ab plane of polyethylene crystal lattice. These characteristics match well with the lamellar stacking morphology observed in the pore walls of HDPE after CSX.

We have previously argued that crystallization in the CSX process is quite similar to crystallization from solution, the difference being the use of a supercritical fluid as solvent, which entails higher chain mobility. However, it is still unclear as to whether phase separation occurs due to crystallization or the gel first phase separates and then the polymer crystallizes. A phase diagram of HDPE in supercritical propane (Figure 4.8), similar to the one obtained for polypropylene,[21] can be assumed. Thus, during the CSX process, when the temperature is reduced, HDPE and the supercritical propane should phase separate as the temperature approaches the two-phase region, shown in Figure 4.8. However, crystallization of the polymer might occur at a temperature above the phase-separation temperature. In such a situation, crystallization induces phase separation. Also, it is possible that the crystallization temperature of HDPE in supercritical propane is below the phase-separation temperature. In such a situation, the polymer and the swelling fluid phase separate into polymer rich and propane rich regions before the polymer starts to crystallize. Since it is very difficult to isolate the crystallization

temperature of HDPE in supercritical propane from the phase-separation temperature, we propose possible mechanisms of crystallization and pore formation for both cases.

4.4.5.1 Crystallization Prior to Phase Separation

Due to the presence of chemical crosslinks, in the highly swollen state (500 – 800% by volume), although the overall stress in the polymer network is isotropic, locally the network segments can experience high-degree of stress in a specific direction. These locally oriented stretched segments have a higher crystallization temperature due to their extended-chain conformation and nucleate first as the temperature lowers in the cooling process. They nucleate as oriented fibrils along the local stretching direction upon which chain-folded lamellar crystals grow when the temperature is further lowered to their crystallization temperature. Therefore, it is likely that some of the crosslinked segments (the gel fraction) which experience highest degree of stretching crystallize first in a chain-extended fashion and the loose chains (the sol fraction) mainly participate in subsequent lamellae crystallization transverse to those extended crystals. The rest of the network segments either crystallize in the oriented lamellae or remain non-crystalline in the amorphous regions in between the lamellar crystals. The overall result of such crystallization would be locally oriented stacked lamellae as seen in the TEM micrographs (Figure 4.5).

Many such nucleating chain segments are created adjacent to each other at the onset of crystallization. The secondary growth (oriented lamellae) begins on each of these locally aligned nuclei. Large density fluctuations occur during this process. As

chain folding and the formation of the lamellae continue, polymer chains migrate towards those nuclei creating polymer rich and polymer lean regions. The growth continues until the lamellae impinge. The series of impinged oriented lamellar stacks positioned next to each other create a sheet of crystalline polymer. This forms the basis of the pore wall while the polymer lean regions created during the formation of the lamellae become the pores. The pore size formed during the process is dictated by the distance between the adjacent nuclei, which in turn is determined by the crosslink density of the polymer.

During the fast growth of the lamellar crystals, the growth rate might overtake the rate of diffusion of the polymer chains. The lack of availability of the polymer creates defects in the lamellar structure, which translate into nanopores that are observed in the pore walls.

4.4.5.2 Phase Separation Followed by Crystallization

In this possible alternative scenario, as the temperature is reduced, the solvation power of supercritical propane decreases leading to micro-phase separation. A thin interconnected continuous polymer rich phase is formed which coexists with the continuous propane rich phase. The connectivity of the polymer phase is maintained due to the presence of the crosslinks, which give the structure a length scale and prevent coarsening as would be seen in classical spinodal decomposition. Thus the crosslink density determines the size of the solvent pockets formed in between the polymer phase.

As the phase separation occurs on a microscopic scale, the molecular strands between the crosslinks in the polymer network experience large amounts of strain. This strain, caused by biaxially drawing the polymer rich microdomains into the cell walls that divide the pores, adds to the strain caused by initial swelling in the supercritical propane and results in local orientation of polymer chains. These elongated chains crystallize first and act as nucleating agents upon which the chain-folded lamellae grow transversely. Due to the 2-dimentional confinement of the crystal growth within the thin polymer phases making up the developing cell wall, the oriented lamellar growth is preferred in the plane of the pore wall, leading to the formation of high aspect-ratio ribbon-like lamellar crystals.

It is interesting to compare results of this study to solution crystallization from supercritical solvents. Before the development of the CSX process, there have been solution crystallization studies of uncrosslinked high-density polyethylene (Winter and coworkers, unpublished) and isotactic polypropylene (Whaley et al.[22,23]), where the solvent was supercritical propane, as in this study. For both polymers, the resulting morphology differs greatly from that obtained from crosslinked polymers using CSX. Without pre-crosslinking, the porous polymer structure grown from supercritical propane has low molecular interconnectivity and relatively poor mechanical strength, suggesting that in such systems the phase separation is induced by the crystal formation. In these experiments, no polymer-rich regions were created by phase separation prior to the onset of crystallization; during crystal growth molecular chains could diffuse freely toward the growing crystal (spherulite). As a consequence, depletion regions are generated

throughout the solution, resulting in semicrystalline spherulites that are poorly interconnected.

In the case of the CSX process, the polymers are pre-crosslinked. The crosslinks hold the polymer together during the crystallization process. Prior phase separation is no longer necessary to create an interconnected polymer network in the CSX-processed porous polymer. Therefore the first mechanism, crystallization prior to phase separation, is a likely mechanism based on results from uncrosslinked polymers. On the other hand, the crosslinking may have an effect on lowering the crystallization temperature of the polymer to below its phase-separation temperature in the supercritical fluid. If this is the case, then the second mechanism, phase separation followed by crystallization, will be a likely mechanism.

Based on the current data, we cannot at this time distinguish between these two possible crystallization and pore formation mechanisms. However, independent of the pore formation mechanism, we can affirm that there is no preferential direction for the lamellar stack orientation, because the origin of the initial alignment of the chains is swelling, which is isotropic in macroscopic scale. Therefore, adjacent lamellar stacks may have different orientations, as observed in the TEM micrographs (Figure 4.5). However, the nucleating chain segments that form the backbone of the stacked lamellar structure are covalently connected because of the crosslinking. This interconnectivity of the crystalline structure provides structural integrity and significant mechanical strength to the pore walls which is extremely desirable for many applications.

4.5 Conclusions

Porous HDPE material was obtained through crystallization from swollen crosslinked polyethylene gels (CSX process[1]) in supercritical propane. SEM showed a micron-sized open pore structure, large void fraction and surface area, as well as thin yet mechanically sustainable pore walls in the porous HDPE material. TEM revealed oriented lamellar structure in the pore walls, with ribbon-like lamellar crystals, much different from structures found in typical bulk HDPE material as well as that of the crosslinked HDPE before CSX processing. Electron diffraction determined the chain axis orientation as well as the random rotation of lamellar crystals in the lamellar stacks. Based on this oriented lamellar structure, two plausible scenarios for crystallization and pore formation in the CSX process are suggested, one favoring crystallization prior to phase separation and the other favoring phase separation prior to crystallization. It would be difficult to prove one or the other due to the possible depression of polyethylene crystallization temperature in supercritical propane.

4.6 References

(1) Winter, H. H.; Gappert, G.; Ito, H. *Macromolecules* **2002**, *35*, 3325–3327.

(2) Pinnau, I. In *Encyclopedia of Separation Science*; Wilson, I. D., Ed.; Academic Press: San Diego, 2000; Vol. 4, pp 1755–1764.

(3) Mark, H. F.; Bikales, N. M.; Overberger, C. G.; Menges, G. In *Encyclopedia of Polymer Science and Engineering*; Mark, H. F., Ed.; John Wiley & Sons: New York, 1990; Vol. 9, p 509.

(4) Paul, D.; Peinemann, K.-V. In *Polymeric Materials Encyclopedia*; Salamone, J. C., Ed.; CRC Press: Boca Raton, FL, 1996; Vol. 6, pp 4074–4082.

(5) Chiang, C.-Y.; Lloyd, D. R. *J. Porous Mater.* **1996**, *2*, 273–285.

(6) Suh, J.-K. F.; Matthew, H. W. T. *Biomaterials* **2000**, *21*, 2589–2598.

(7) Glicklis, R.; Shapiro, L.; Agbaria, R.; Merchuk, J. C.; Cohen, S. *Biotechnol. Bioeng.* **2000**, *67*, 344–353.

(8) Ma, T.; Li, Y.; Yang, S.-T.; Kniss, D. A. *Biotechnol. Bioeng.* **2000**, *70*, 606–618.

(9) Ma, P. X.; Choi, J.-W. *Tissue Eng.* **2001**, *7*, 23–33.

(10) Stachowiak, A. N.; Bershteyn, A.; Tzatzalos, E.; Irvine, D. J. *Advanced Materials* **2005**, *17*, 399–403.

(11) Gibson, L. J.; Ashby, M. F. *Cellular Solids: Structure and Properties*; Cambridge University Press: New York, 1997.

(12) Saunders, J.; Hansen, R. In *Plastic Foams*; Frisch, K., Saunders, J., Eds.; Dekker: New York, 1972; Part I, pp 23–108.

(13) Shastri, V. P.; Martin, I.; Langer, R. *Proc. Natl. Acad. Sci. USA* **2000**, *97*, 1970–1975.

(14) Li, W.-J.; Laurencin, C. T.; Caterson, E. J.; Tuan, R. S.; Ko, F. K. *J. Biomed. Mater. Res.* **2002**, *60*, 613–621.

(15) Sakai, Y.; Otsuka, M.; Hanada, S.; Nishiyama, Y.; Konishi, Y.; Yamashita, A. *Mat. Sci. Eng. C* **2004**, *24*, 379–386.

(16) Nandi, S.; Winter, H. H.; Fritz, H. G. *Polymer* **2004**, *45*, 4819–4827.

(17) Tester, J. W.; Modell, M. *Thermodynamics and Its Applications*, 3rd ed.; Prentice Hall PTR: New Jersey, 1983, Appendix G.

(18) Wunderlich, B. *Macromolecular Physics, Vol. 3: Crystal Melting*; Academic Press: New York, 1980.

(19) Pennings, A. J.; Kiel, A. M. *Kolloid-Z.* **1965**, *205*, 160–162.

(20) Keller, A.; Machin, M. J. *J. Macromol. Sci. Phys.* **1967**, *B1*, 41–91.

(21) Whaley, P. D.; Winter, H. H.; Ehrlich, P. *Macromolecules* **1997**, *30*, 4887–4890.

(22) Whaley, P. D.; Kulkarni, S.; Winter, H. H.; Stein, R. S; Ehrlich, P. *Polym. Mat. Sci. Eng.* **1995**, *73*, 404–405.

(23) Whaley, P. D.; Kulkarni, S.; Ehrlich, P.; Stein, R. S.; Winter, H. H.; Conner, W. C.; Beaucage, G. *J. Polym. Sci. Pol. Phys.* **1998**, *36*, 617–627.

Table 4.1 Gel Fraction, Compressive Modulus, Molecular Weight between Crosslinks, Crystallinity, and Melting Temperatures of HDPE-10 before and after CSX

Sample	Gel Fraction (%)	Compressive Modulus (MPa)	M_c (g/mol)	Crystallinity (%)	T_m (°C)
HDPE-10 before CSX	41	46	7300	62	132
HDPE-10 after CSX	-	5.1	-	69	127

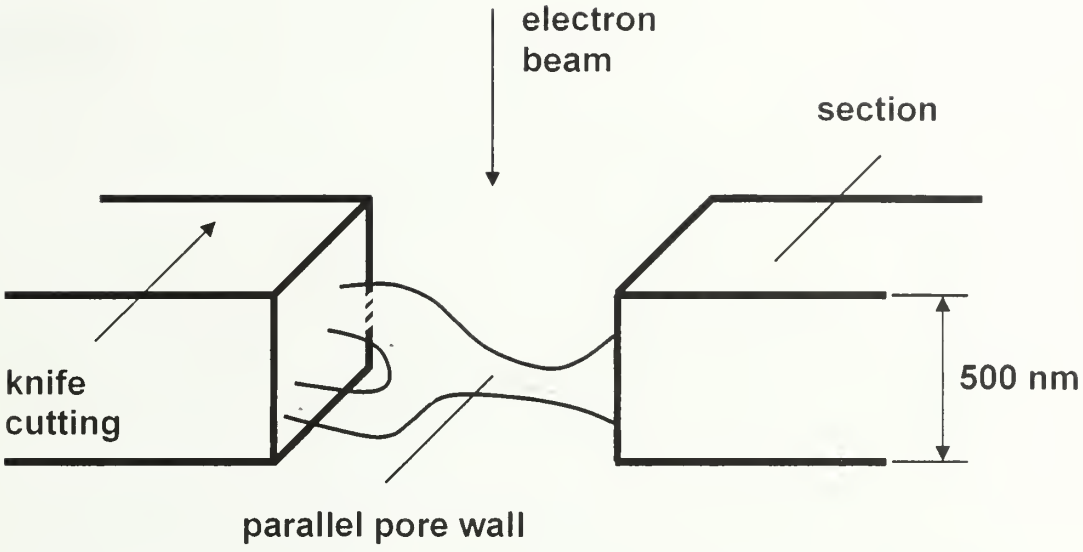

Figure 4.1 Illustration of a microtomed thick section of the porous HDPE-10 after CSX with an embedded single pore wall layer for TEM observation.

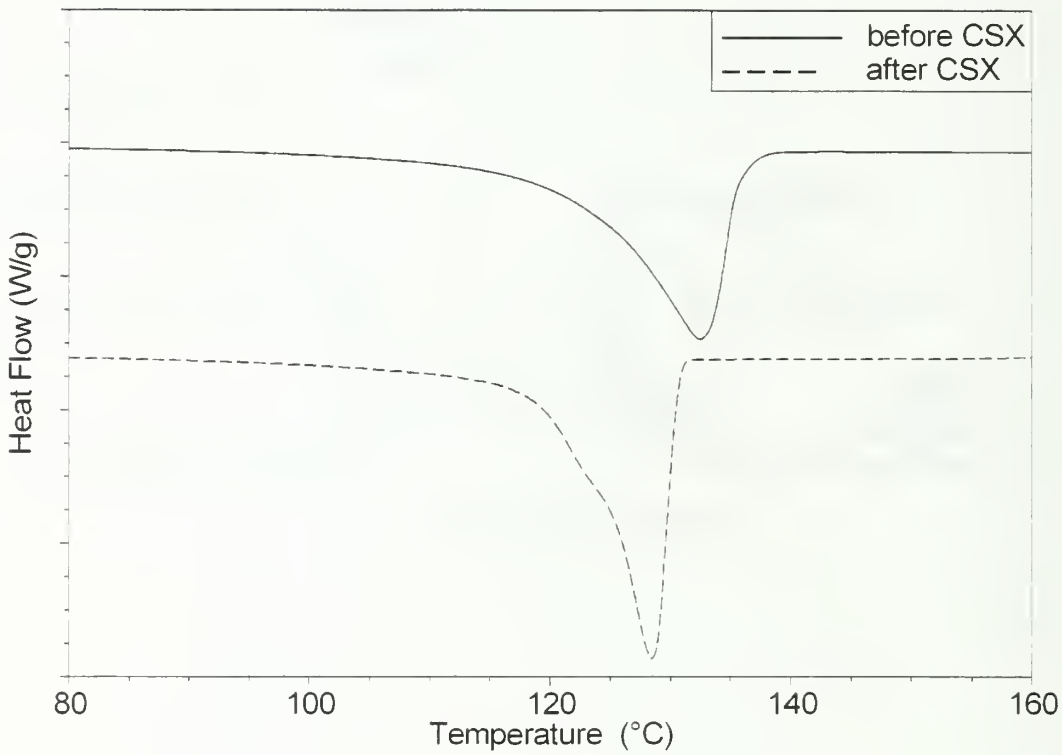

Figure 4.2 DSC melting endotherms for HDPE-10 before and after CSX.

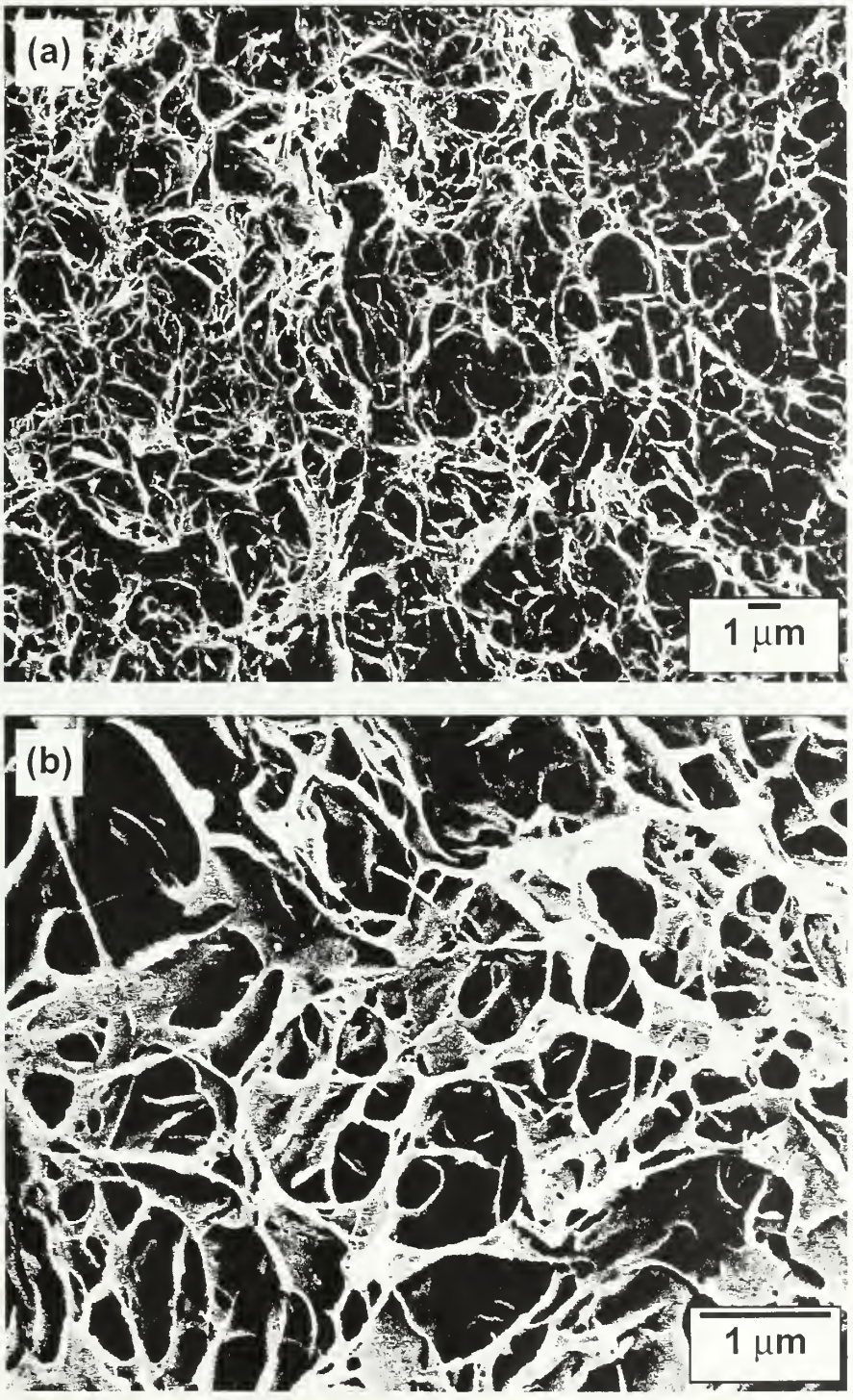

Figure 4.3 Pore structure of porous HDPE-10 after CSX. (a) Low-magnification SEM micrograph; (b) High-magnification SEM micrograph.

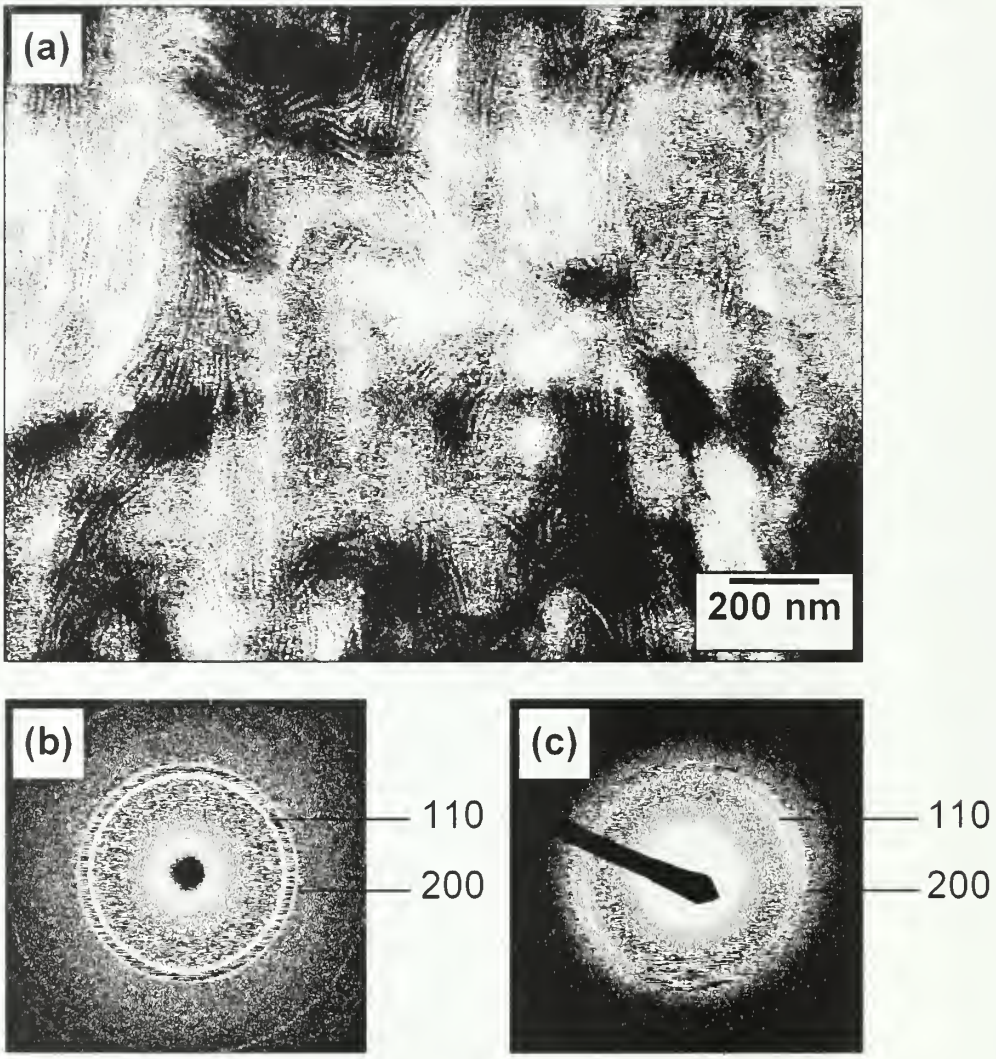

Figure 4.4 Bulk morphology of HDPE-10 before CSX. (a) TEM micrograph: (b) Wide angle x-ray diffraction pattern: (c) Selected area electron diffraction pattern.

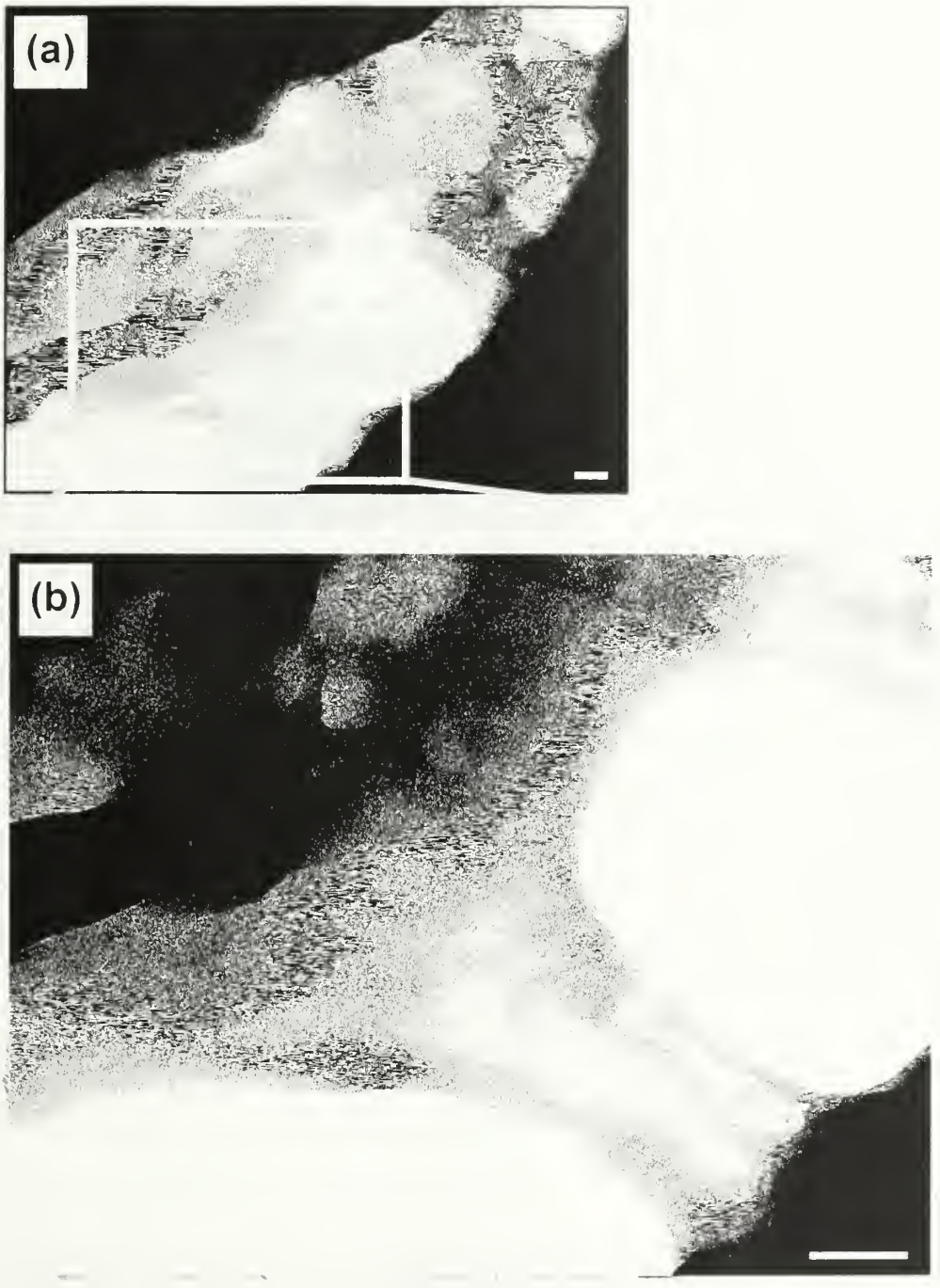

Figure 4.5 TEM micrographs showing pore wall morphology of porous HDPE-10 after CSX. (a) Low-magnification overview of a pore wall segment spanning across two thicker overlapped regions: (b) High-magnification TEM micrograph of the boxed area in (a). Scale bar: 100 nm.

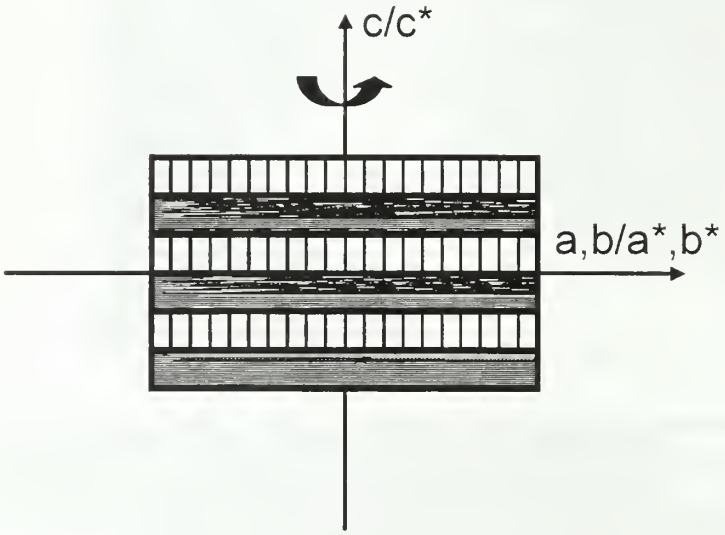

Figure 4.6 Proposed lamellar stacking model for the pore wall structure of porous HDPE-10 after CSX. In this model, a, b, c represent the crystallographic axes of the orthorhombic unit cell of polyethylene, of which c is the chain axis; a*, b*, c* represent the corresponding axes of polyethylene reciprocal lattice, with relationships a // a*, b // b*, and c // c*.

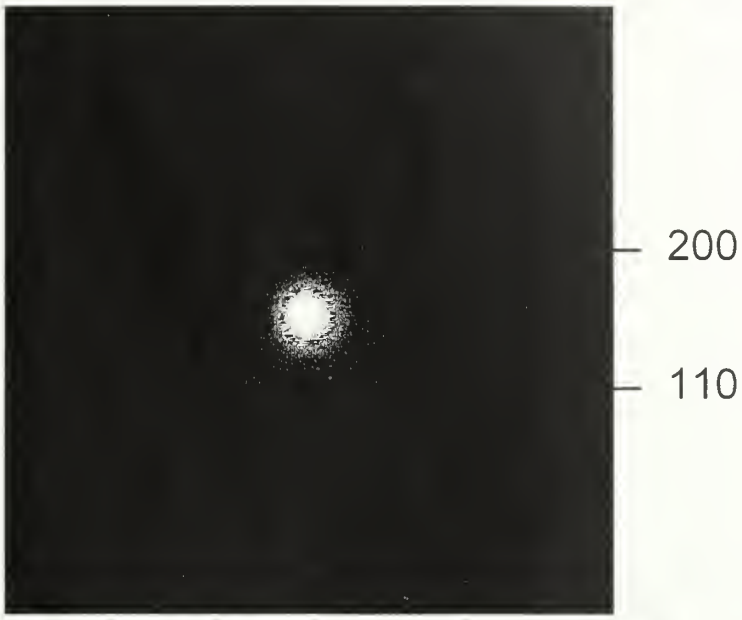

Figure 4.7 Selected area electron diffraction pattern from a single layer pore wall in a microtomed thick section of porous HDPE-10 after CSX.

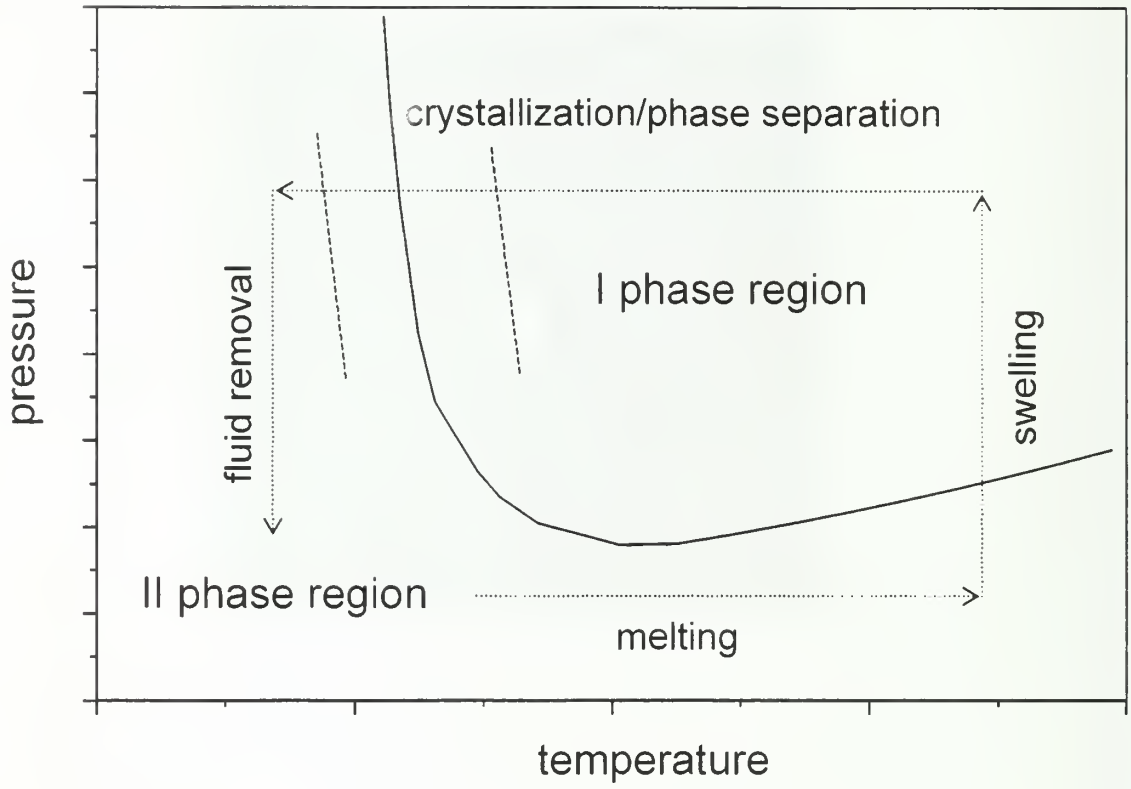

Figure 4.8 Phase behavior of HDPE as expected in supercritical propane. The solid line represents the temperature and pressure conditions for the phase separation of the polymer and propane. The dotted line represents the CSX process. The dashed lines represent the crystallization temperature of HDPE in the presence of supercritical propane. It is difficult to determine whether crystallization occurs prior to or after phase separation.

CHAPTER 5

OTHER POLYMER SYSTEMS STUDIED

5.1 SEBS Triblock Copolymers Cast from Selective Solvents

5.1.1 Introduction

It is well-known that the morphologies of block copolymers are dependent on the solvents from which they are cast.[1] The selectivity of the solvent affects the effective volume fractions of different blocks, and therefore the resultant morphology. For example, the morphology of a lamellar AB diblock copolymer may become that of A cylinders when cast from a B-selective solvent, and that of A spheres if the solvent selectivity for B is even higher.

Usually equilibrium morphologies are desirable and neutral or non-preferential solvents are used. In practice, however, it is often hard to find a true neutral solvent for a two-phase system, let alone a system with three or more components. Even if such a neutral solvent does exist, its use may not be preferred due to environmental or economical concerns. Therefore, the use of a selective solvent may be inevitable in certain applications.

In many cases, the initial non-equilibrium morphology obtained from a selective solvent may be converted to the equilibrium morphology via thermal annealing. One can imagine that, depending on the degree of selectivity of the initial casting solvent, and in turn the nature of the initial morphology, the degree of order as well as lattice dimensions

in the final morphology may vary. Such a selective-solvent effect may be a positive or negative one, that is, the resultant final morphology may have better or worse order as compared to the one from a neutral (or almost neutral) solvent. If it turns out to be a positive one, it will become a new means to improve long-range order in block copolymer morphologies.

It is therefore meaningful to study systematically the effect of solvent selectivity on the final block copolymer morphology, in terms of both the degree of order and the lattice dimensions, and assess the feasibility of using selective solvents as a possible means of morphological control in block copolymer systems.

5.1.2 Experimental Methods

The SEBS triblock copolymer was obtained from Kraton Polymers . The characteristics of both block copolymers are given in Table 5.1. SEBS was solution cast from selected solvents at room temperature for 3 to 7 days. Specifically, toluene (S-selective), cyclohexane (neutral for S and EB), and hexane (EB-selective), are used. All as-cast SEBS samples were further vacuum annealed at 120 °C for one week, followed by 140 °C for one week, and then 160 °C for one more week.

Ultrathin sections of the samples were obtained through cryo-microtoming, at a knife temperature of -120 °C. The sections were then stained in RuO_4 vapors for 1 h before TEM observation. SAXS was performed on as-cast and annealed films using Cu Kα X-ray radiation and pinhole collimation. Patterns were collected digitally with a 2D

multiwire detector and analyzed with a multichannel analyzer and custom-written software.

5.1.3 Results and Discussion

The as-cast morphologies of all three SEBS samples (cast from toluene, cyclohexane, and hexane), as well as the final morphologies of all samples after three weeks of thermal annealing, are shown in Figure 5.1. The respective SAXS profiles are shown in Figure 5.2. The TEM morphologies and lattice dimensions as measured from SAXS are summarized in Table 4.2.

SEBS used in this study has a styrene volume fraction of 0.26. According to the theoretical morphological diagram, the equilibrium morphology should be that of styrene cylinders in an ethylene/butylene matrix. When cast from toluene, a styrene-selective solvent, it was not surprising that SEBS adopts a lamellar morphology, since toluene would swell the styrene phase and increase its effective volume fraction to push it over the cylindrical/lamellar boundary. However, the formation of a mixture of lamellae and modified layers (an intermediate phase between lamellae and cylinders) when cast from cyclohexane, was somewhat unexpected. This may be due to the fact cyclohexane, although a near-neutral solvent based on solubility parameter data, is not a true neutral solvent. It may have slight preference for styrene. Another possibility is that the system studied may be too close to a phase boundary and any slight perturbation in solvent quality may have a large impact on morphology. SEBS cast from hexane adopts a spherical morphology, because the solvent is strongly selective for ethylene/butylene and too poor for styrene.

After extensive thermal annealing, the morphology of samples cast from all three solvents changed into that of core-shell cylindrical with styrene as the shell and ethylene/butylene as both the core and the matrix. The observation of core-shell cylinders, instead of solid cylinders of styrene, in all annealed samples was unexpected. Core-shell cylindrical morphology for a two-phase system is very rare. Other than one experimental study[2] in which the formation of core-shell cylinders in a poly(styrene-*b*-cyclohexadiene) diblock copolymer was reported, there has been no report on core-shell cylindrical morphology in other two-phase block copolymer systems. In order to find out whether this is a true morphology or a staining artifact, as some might claim, detailed TEM image analysis is needed.

Nevertheless, it is evident from the TEM images (Figures 5.1b, 5.1d, and 5.1f) that the degree of order varies greatly in the final morphology, depending on the initial casting solvent. In particular, the core-shell cylindrical morphology in SEBS cast from hexane, a strongly-selective solvent, appears to have the best long-range order. Large grains of well-aligned cylinders are seen in TEM. This may be attributed to the templating effect of well-ordered BCC spherical lattice formed when the sample was cast from hexane. This type of templating based on well-ordered non-equilibrium morphology has not been reported before and may be utilized in improving long-range order in certain block copolymer morphologies.

5.2 Polydiacetylene (PDA) Micron and Submicron Crystals

5.2.1 Introduction

The preparation and characterization of polydiacetylene (PDA) micron and submicron size crystals by the reprecipitation method[3] has allowed the study of PDAs and their properties in a new morphology. The reprecipitation method involves pouring a diacetylene (DA) monomer solution into a poor solvent, usually water, under vigorous stirring. This is typically followed by polymerization initiated by ultraviolet light. The crystals thus formed have good dispersion for long periods of time (several days to several months). Micron and submicron size PDA crystals prepared by this method were found to be of interest for the assessment of third order[4] and fifth order[5] nonlinear optical properties of the PDA of 1,6-di-N-carbazolyl-2,4-hexadiyne (DCH, 1a). The molecular structures of PDAs under discussion are given in Figure 5.3.

A noteworthy property of micron and submicron sized crystals of PDA-DCH is the shift to shorter wavelengths of the wavelength of strongest visible absorption as crystal size decreases from bulk crystals to nano-crystals.[6] In connection with our interest in the possibility that the thermochromic phase transition in the PDA of the *bis*-alkylurethanes of 5,7-dodecadiyn-1, 12-diol involved an aggregate structure of several chains in contrast to the need for only a single chain[7], micro- and submicron-crystals of the PDAs of the *bis*-ethyl (ETCD, 1b) and *bis*-*n*-propyl (PUDO, 1c) urethanes were prepared and their optical properties were studied. In this work, morphological characterization through transmission electron microscopy (TEM) and electron

diffraction (ED) is performed on these micron and submicron sized PDA crystals, in order to study the possible crystal structural changes associated with these optical shifts.

5.2.2 Experimental Methods

Micro- and submicron-crystals of the monomers of the *bis*-ethyl (ETCD, 1b) and *bis*-*n*-propyl (PUDO, 1c) urethanes were prepared by the reprecipitation followed by ultrasonic irradiation (42 KHz) method, which were then polymerized with 254-nm UV light for an irradiation period of 20 minutes. This preparative work has been previously described.[8]

Samples for TEM and ED were prepared by directly dropping the respective PDA crystal-water dispersions onto carbon coated copper grids, which were then allowed to air dry at room temperature overnight. TEM and ED were performed using a JEOL 2000 FX TEM at 200 kV accelerating voltage. In performing these experiments, care was taken to limit unnecessary electron beam exposure thus minimizing electron beam damage and producing the best possible electron diffraction patterns. This included such standard procedures as focusing on an adjacent area to the area where data was recorded, using the smallest possible spot size, limiting the spread of the beam, and turning the beam off when it was not needed. Also the ED data was recorded on fast X-ray film (Kodak DEF5) rather than standard EM film.

5.2.3 Results and Disscussion

PDA-ETCD and PDA-PUDO micron (0.5-2 μm in length) and submicron sized (250-350 nm) crystals exhibited absorption spectra with maxima at 655 and 660 nm, respectively, when suspended in water. These spectra exhibit vibronic structures and are shown in Figure 5.4. The spectra in Figure 5.4 did not change with longer periods of UV irradiation. These maxima are to be compared to those reported for bulk crystals of PDA-ETCD[9] and -PUDO[10], 635 and 640 nm, respectively. This amounts to a shift to lower energy of about 0.06 eV between spectral maximum in bulk crystals and micron scale crystals. Hence in contrast to PDA-DCH, where the absorption maximum shifts to shorter wavelength as crystal size decreases, in these thermochromic PDA specimens, the absorption maximum shifts to longer wavelengths as crystal size decreases from bulk crystals to those with micron scale dimension.

FTIR spectra of the micron scale and submicron scale PDA specimens are indistinguishable from those of the bulk specimens. Hence there is no compositional difference between the two kinds of materials. X-ray powder diffraction was recorded at room temperature for bulk crystals, micron scale, and submicron scale crystals of PDA-ETCD and -PUDO. The data are summarized in Table 5.3. The diffraction of both PDAs is dominated by the *h00* reflections, and the three specimens of each PDA have similar diffraction patterns. These are in accord with literature[11] data and indicate that the micron scale and submicron scale crystals have a structure similar to the bulk crystals.

TEM morphologies of PDA-ETCD and PDA-PUDO bulk, micron, and submicron crystals, and respective electron diffraction patterns are shown in Figures 5.5-5.18. Most electron diffraction patterns are from zone [100], or b*-c* plane, where only *0hk* reflections are observed. This is because the a-axis of the PDA crystal is along its thickness direction, which is parallel to the electron beam when performing electron diffraction on these PDA crystals. In some rare cases the crystal is rolled up, which allows the a-axis of the crystal to be in the plane of the electron diffraction. One such case is seen in Figures 5.13-5.14, for PDA-PUDO bulk crystal, in which the reflections are all *0hk* reflections from zone [001], or a*-b* plane. Therefore for PDA-PUDO, all three lattice parameters a, b and c can be determined from the electron diffraction data, whereas for PDA-ETCD, only two of the lattice parameters, b and c can be determined. The crystal lattice parameters for the bulk, micron, and submicron crystals of PDA-ETCD and PDA-PUDO are summarized in Figures 5.19-5.22. It is clear from these figures that for both PDAs the crystal lattice parameters do not change noticeably when the crystal size goes from bulk to micron and submicron scales.

It is our assumption that the shift to longer wavelength of the spectra of the micron and submicron sized PDA crystals involves a modest enhancement of the mechanical strains likely present in the bulk crystals. We have earlier reported[12] solid state NMR data that support the involvement of mechanical strains in the thermochromic phase transition of these PDA, namely that mechanical strains on the PDA backbone at ambient temperature are partially relieved on heating above the temperature of the thermochromic phase transition. The spectral shift of the thermochromic shift of these

PDA is approximately 0.35 eV and involves[11] a volume expansion of the crystallographic unit cell of 2.5-3.0%. As noted above, the shift in the electronic spectrum between bulk crystals and the smaller specimens is about 0.06 eV. Hence, it is likely that any change in unit cell dimensions as a result of increased mechanical strains may not be detectable under the present conditions.

5.3 References

(1) Lodge, T. P.; Pudil, B.; Hanley, K. J. *Macromolecules* **2002**, *35*, 4707–4717.

(2) David, J. L.; Gido, S. P.; Hong, K.; Zhou, J.; Mays, J. W.; Tan, N. B. *Macromolecules* **1999**, *32*, 3216–3226.

(3) Kasai, H.; Nalwa, H. S.; Oikawa, H.; Okada, S.; Matsuda, H.; Minami, N.; Kakuta, A.; Ono, K.; Mukoh, A.; Nakanishi, H. *Jap. J. Appl. Phys.* **1992**, *31*, L1132–L1134.

(4) Nakanishi, H.; Kasai, H., in *Photonic and Optoelectronic Polymers*, ACS Symposium Series, Jenekhe, S. A. and Wynne, K. J., Eds., vol. 672, pp. 183–198; American Chemical Society, Washington, D.C.

(5) Yang, K.; He, J.-A.; Kumar, J.; Samuelson, L. A.; Oshikiri, T.; Katagi, H.; Kasai, H.; Okada, S.; Oikawa, H.; Nakanishi, H. *J. Opt. Soc. Am. B* **2005**, *22*, 6123–6132.

(6) (a) Katagi, H.; Kasai, H.; Okada, S.; Oikawa, H.; Matsuda, H.; Nakanishi, H. *J. Macromol. Sci.-Pure Appl. Chem. A* **1997**, *34*, 2013–2024. (b) Nakanishi, H.; Katagi, H. *Supramolecular Science* **1998**, *5*, 289–295. (c) Oikawa, H.; Oshikiri, T.; Kasai, H.; Okada, S.; Tripathy, S. K.; Nakanishi, H. *Polym. Adv. Technol.* **2000**, *11*, 783–790. (d) Onodera, T.; Oshikiri, T.; Katagi, H.; Kasai, H.; Okada, S.; Oikawa, H.; Terauchi, M.; Terauchi, M.; Tanaka, M.; Nakanishi, H. *Journal of Crystal Growth* **2001**, *229*, 586–590. (e) Volkov, V.; Asahi, T.; Masuhara, H.; Masuhara, A.; Kasai, H.; Oikawa, H.; Nakanishi, H. *Journal of Phys. Chem. B* **2004**, *108*, 7674–7680.

(7) Sandman, D. J. *Trends in Polymer Sci.* **1997**, *5*, 71–74.

(8) Wang, X.; Yang, K.; Ye, H.; Wang, Y.; Lee, J. S.; Sandman, D. J. *J. Macromol. Sci. A* **2006**, *43*, 1937–1943.

(9) Chance, R. R.; Baughman, R. H.; Mueller, H.; Eckhardt, C. J. *J. Chem. Phys.* **1977**, *67*, 3616–3618.

(10) Koshihara, S.; Tookura, Y.; Takeda, K.; Koda, T. *Phys. Rev. Lett.* **1992**, *68*, 1148.

(11) (a) Downey, M. J.; Hamill, G. P.; Rubner, M.; Sandman, D. J.; Velazquez, C. S. *Die Makromol. Chem.* **1988**, *188*, 1199–1205. (b) Tanaka, H.; Gomez, M. A.; Tonelli, A. E.; Lovinger, A. J.; David, D. D.; Thakur, M. *Macromolecules* **1989**, *22*, 2427–2432.

(12) Lee, D.-C.; Sahoo, S. K.; Cholli, A. L.; Sandman, D. J. *Macromolecules* **2002**, *35*, 4347–4355.

Table 5.1 Molecular Characteristics of the SEBS Triblock Copolymer

Polymer	M_n (kg mol^{-1})	M_w/M_n	ϕ_{PS}	ϕ_{PEB}
SEBS	76.0	1.07	26	74

ϕ_x is the volume fraction of x.
PS: polystyrene.
PEB: poly(ethylene-*co*-butylene).

Table 5.2 Summary of SEBS Morphologies Cast from Selective Solvents

Casting Solvent	Thermal History	Morphology	d_1 (nm)
Toluene	As cast	Well-ordered lamellae	37.2
Toluene	Annealed	Core-shell cylinders	30.2
Cyclohexane	As cast	Lamellae/modified layers	33.6
Cyclohexane	Annealed	Core-shell cylinders	29.8
Hexane	As cast	BCC spheres	21.8
Hexane	Annealed	Core-Shell cylinders	25.8

Table 5.3 X-ray Powder Diffraction Data for PDA-ETCD and PDA-PUDO

PDA	Size of PDA Crystals	2θ (°)	d-spacings (nm)
ETCD	Bulk	4.8. 9.6. 14.3	1.84. 0.92. 0.62
ETCD	Approx. 1 micron	4.8. 9.7. 14.6	1.84. 0.91. 0.61
ETCD	Approx. 350 nm	4.8. 9.7. 14.6	1.84. 0.91. 0.61
PUDO	Bulk	4.3. 8.8. 13.2	2.01. 1.01. 0.67
PUDO	Approx. 1 micron	4.3. 8.8. 13.2	2.01. 1.01. 0.67
PUDO	Approx. 300 nm	4.3. 8.8. 13.2	2.01. 1.01. 0.67

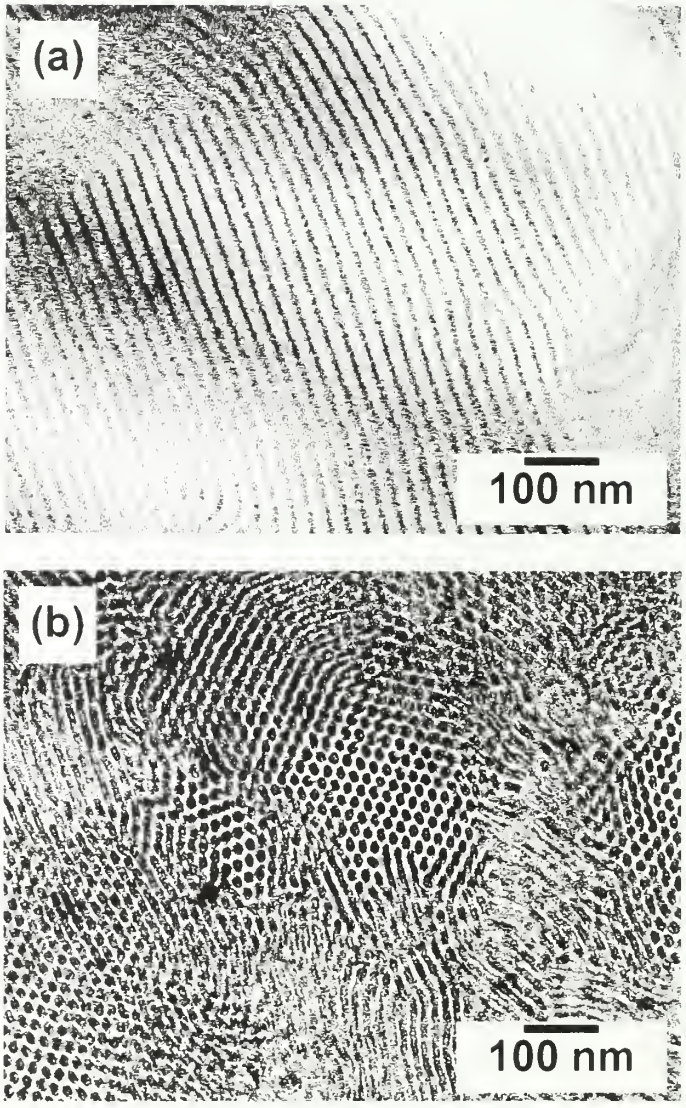

Figure 5.1 TEM morphologies of SEBS cast from different solvents. (a) and (b) are from toluene; (c) and (d) are from cyclohexane; (e) and (f) are from hexane. (a), (c), (e): as-cast; (b), (d), (f): after three weeks of thermal annealing. (Continued)

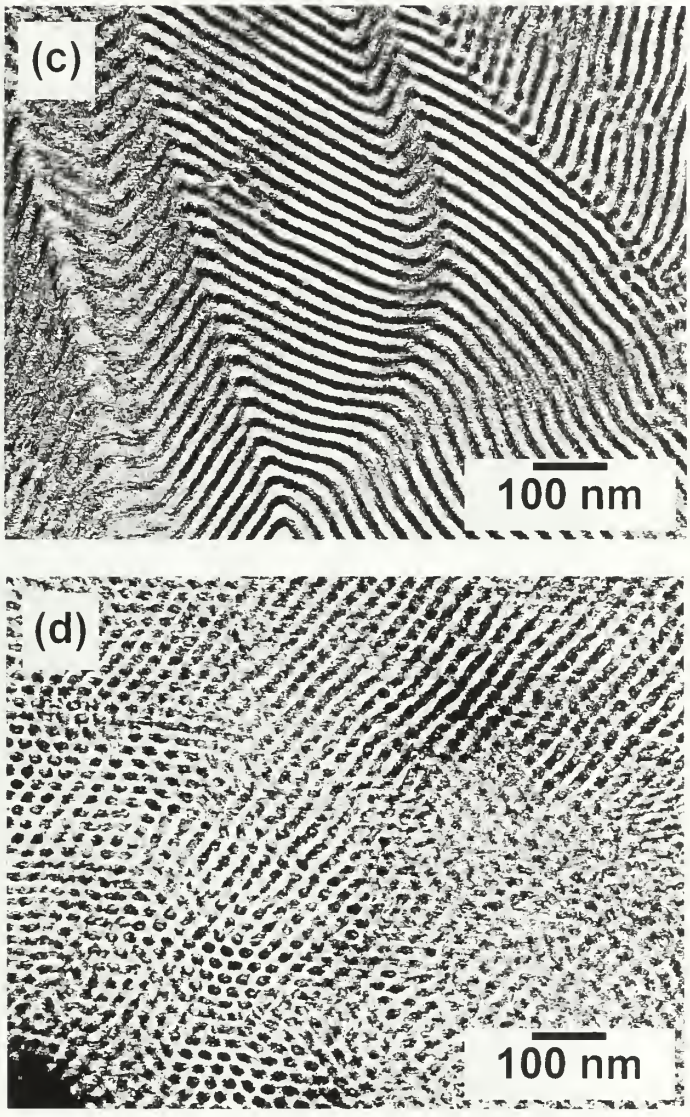

Figure 5.1 Continued.

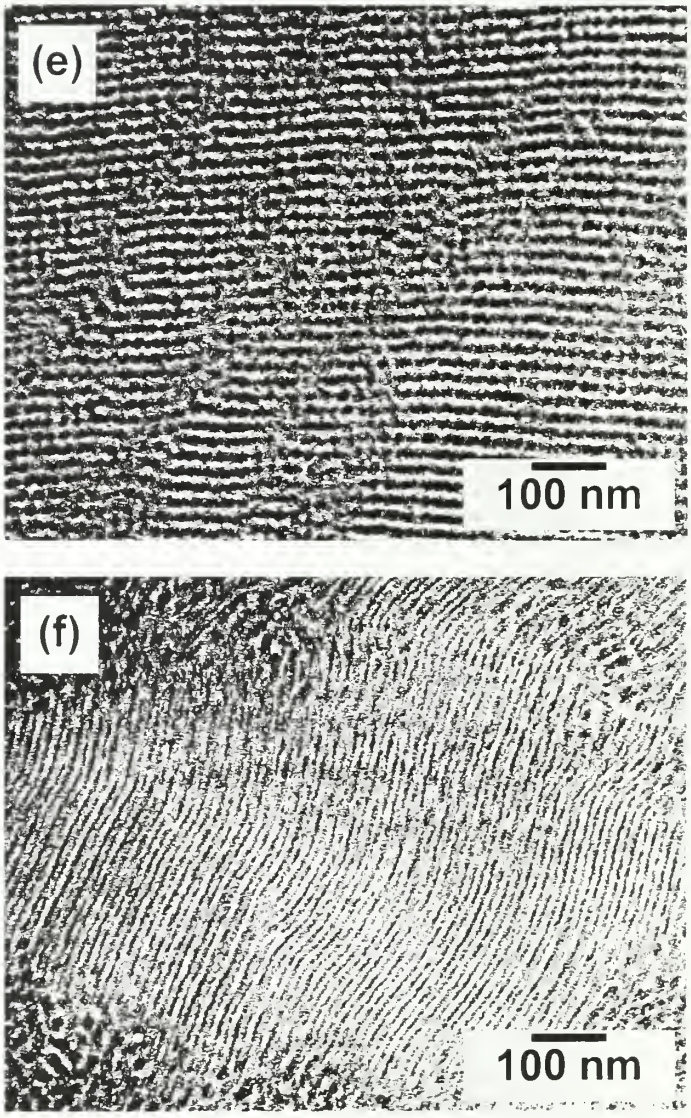

Figure 5.1 Continued.

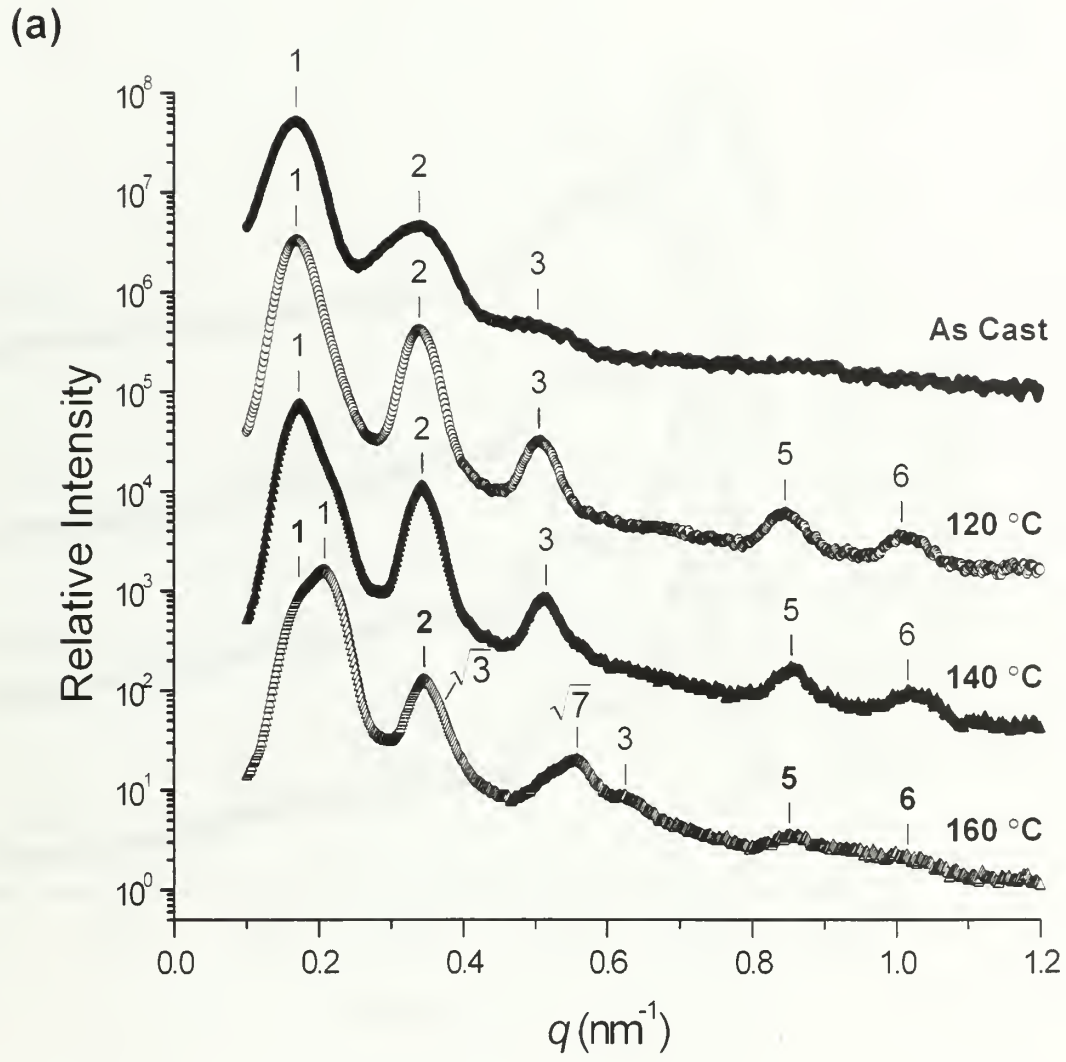

Figure 5.2 SAXS profiles of SEBS cast from (a) toluene: (b) cyclohexane: (c) hexane. (Continued)

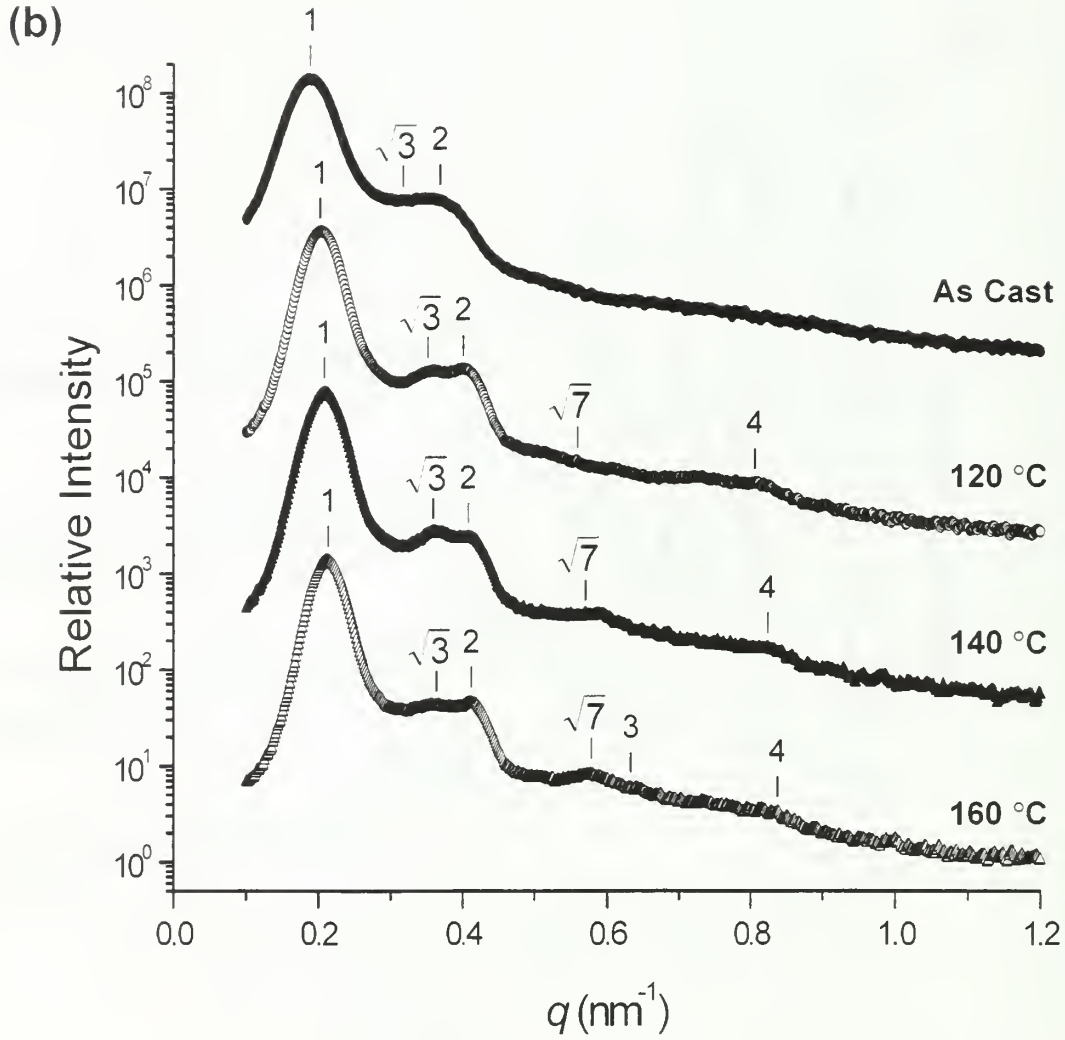

Figure 5.2 Continued.

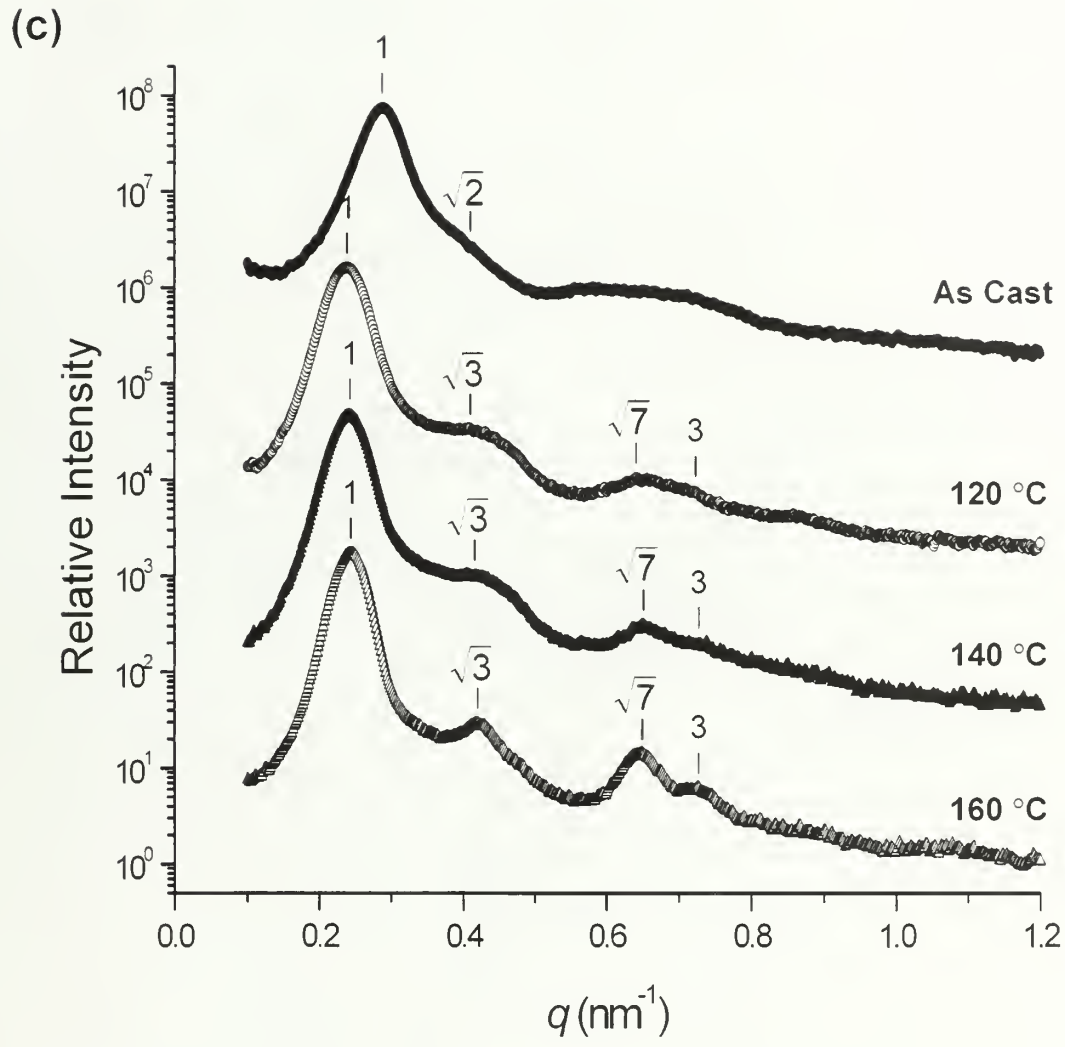

Figure 5.2 Continued.

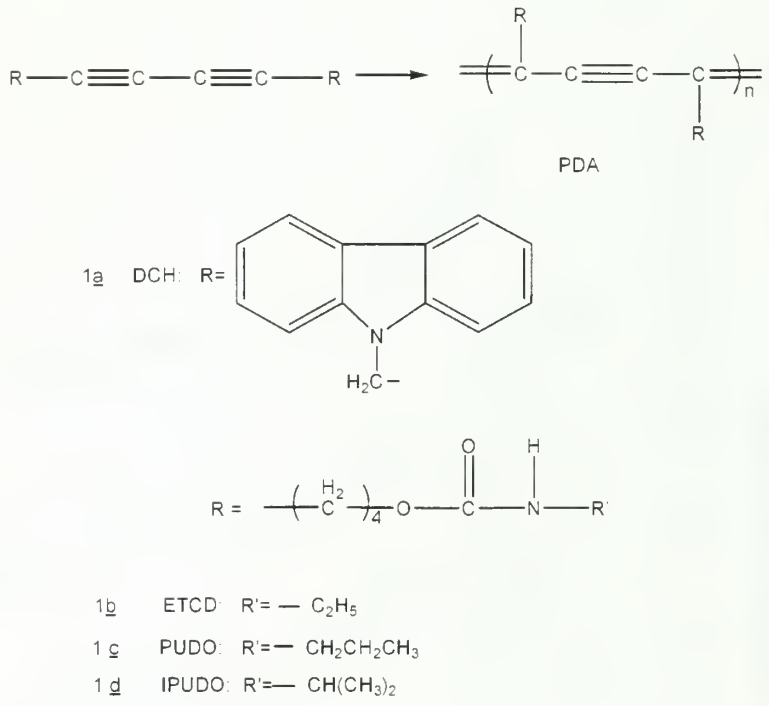

Figure 5.3 Repeat structures for PDA-ETCD and PDA-PUDO.

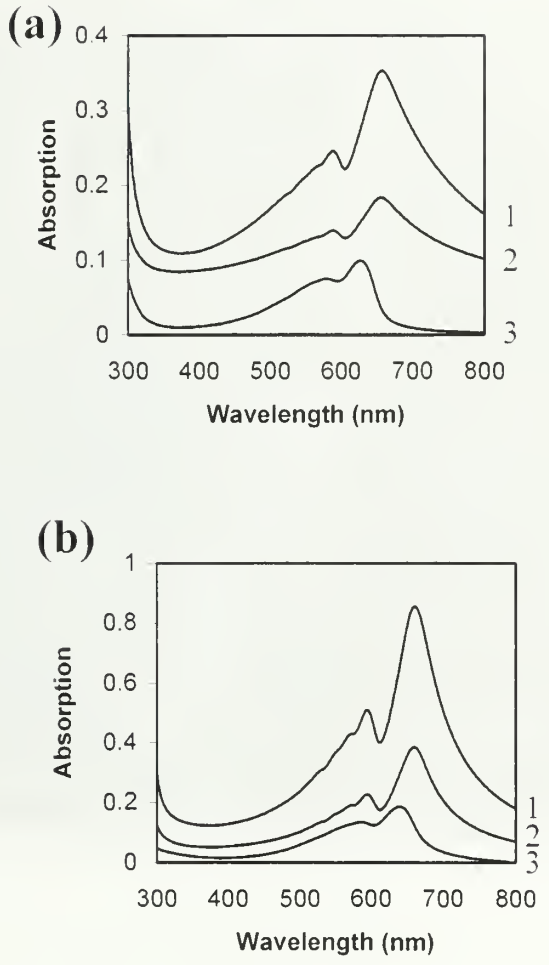

Figure 5.4 Electronic absorption spectra of PDA-ETCD and PDA-PUDO bulk, micron, and submicron crystals. (a) 1 (1~2 μm) and 2 (~250nm) and 3 (bulk) are PDA-ETCD micron, submicron, and bulk crystals, respectively; (b) 1 (~1μm) and 2 (~350nm) and 3 (bulk) are PDA-PUDO micron, submicron, and bulk crystals, respectively.

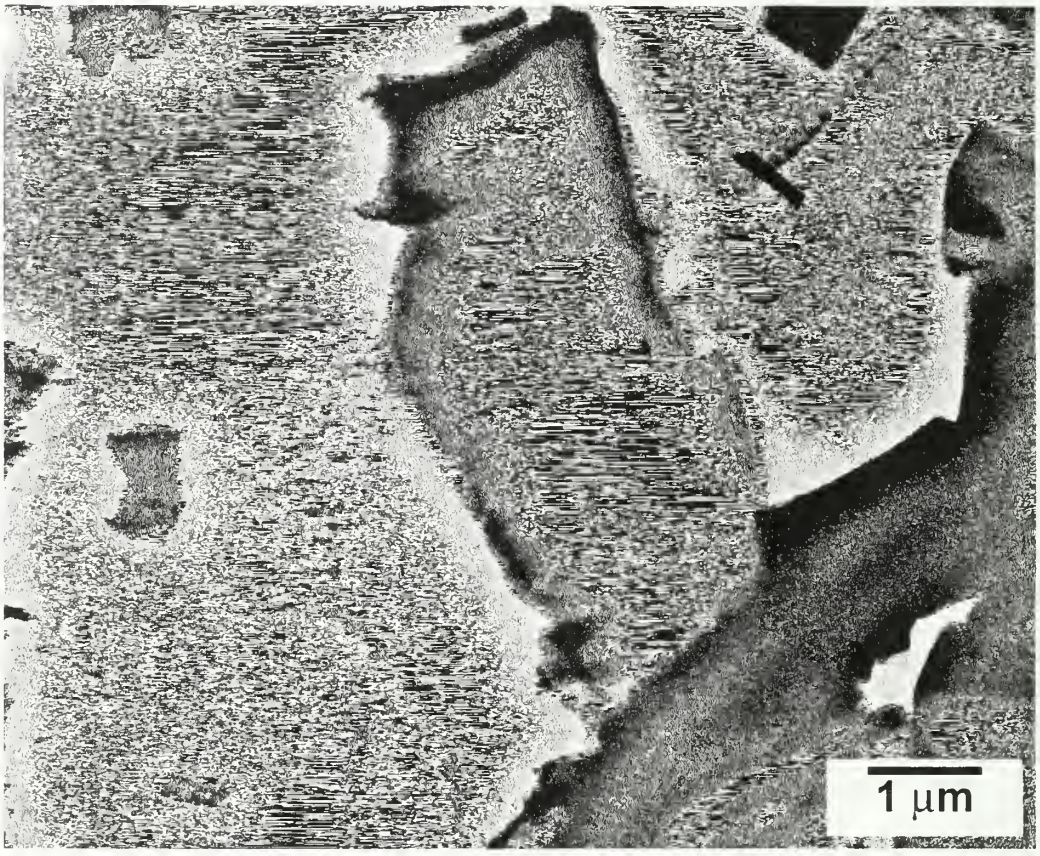

Figure 5.5 TEM morphology of a representative PDA-ETCD bulk crystal of size about 2 μm x 6 μm.

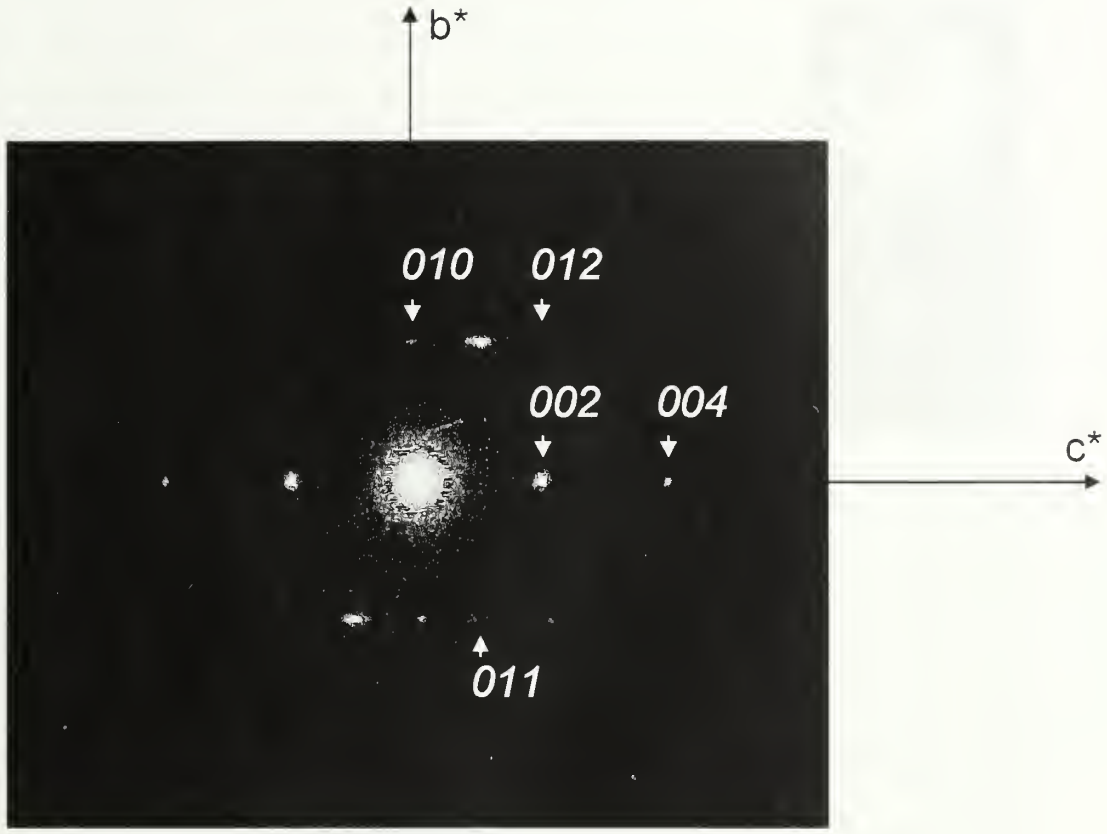

Figure 5.6 PDA-ETCD bulk crystal electron diffraction pattern from zone [100]. b*-c* plane.

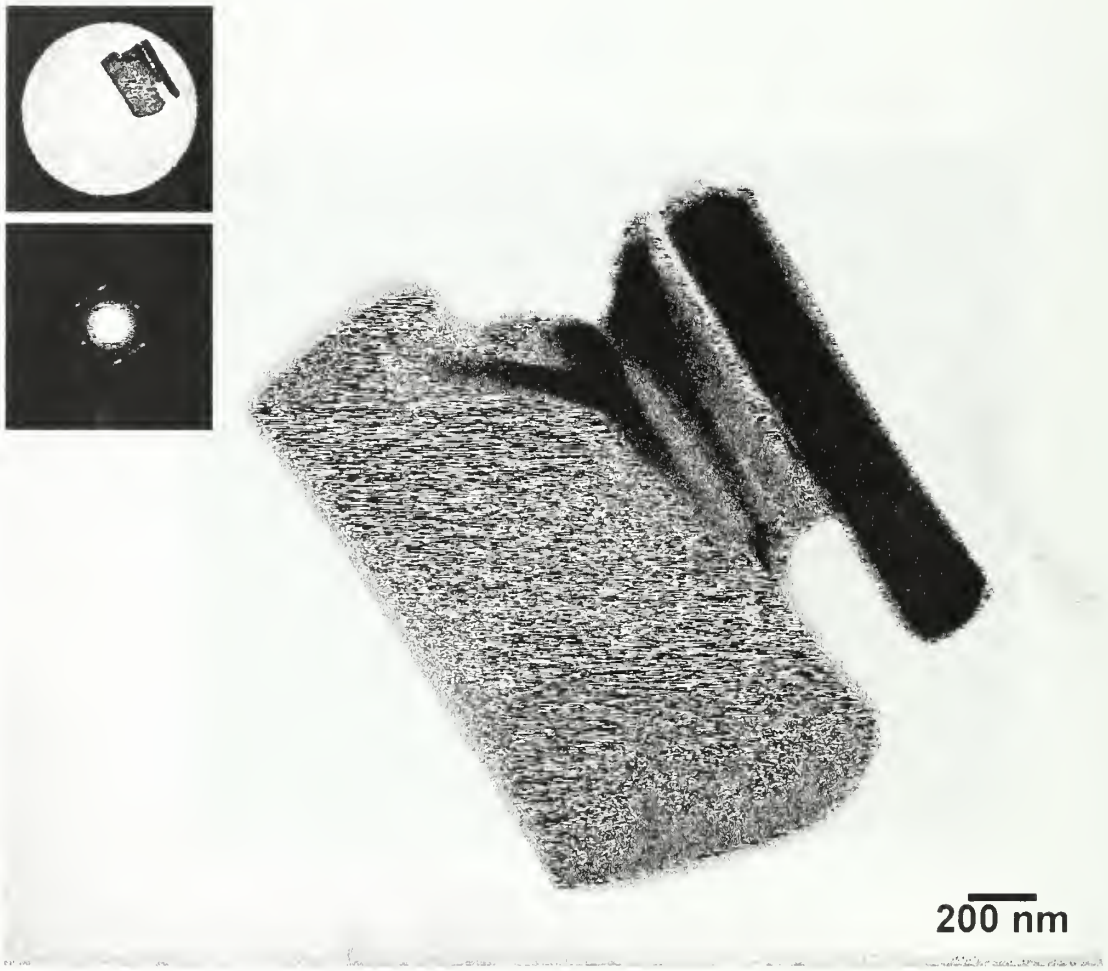

Figure 5.7 TEM morphology of a representative PDA-ETCD micron crystal. Upper inset shows the area selected for electron diffraction. Lower inset shows the corresponding electron diffraction pattern from zone [100], b*-c* plane.

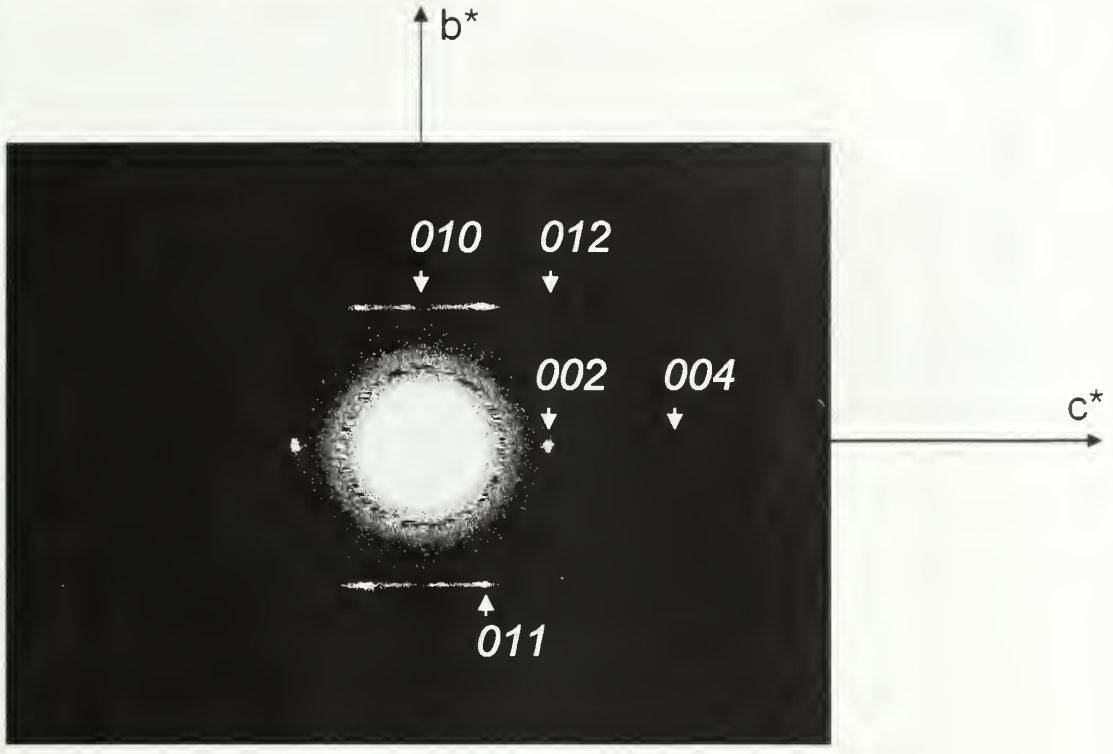

Figure 5.8 PDA-ETCD micron crystal electron diffraction pattern from zone [100]. b*-c* plane.

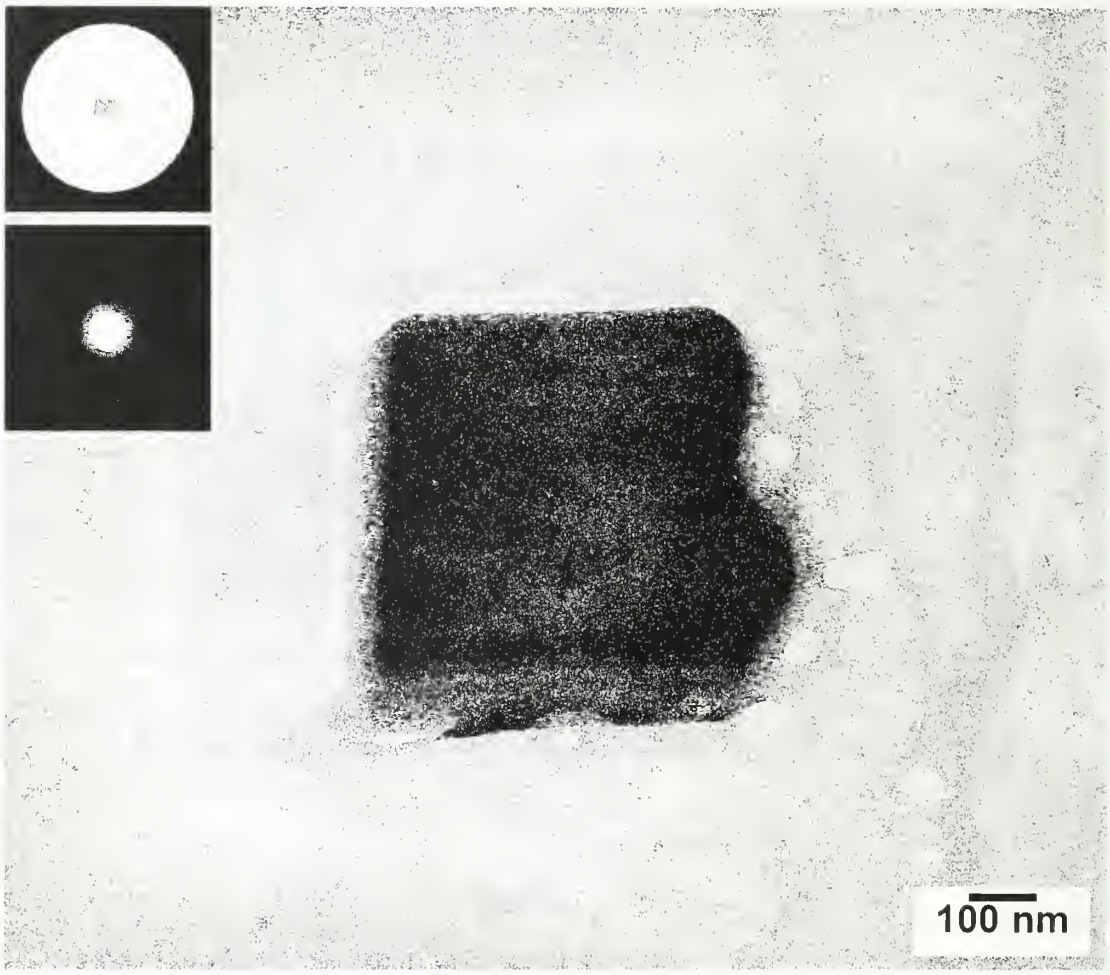

Figure 5.9 TEM morphology of a representative PDA-ETCD submicron crystal. Upper inset shows the area selected for electron diffraction. Lower inset shows the corresponding electron diffraction pattern from zone [100], b*-c* plane.

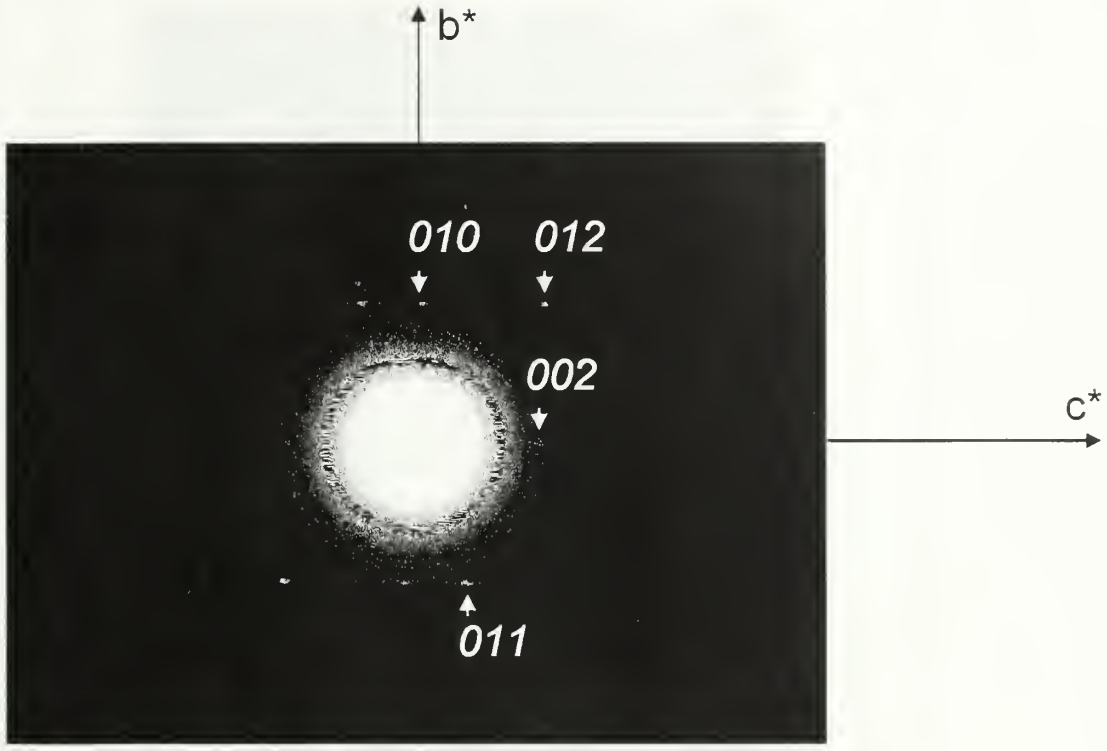

Figure 5.10 PDA-ETCD submicron crystal electron diffraction pattern from zone [100], b*-c* plane.

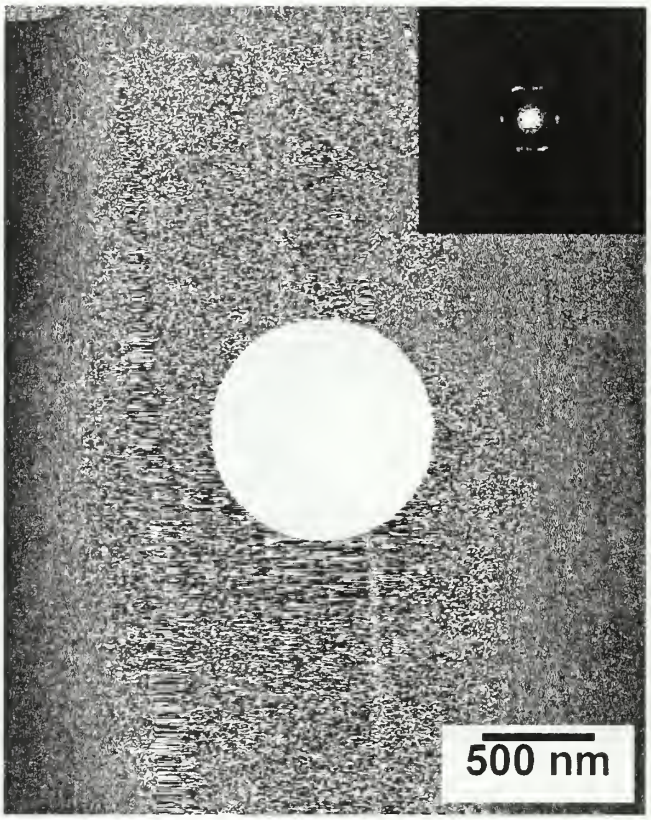

Figure 5.11 TEM image showing part of a large PDA-PUDO bulk crystal. Light circle in the center of the image shows the area selected for electron diffraction. Inset shows the corresponding electron diffraction pattern from zone [100]. b*-c* plane.

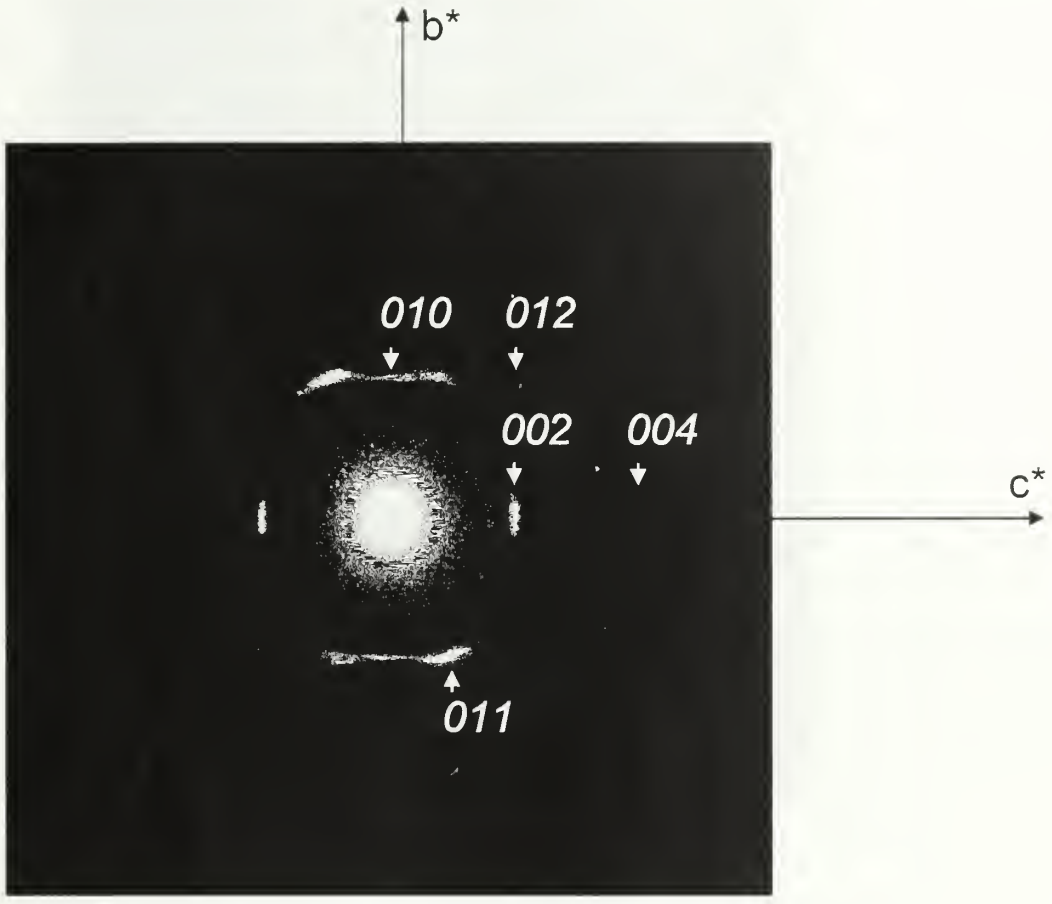

Figure 5.12 PDA-PUDO bulk crystal electron diffraction pattern from zone [100]. b*-c* plane.

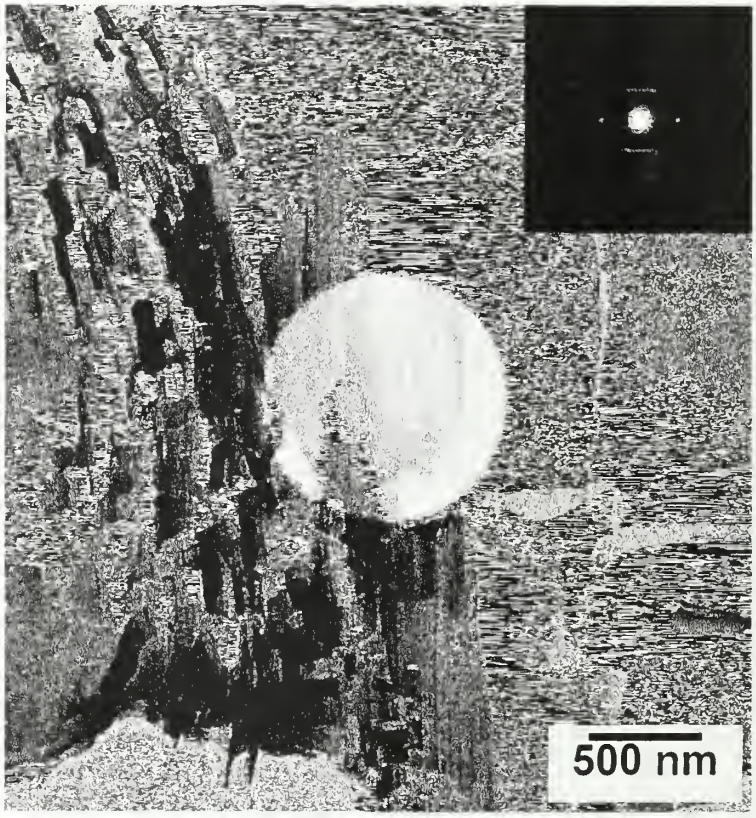

Figure 5.13 TEM image showing part of a large PDA-PUDO bulk crystal. Light circle in the center of the image shows the area selected for electron diffraction. Inset shows the corresponding electron diffraction pattern from zone [001], a*-b* plane.

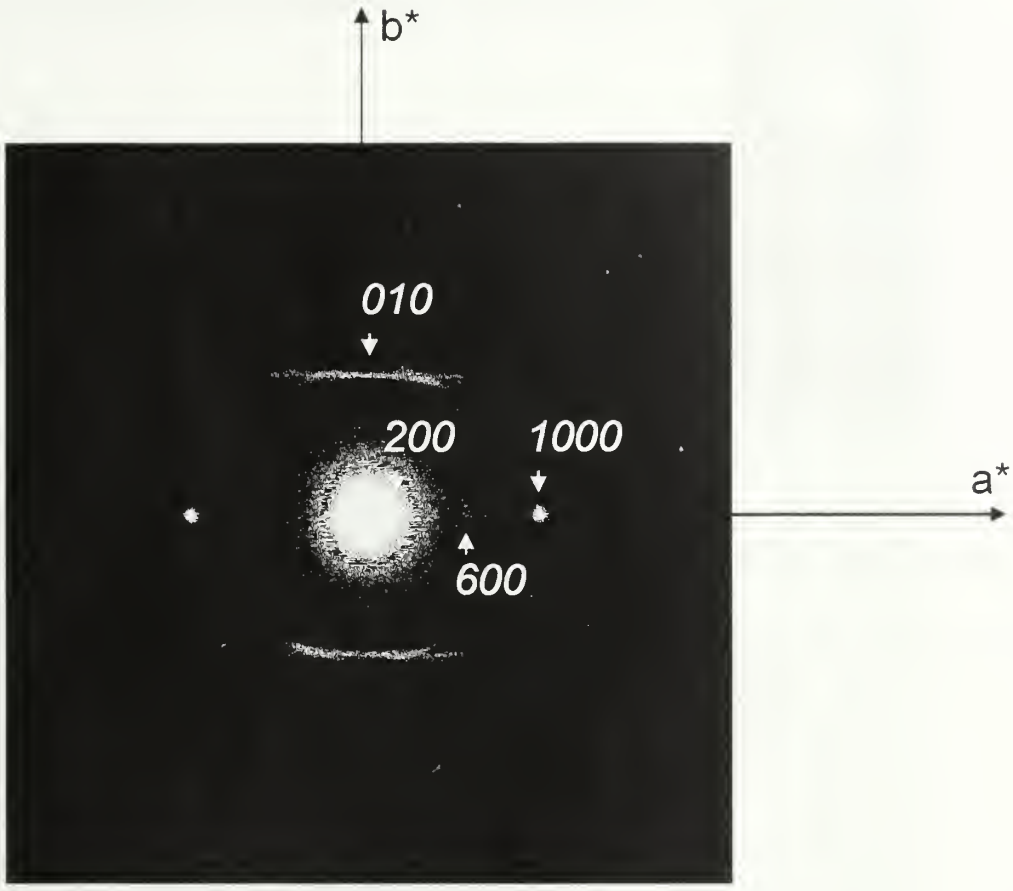

Figure 5.14 PDA-PUDO bulk crystal electron diffraction pattern from zone [001]. a*-b* plane.

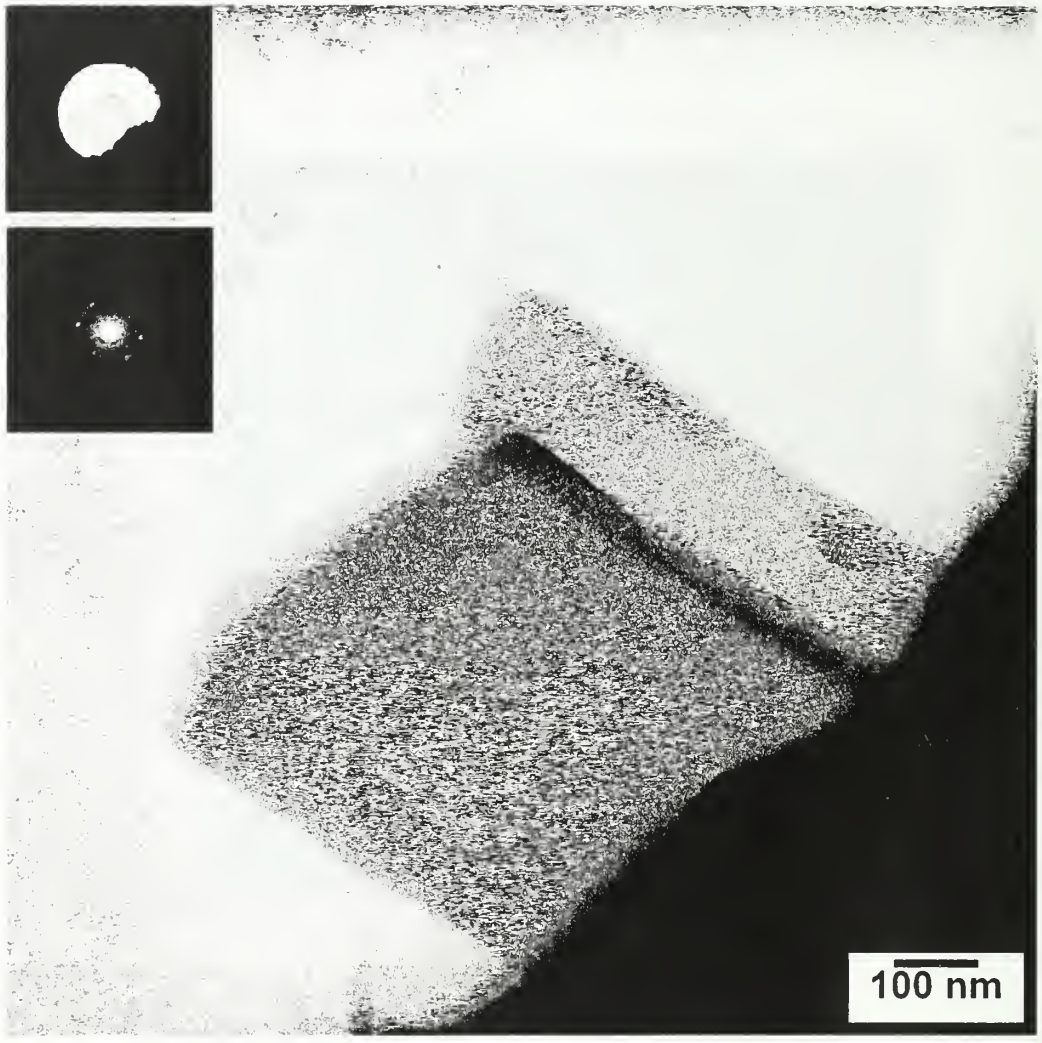

Figure 5.15 TEM morphology of a representative PDA-PUDO micron crystal. Upper inset shows the area selected for electron diffraction. Lower inset shows the corresponding electron diffraction pattern from zone [100], b*-c* plane.

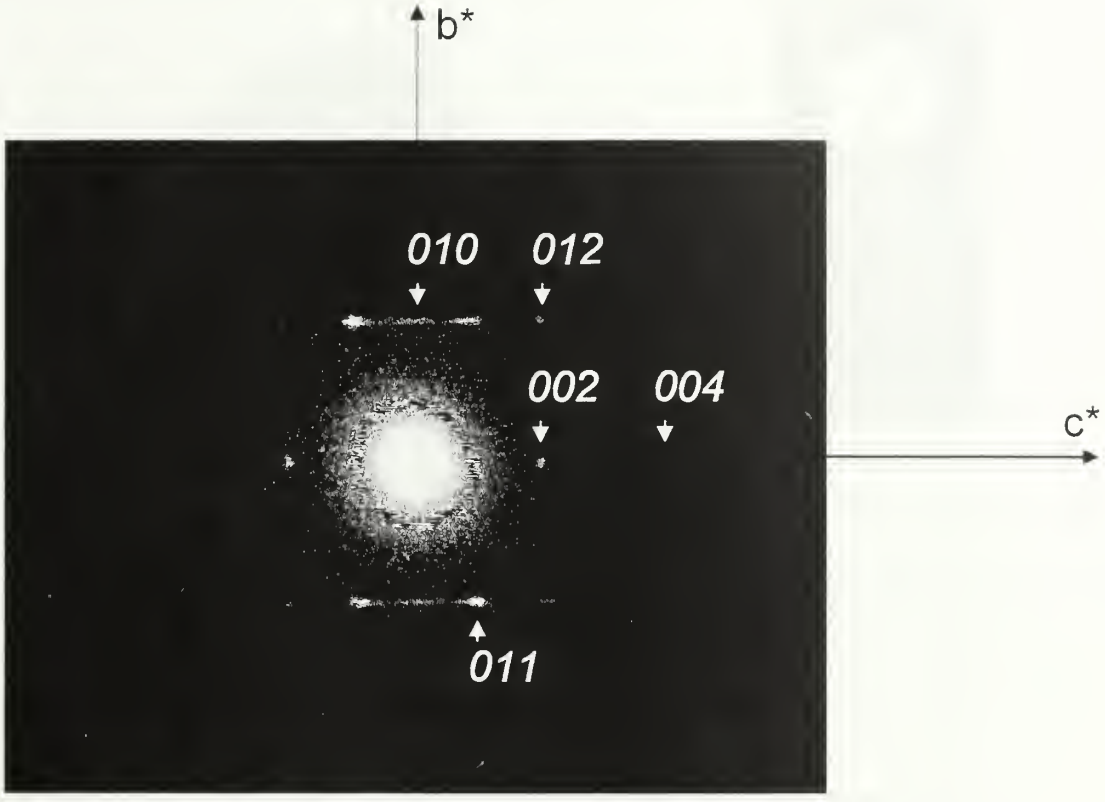

Figure 5.16 PDA-PUDO micron crystal electron diffraction pattern from zone [100]. b*-c* plane.

Figure 5.17 TEM morphology of a representative PDA-PUDO submicron crystal. Upper inset shows the area selected for electron diffraction. Lower inset shows the corresponding electron diffraction pattern from zone [100], b*-c* plane.

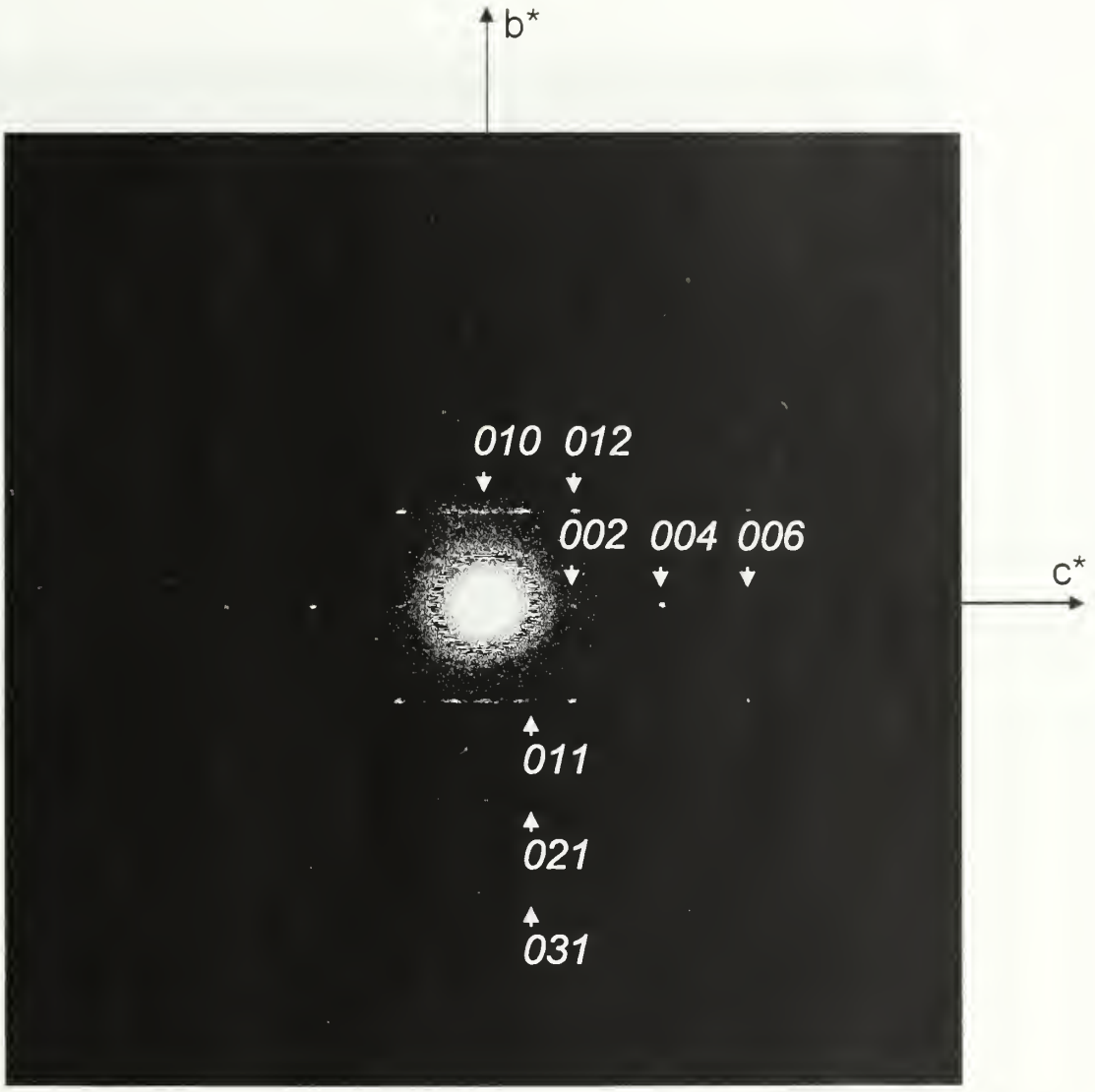

Figure 5.18 PDA-PUDO submicron crystal electron diffraction pattern from zone [100]. b*-c* plane.

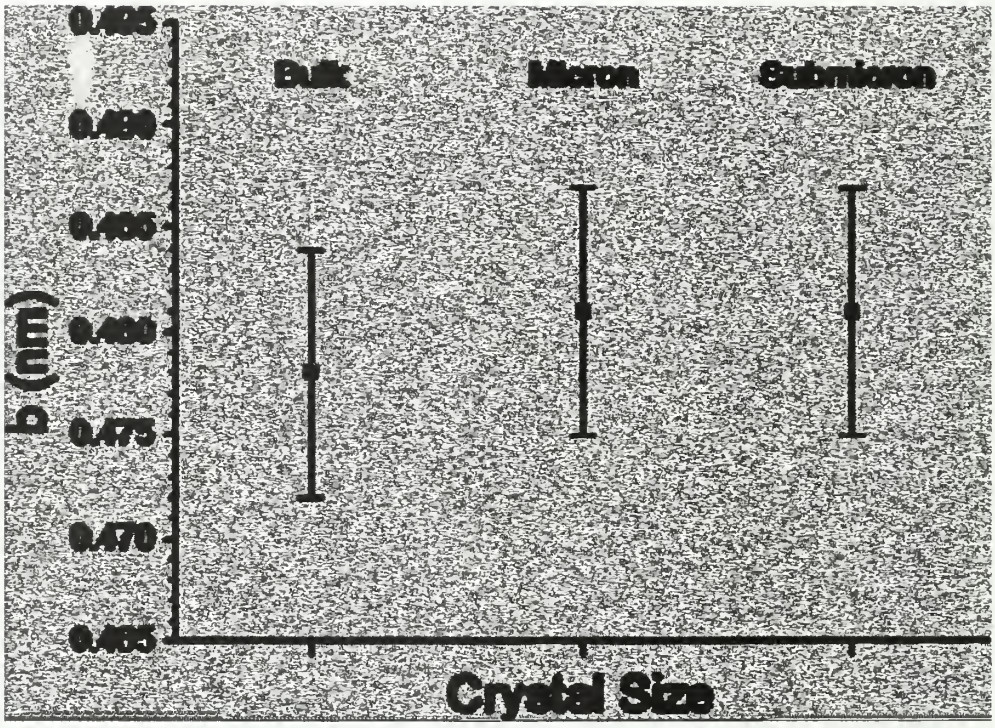

Figure 5.19 Comparison of PDA-ETCD lattice parameter b for bulk, micron, and submicron crystals.

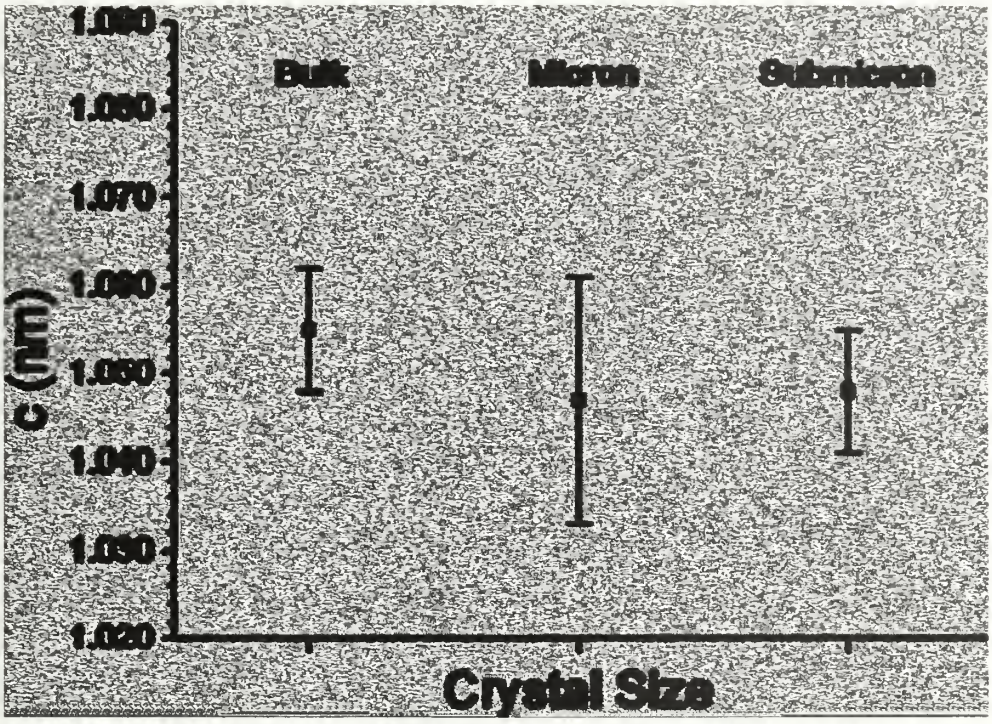

Figure 5.20 Comparison of PDA-ETCD lattice parameter c for bulk, micron, and submicron crystals.

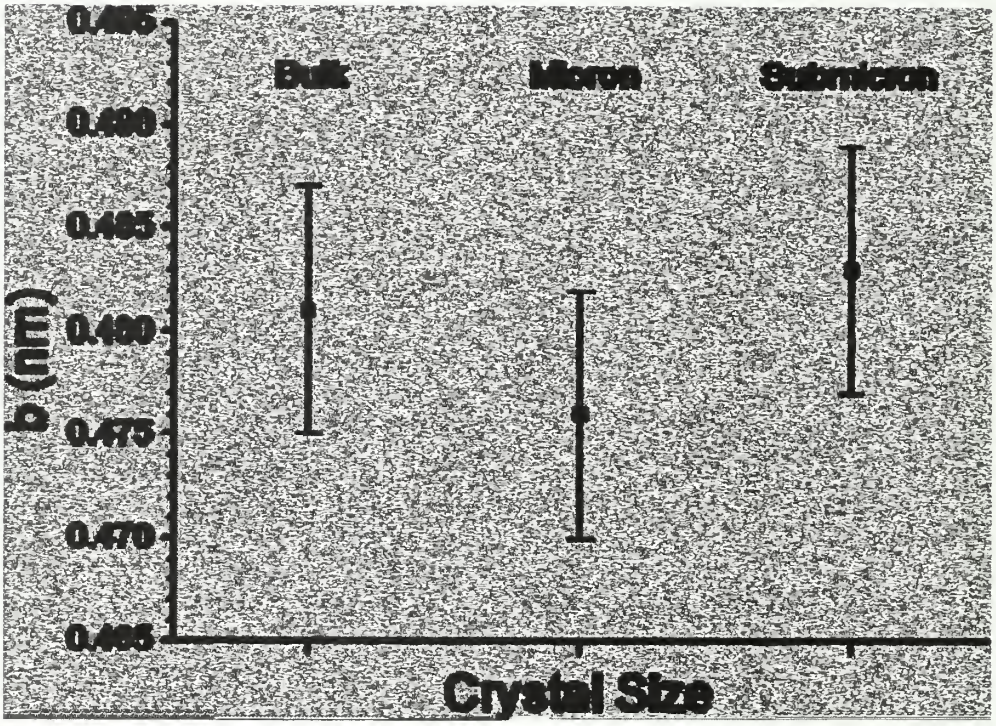

Figure 5.21 Comparison of PDA-PUDO lattice parameter b for bulk, micron, and submicron crystals.

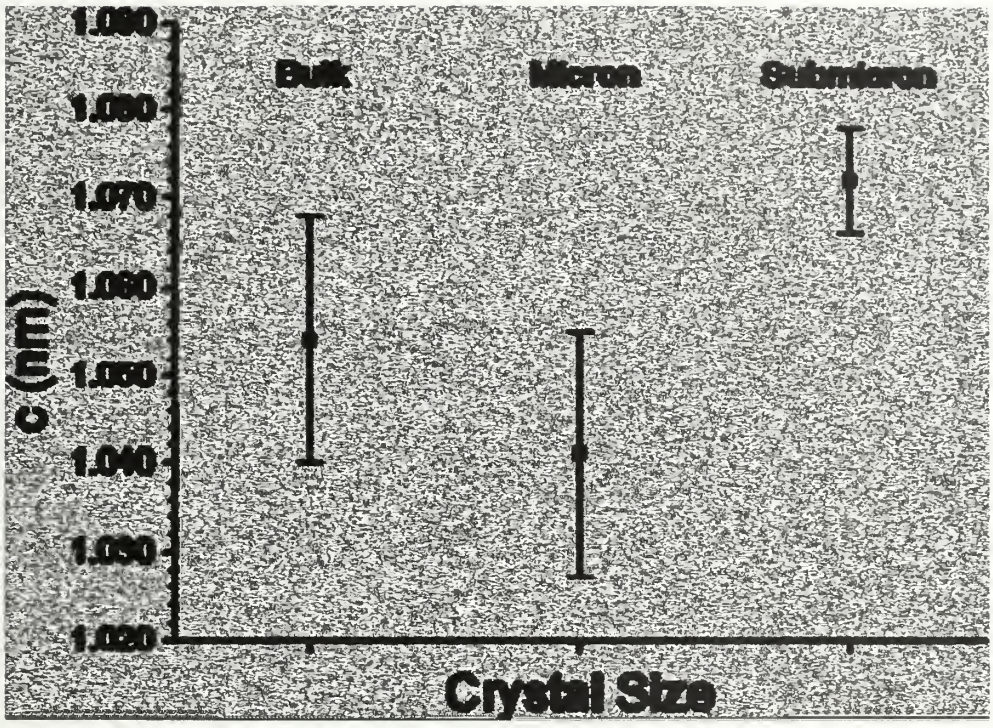

Figure 5.22 Comparison of PDA-PUDO lattice parameter c for bulk, micron, and submicron crystals.

BIBLIOGRAPHY

(1) Abetz, V.; Goldacker, T. *Marcomol. Rapid Commun.* **2000**, *21*, 16–34.

(2) Abetz, V.; Markgraf, K.; Rebizant, V. *Macromol. Symp.* **2002**, *177*, 139–145.

(3) Aoshima, S.; Iwasa, S.; Kobayashi, E. *Polym. J.* **1994**, *26* (8), 912–919.

(4) Bae, Y. C.; Faust, R. *Macromolecules* **1998**, *31*, 2480–2487.

(5) Bae, Y. C.; Hadjikyriacou, S.; Schlaad, H.; Faust, R. In *Ionic Polymerization and Related Processes*; Puskas J. E., Ed.; Kluwer Academic Publishers: Dordrecht, Germany, 1999.

(6) Barton, A. F. M. *CRC Handbook of Solubility Parameters and Other Cohesion Parameters*; CRC Press: Boca Raton, 1991; p 588.

(7) Brandrup, J.; Immergut, E. H.; Grulke, E. A.; Bloch, D., Eds. *Polymer Handbook*, 4th ed.; John Wiley & Sons: New York, 1999.

(8) Chance, R. R.; Baughman, R. H.; Mueller, H.; Eckhardt, C. J. *J. Chem. Phys.* **1977**, *67*, 3616–3618.

(9) Chen, S.; Gido, S. P.; Tsoukatos, T.; Avgeropoulos, A.; Hadjichristidis, N.; Hong, K.; Mays, J. W. *Polymer Preprints* **2005**, *46(2)*, 542.

(10) Chiang, C.-Y.; Lloyd, D. R. *J. Porous Mater.* **1996**, *2*, 273–285.

(11) Coca, S.; Matyjaszewski, K. *J. Polymer. Sci. Part A: Polym. Chem.* **1997**, *35*, 3595–3601.

(12) David, J. L.; Gido, S. P.; Hong, K.; Zhou, J.; Mays, J. W.; Tan, N. B. *Macromolecules* **1999**, *32*, 3216–3226.

(13) Downey, M. J.; Hamill, G. P.; Rubner, M.; Sandman, D. J.; Velazquez, C. S. *Die Makromol. Chem.* **1988**, *188*, 1199–1205.

(14) Duque, D.; Schick, M. *J. Chem. Phys.* **2000**, *113*, 5525–5530.

(15) Faust, R.; Kennedy, J. P. *Polym. Bull.* **1986**, *15*, 317–323.

(16) Feldthusen, J.; Iván, B.; Müller, A. H. E. *Macromolecules* **1998**, *31*, 578–585.

(17) Fishbein, L.; Crowe, B. F. *Makromol. Chem.* **1961**, *48*, 221–228.

(18) Fodor, Z.; Faust, R. *J. Macromol. Sci., Pure Appl. Chem.* **1994**, *A31* (12), 1985–2000.

(19) Fodor, Z.; Faust, R. *J. Macromol. Sci., Pure Appl. Chem.* **1995**, *A32* (3), 575–591.

(20) Gibson, L. J.; Ashby, M. F. *Cellular Solids: Structure and Properties*; Cambridge University Press: New York, 1997.

(21) Gido, S. P.; Gunther, J.; Thomas, E. L.; Hoffman, D. *Macromolecules* **1993**, *26*, 4506–4520.

(22) Gido, S. P.; Thomas, E. L. *Macromolecules* **1994**, *27*, 6137–6144.

(23) Gido, S. P.; Thomas, E. L. *Macromolecules* **1994**, *27*, 849–861.

(24) Glicklis, R.; Shapiro, L.; Agbaria, R.; Merchuk, J. C.; Cohen, S. *Biotechnol. Bioeng.* **2000**, *67*, 344–353.

(25) Goldacker, T.; Abetz, V.; Stadler, R.; Erukhimorich, I.; Leibler, L. *Nature* **1999**, *398*, 137–139.

(26) Gyor, M.; Fodor, Z.; Wang, H.-C.; Faust, R. *J. Macromol. Sci.* **1994**, *A31* (12), 2055–2065.

(27) Gyor, M.; Wang, H.-C.; Faust, R. *J. Macromol. Sci., Pure Appl. Chem.* **1992**, *A29*, 639–653.

(28) Hadjikyriacou, S.; Faust, R. *Macromolecules* **1995**, *28*, 7893–7900.

(29) Hadjikyriacou, S.; Faust, R. *Macromolecules* **1996**, *29*, 5261–5267.

(30) Hatada, K.; Kitayama, T.; Matsuo, N.; Yuki, H. *Polym. J.* **1983**, *15* (10), 719–725.

(31) Helfand, E.; Tagami, Y. J. Chem. Phys. 1972, 56, 3592.

(32) Hildebrand, J. H.; Scott, R. L. *The Solubility of Non-Electrolytes*; Reinhold: New York, 1949.

(33) Hong, K.; Mays, J. W. *Macromolecules* **2001**, *34*, 3540–3547.

(34) Imaizumi, K.; Ono, T.; Natori, I; Sakurai, S.; Takeda, K. *J. Polym. Sci. Pol. Phys.* **2001**, *39*, 13–22.

(35) Jaffer, K. M.; Wickham, R. A.; Shi, A.-C. *Macromolecules* **2004**, *37*, 7042–7050.

(36) Kasai, H.; Nalwa, H. S.; Oikawa, H.; Okada, S.; Matsuda, H.; Minami, N.; Kakuta, A.; Ono, K.; Mukoh, A.; Nakanishi, H. *Jap. J. Appl. Phys.* **1992**, *31*, L1132–L1134.

(37) Kaszas, G.; Puskas J. E.; Kennedy, J. P.; Hager, W. G. *J. Polym. Sci. Part A: Polym. Chem.* **1991**, *29*, 427–435.

(38) Katagi, H.; Kasai, H.; Okada, S.; Oikawa, H.; Matsuda, H.; Nakanishi, H. *J. Macromol. Sci.-Pure Appl. Chem. A* **1997**, *34*, 2013–2024.

(39) Kawaguchi T.; Sanda, F.; Masuda, T. *J. Polymer. Sci. Part A: Polym. Chem.* **2002**, *40* (16), 3938–3943.

(40) Keller, A.; Machin, M. J. *J. Macromol. Sci. Phys.* **1967**, *B1*, 41–91.

(41) Kennedy, J. P.; Iván, B. *Designed Polymers by Carbocationic Macromolecular Engineering: Theory and Practice*; Hanser Publishers: Munich, 1992.

(42) Kennedy, J. P.; Midha, S.; Tsunogal, Y. *Macromolecules* **1993**, *26*, 429–435.

(43) Kim, M. S.; Faust, R. *Polym. Bull.* **2002**, *48*, 127–134.

(44) Koshihara, S.; Tookura, Y.; Takeda, K.; Koda, T. *Phys. Rev. Lett.* **1992**, *68*, 1148.

(45) Kurian, J. Ph.D. Thesis, The University of Akron, **1991**.

(46) Kwon, Y.; Faust, R. *Macromolecules* **2002**, *35*, 3348–3357.

(47) Landau, L. D.; Lifshitz, E. M. *Electrodynamics of Continuous Media*; Pergamon: Oxford, 1987.

(48) Ledwith, A.; Lockett, E.; Sherrington, D. C. *Polymer* **1975**, *16*, 31–37.

(49) Lee, D.-C.; Sahoo, S. K.; Cholli, A. L.; Sandman, D. J. *Macromolecules* **2002**, *35*, 4347–4355.

(50) Leibler, L.; Gay, C.; Erukhimovich, I. *Europhys. Lett.* **1999**, *46*, 549–554.

(51) Li, D.; Faust, R. *Macromolecules* **1995**, *28*, 1383–1389.

(52) Li, D.; Faust, R. *Macromolecules* **1995**, *28*, 4893–4898.

(53) Li, W.-J.; Laurencin, C. T.; Caterson, E. J.; Tuan, R. S.; Ko, F. K. *J. Biomed. Mater. Res.* **2002**, *60*, 613–621.

(54) Lodge, T. P.; Pudil, B.; Hanley, K. J. *Macromolecules* **2002**, *35*, 4707–4717.

(55) Lu, Z.; Liu, G. J.; Duncan, S. *Macromolecules* **2004**, *37*, 174–180.

(56) Lubnin, A. V.; Kennedy, J. P. *J. Polym. Sci. Part A: Polym. Chem.* **1993**, *31*, 2825–2834.

(57) Ma, P. X.; Choi, J.-W. *Tissue Eng.* **2001**, *7*, 23–33.

(58) Ma, T.; Li, Y.; Yang, S.-T.; Kniss, D. A. *Biotechnol. Bioeng.* **2000**, *70*, 606–618.

(59) Mark, H. F.; Bikales, N. M.; Overberger, C. G.; Menges, G. In *Encyclopedia of Polymer Science and Engineering*; Mark, H. F., Ed.; John Wiley & Sons: New York, 1990; Vol. 9, p 509.

(60) Matsen, M. W. *J. Chem. Phys.*, **1997**, *107*, 8110–8119.

(61) Matyjaszewski, K., Ed. *Cationic Polymerizations, Mechanisms, Synthesis and Application*; Marcel Dekker: New York, 1996.

(62) Miyamoto, M.; Sawamoto, M.; Higashimura, T. *Macromolecules* **1984**, *17*, 265–268.

(63) Nakanishi, H.; Kasai, H., in *Photonic and Optoelectronic Polymers*, ACS Symposium Series, Jenekhe, S. A. and Wynne, K. J., Eds., vol. 672, pp. 183–198; American Chemical Society, Washington, D.C.

(64) Nakanishi, H.; Katagi, H. *Supramolecular Science* **1998**, *5*, 289–295.

(65) Nandi, S.; Winter, H. H.; Fritz, H. G. *Polymer* **2004**, *45*, 4819–4827.

(66) Ohgi, H.; Sato, T. *Macromolecules* **1999**, *32*, 2403–2409.

(67) Oikawa, H.; Oshikiri, T.; Kasai, H.; Okada, S.; Tripathy, S. K.; Nakanishi, H. *Polym. Adv. Technol.* **2000**, *11*, 783–790.

(68) Okamura, S.; Kodama, T.; Higashimura, T. *Makromol. Chem.* **1962**, *53*, 180–191.

(69) Onodera, T.; Oshikiri, T.; Katagi, H.; Kasai, H.; Okada, S.; Oikawa, H.; Terauchi, M.; Terauchi, M.; Tanaka, M.; Nakanishi, H. *Journal of Crystal Growth* **2001**, *229*, 586–590.

(70) Ouchi, M.; Kamigaito, M.; Sawamoto, M. *Macromolecules* ***1999***, *32*, 6407–6411.

(71) Paul, D.; Peinemann, K.-V. In *Polymeric Materials Encyclopedia*; Salamone, J. C., Ed.; CRC Press: Boca Raton, FL, 1996; Vol. 6, pp 4074–4082.

(72) Pennings, A. J.; Kiel, A. M. *Kolloid-Z.* **1965**, *205*, 160–162.

(73) Pernecker, T.; Kennedy, J. P.; Ivan, B. *Macromolecules* **1992**, *25*, 1642–1647.

(74) Pinnau, I. In *Encyclopedia of Separation Science*; Wilson, I. D., Ed.; Academic Press: San Diego, 2000; Vol. 4, pp 1755–1764.

(75) Puskas, J. E.; Kaszas, G. *Prog. Polym. Sci.* **2000**, *25*, 403–452.

(76) Roth, M.; Mayr, H. *Macromolecules* **1996**, *29*, 6104–6109.

(77) Sakai, Y.; Otsuka, M.; Hanada, S.; Nishiyama, Y.; Konishi, Y.; Yamashita, A. *Mat. Sci. Eng. C* **2004**, *24*, 379–386.

(78) Sandman, D. J. *Trends in Polymer Sci.* **1997**, *5*, 71–74.

(79) Saunders, J.; Hansen, R. In *Plastic Foams*; Frisch, K., Saunders, J., Eds.; Dekker: New York, 1972; Part I, pp 23–108.

(80) Schlaad, H.; Kwon, Y.; Faust, R.; Charleux, B. *Macromolecules* **2000**, *33*, 8225–8232.

(81) Schlaad, H.; Kwon, Y.; Faust, R.; Mayr, H. *Macromolecules* **2000**, *33*, 743–747.

(82) Shastri, V. P.; Martin, I.; Langer, R. *Proc. Natl. Acad. Sci. USA* **2000**, *97*, 1970–1975.

(83) Sipos, L.; Zsuga, M.; Deák, G. *Macromolecular Rapid Communication* **1995**, *16*, 935–940.

(84) Small, P. A. *J. Appl. Chem.* **1953**, *3*, 71–80.

(85) Stachowiak, A. N.; Bershteyn, A.; Tzatzalos, E.; Irvine, D. J. *Advanced Materials* **2005**, *17*, 399–403.

(86) Storey, R. F.; Chisholm, B. J. *Macromolecules* **1993**, *26*, 6727–6733.

(87) Suh, J.-K. F.; Matthew, H. W. T. *Biomaterials* **2000**, *21*, 2589–2598.

(88) Takano, A; Soga, K.; Suzuki, J; Matsushita, Y. *Macromolecules* **2003**, *36*, 9288–9291.

(89) Tanaka, H.; Gomez, M. A.; Tonelli, A. E.; Lovinger, A. J.; David, D. D.; Thakur, M. *Macromolecules* **1989**, *22*, 2427–2432.

(90) Tester, J. W.; Modell, M. *Thermodynamics and Its Applications*, 3rd ed.; Prentice Hall PTR: New Jersey, 1983, Appendix G.

(91) Thurn-Albrecht, T.; Schotter, J.; Kastle, G. A.; Emley, N.; Shibauchi, T.; Krusin-Elbaum, L.; Guarini, K.; Black, C. T.; Tuominen, M. T.; Russell, T. P. *Science* **2000**, *290*, 2126–2129.

(92) Trent, J. S.; Scheinbeim, J. I.; Couchman P. R. *Macromolecules* **1983**, *16*, 589–598.

(93) Tsori, Y.; Andelman, D; Schick, M. *Phys. Rev. E* **2000**, *61*, 2848–2858.

(94) Tsoukatos, T.; Avgeropoulos, A.; Hadjichristidis, N.; Hong, K.; Mays, J. W. *Macromolecules* **2002**, *35*, 7928–7935.

(95) Volkov, V.; Asahi, T.; Masuhara, H.; Masuhara, A.; Kasai, H.; Oikawa, H.; Nakanishi, H. *Journal of Phys. Chem. B* **2004**, *108*, 7674–7680.

(96) Wang, X.; Yang, K.; Ye, H.; Wang, Y.; Lee, J. S.; Sandman, D. J. *J. Macromol. Sci. A* **2006**, *43*, 1937–1943.

(97) Whaley, P. D.; Kulkarni, S.; Ehrlich, P.; Stein, R. S.; Winter, H. H.; Conner, W. C.; Beaucage, G. *J. Polym. Sci. Pol. Phys.* **1998**, *36*, 617–627.

(98) Whaley, P. D.; Kulkarni, S.; Winter, H. H.; Stein, R. S; Ehrlich, P. *Polym. Mat. Sci. Eng.* **1995**, *73*, 404–405.

(99) Whaley, P. D.; Winter, H. H.; Ehrlich, P. *Macromolecules* **1997**, *30*, 4887–4890.

(100) Wickham, R. A.; Shi, A.-C. *Macromolecules* **2001**, *34*, 6487–6494.

(101) Winter, H. H.; Gappert, G.; Ito, H. *Macromolecules* **2002**, *35*, 3325–3327.

(102) Wolff, T.; Burger, C.; Ruland, W. *Macromolecules* **1993**, *26*, 1707–1711.

(103) Wunderlich, B. *Macromolecular Physics, Vol. 3: Crystal Melting*; Academic Press: New York, 1980.

(104) Yang, K.; He, J.-A.; Kumar, J.; Samuelson, L. A., Oshikiri, T.; Katagi, H.; Kasai, H.; Okada, S.; Oikawa, H.; Nakanishi, H. *J. Opt. Soc. Am. B* **2005**, *22*, 6123–6132.

(105) Yariv, A. *Quantum Electronics*; Saunders College Publishing: Philadelphia, 1991.

(106) Zhou, Y.; Faust, R. *Polymer Preprints* **2003**, *44* (2), 661–662.